Mild pH-decoupling Aqueous Flow Battery with Practical pH Recovery

Dawei Xi[1,3], Abdulrahman M. Alfaraidi[1,3], Jinxu Gao[2], Thomas Cochard[1], Luana C. I. Faria[1], Zheng Yang[1], Thomas Y. George[1], Taobo Wang[1], Roy G. Gordon[1,2] *, Richard Y. Liu[2] *, Michael J. Aziz[1] *
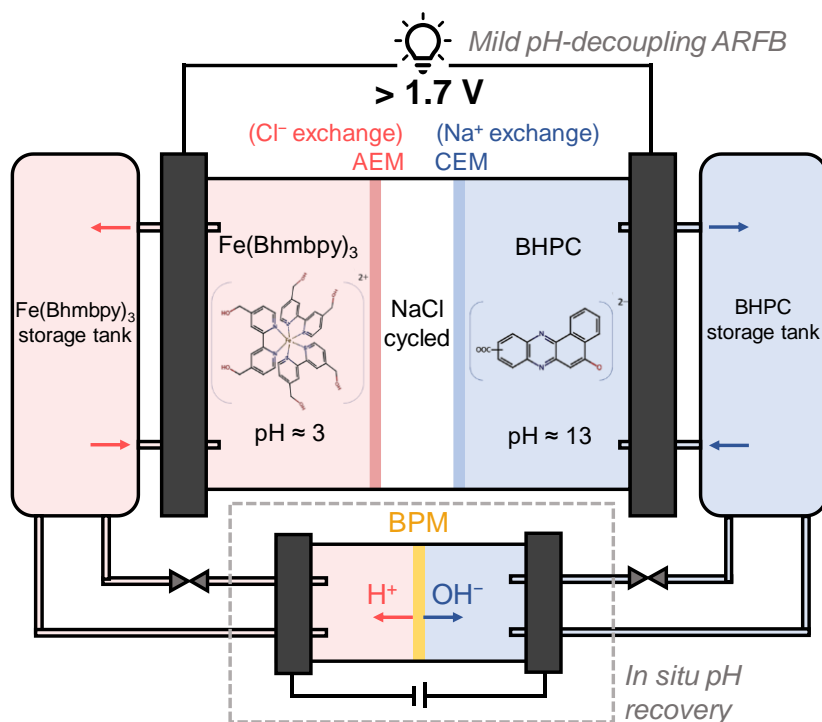
1 Harvard John A. Paulson School of Engineering and Applied Sciences, Cambridge, MA, USA.

2 Department of Chemistry and Chemical Biology, Harvard University, Cambridge, MA, USA 3

These authors contributed equally: Dawei Xi and Abdulrahman M. Alfaraidi

* E-mail: gordon@chemistry.harvard.edu; richardliu@chemistry.harvard.edu; maziz@harvard.edu

TOC:

Abstract:

Aqueous redox flow batteries (ARFBs) constitute a promising technology for grid-scale electricity storage, but it is challenging to implement cell voltages exceeding the 1.23 V thermodynamic water splitting window with high Coulombic efficiency and long lifetime. pH decoupling – the creation of a pH difference between the negolyte and posolyte – can broaden the operating voltage window and improve long-term operational stability. This penalizes the efficiency, however, due to acid-base crossover induced by the pH gradient. As the voltage of the water splitting window varies linearly with pH whereas crossover fluxes vary exponentially, we employed mildly acidic and mildly alkaline electrolytes to develop a cell with high round-trip energy efficiency at an open-circuit voltage > 1.7 V. Moreover, we implemented an acid-base regeneration system to

periodically restore the negolyte and posolyte pH to their initial values. The combined system exhibits a capacity fade rate of less than 0.07% per day, a round-trip energy efficiency of over 85%, and a Coulombic efficiency of approximately 99%. Cost analysis shows that the tolerance of acid-base crossover could be increased if the pH-decoupling ARFB achieved a higher voltage output and lower resistance. The concept of mild pH-decoupling and pH recovery can be used for various pH-decoupling systems. This work demonstrates principles for addressing critical issues such as lifespan, rate capability, long-term practicability, and energy efficiency in pH-decoupling ARFBs, providing guidance for the design of the next generation of high-voltage ARFBs.

Introduction

The need for decarbonization, the advantages of electrical-grid decentralization, and the intermittency of wind and solar energy are motivations for the development of grid-scale storage technologies.[1,2] The aqueous redox flow battery (ARFB) is a promising solution, featuring safety, the decoupling of energy and power capacities, and potential long lifetime, recyclability, and low cost. Redox-active materials have been rapidly developed to approach the requirements for practical grid-scale storage.[3,4]

Despite the advantages of ARFBs, the 1.23 V thermodynamic water splitting window presents practical challenges. Competing water splitting reactions can compromise the Coulombic efficiency of the cell[5,6] and rapidly drive the two sides of the cell out of balance, greatly cutting the operational lifetime.[6-9] Operation of ARFBs at higher voltage output is a potential pathway to achieving increased energy density, higher output power, and lower capital cost, all of which improve the techno-economy and operational flexibility of the cell.[10] Efforts have been put into designing redox-active species that allow higher cell voltage and developing conditions in which water-splitting kinetics remain sluggish[6,9]. Recently, pH-decoupling ARFBs, which contain negolytes (negative electrolytes) and posolytes (positive electrolytes) at different pH, have attracted increasing attention. By employing specialized ion-selective membranes and bipolar membranes[11,12], single-membrane pH-decoupling ARFBs have been demonstrated. Multi-chamber cell structures have also been demonstrated to decouple the pH of negolyte and posolyte.[13-17] For example, by using a three-chamber, two-membrane flow battery design, pH-decoupling ARFBs achieved record high voltage and power output.[14,17,18] However, all previously reported pH decoupled systems suffer from severe proton/hydroxide crossover due to the pH difference across the membrane. This results in short lifetimes and low overall energy efficiency, considering the energy cost required to rebalance the pH difference.[16,19] Adding acid and base to restore the initial pH values is only a superficial solution as, during the long-term operation for ARFBs (years), salt accumulation from the net reaction of exogenous acid and base can deteriorate the cell. Longevity of the pH decoupled systems is an important criterion for practical deployment,[20] yet none of the developed pH-decoupling ARFBs has been proven to be long-term practicable.

In this work, we implemented a mild pH-decoupling design with a pH-difference recovery system to address this critical obstacle. Because the thermodynamic water-splitting voltage varies linearly with pH whereas crossover fluxes vary exponentially, by reducing the strength of the acidic and alkaline electrolytes we have significantly reduced proton/hydroxide crossover while maintaining stable cycling with an open-circuit voltage more than half a volt beyond the 1.23 V threshold. Even pH in cathode and anode are only mildly decoupled, the spare room for developing and utilizing high voltage redox molecules can be largely broadened. A redox pair of benzo[a]hydroxyphenazine-7/8-carboxylic acid[21] (BHPC) and tris(4,4'-bis(hydroxymethyl)-2,2'-bipyridine)iron dichloride[22] (Fe(Bhmbpy)$_3$) that function in mild alkaline and acidic conditions,

2

respectively, were chosen to demonstrate the performance of this mild pH-decoupling design. To compensate for remaining acid-base crossover, the pH difference is intermittently recovered using an acid-base regeneration cell, which does not require exogenous acid or base and thereby avoids salt accumulation. Because of the low observed crossover flux, the energy cost of this pH-recovery process is negligible. We achieved a stable high-voltage ARFB with a fade rate lower than 0.07% per day ($< 0.002\%$ per cycle), overall round-trip energy efficiency higher than 85% (pH recovery energy cost included), Coulombic efficiency around 99%, and peak power density of $140\,\mathrm{mW\,cm^{-2}}$. The cell was cycled continuously for over one week while maintaining its pH difference with pH recovery, demonstrating the suitability of the design for practical long-term operation. This approach has resulted in one of the most stable high-voltage ARFB performances to date. We further demonstrate other pH-decoupling cell structures and different aqueous redox chemicals utilizing the concept of mild pH-decoupling and pH-difference recovery, guiding the design of pH-sensitive or pH-instable systems.

Acid-base crossover in pH-decoupling systems

Our design, using a three-chamber two-membrane cell structure with an acid-base generator, is illustrated in **Fig. 1a**. The three-chamber two-membrane cell was selected as the model system due to the transparency it provided for the study of proton/hydroxide crossover. We selected Fe(Bhmbpy)$_3$ at pH $2 - 4$ with a supporting electrolyte of NaCl/HCl for the positive terminal[22] and BHPC at pH around 13 with a supporting electrolyte of NaCl/NaOH for the negative terminal.[21] The open circuit voltage (OCV) of this cell is approximately 1.75 V. An anion exchange membrane (AEM) and a cation exchange membrane (CEM) were used to separate the acidic positive and alkaline negative terminals, respectively, from the center chamber. NaCl solution is cycled in this center compartment between the two membranes, and pH sensors were inserted in all three chambers' electrolyte tanks for real-time pH monitoring. To counteract any remaining proton/hydroxide crossover processes, the posolyte and negolyte tanks were also connected to a bipolar membrane sub-cell (BPM sub-cell) for periodic pH recovery. During its operation, the BPM sub-cell reduces the posolyte and oxidizes the negolyte, dissociating water into protons and hydroxide, generating acid and base for pH-difference recovery. This BPM sub-cell could be small, relative to the main cell, and operate at intervals for periodic pH recovery. The sub-cell can also operate at steady state under constant current for *operando* pH recovery. Because the operation of *operando* pH recovery can always maintain the electrolyte pH, we chose the periodic pH recovery to show the change during cell cycling.

To achieve ion type selectivity, we utilized AEMs and CEMs to separate the acidic and alkaline sides, respectively. In this system, sodium cations and chloride anions serve as the major charge carriers. The main charge carrier concentration is almost identical across the liquid junctions of the two membranes, and thus the battery open circuit voltage is directly determined by the difference between the two electrode potentials. Although hydroxide and protons are mainly excluded by the CEM and AEM, respectively, the pH gradient that exists in the cell nevertheless causes undesired crossover of these ions. [23]
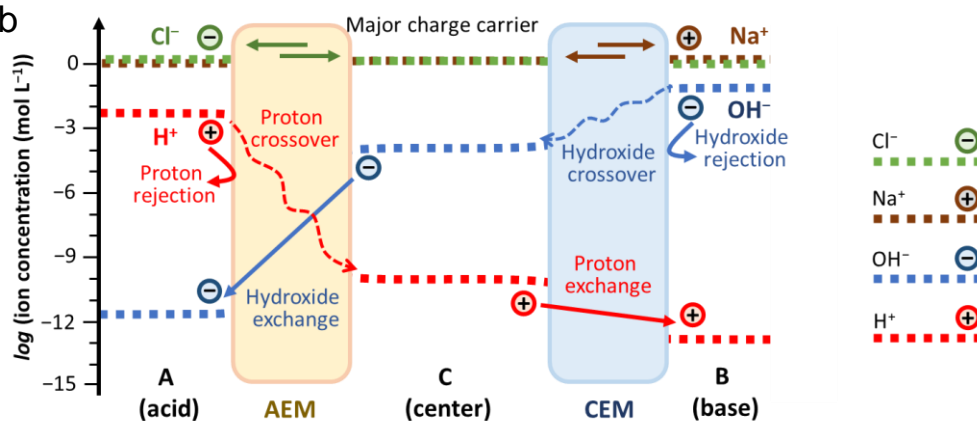
3
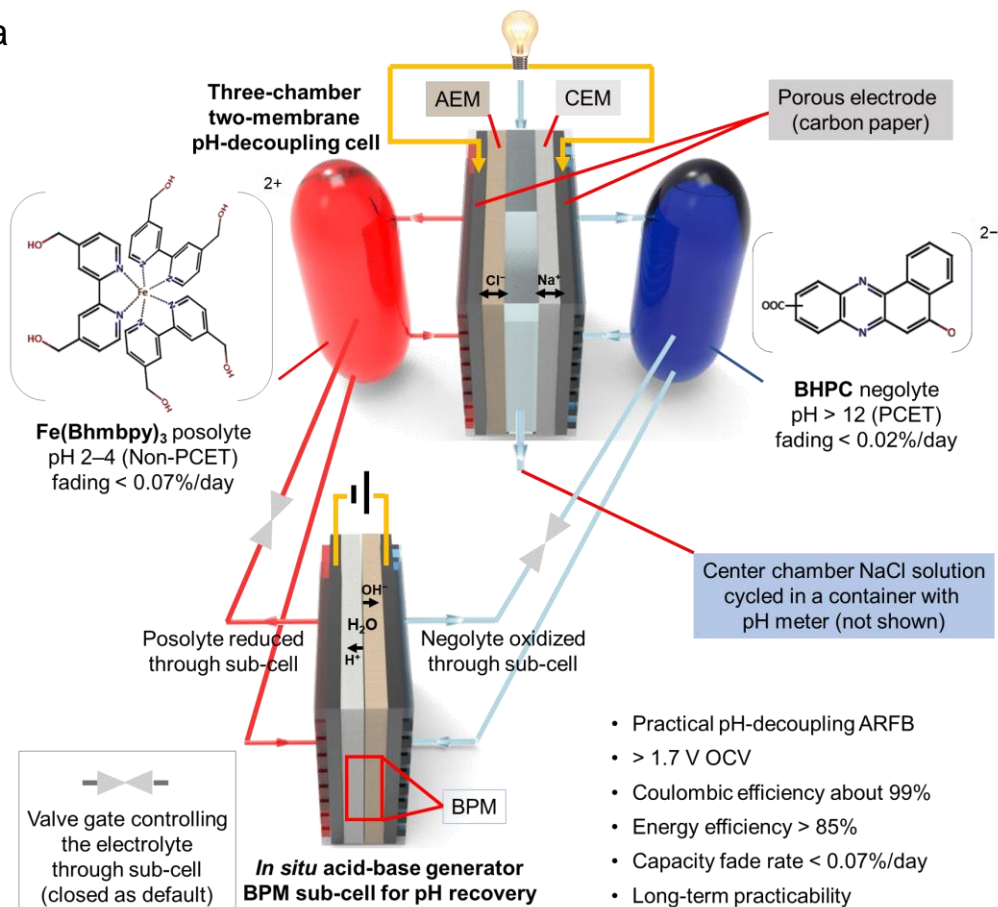
Figure 1 | Cell structure and charge carrier migration. a, Schematic of a three-chamber two-membrane cell with a pH recovery sub-cell. Electrolytes, cell components, and sensors are labeled accordingly. Electrolyte flow is indicated with arrows. Electrolytes are pumped into the BPM sub-cell for acid-base regeneration when needed (pumps not shown). **b,** Ion concentration and flow across three chambers. Sodium and chloride ions are the major charge carriers.

A cross-sectional view of the ion concentration profile, and transport expected during operation of the cell is shown in **Fig. 1b**. Most hydroxide ions are blocked by the CEM. However, small amounts of hydroxide ions can crossover and increase the center chamber pH before eventually exchanging through the AEM. The symmetric process can occur for protons. The crossover rate of protons and hydroxide can be described by **Equations 1** and **2**. $[H^+]_A$, $[H^+]_C$, and $[H^+]_B$ represent the proton concentrations in acidic, center, and basic chambers, respectively; their chemical compositions are assumed to be spatially uniform. $[OH^-]_A$, $[OH^-]_C$, and $[OH^-]_B$ represent the hydroxide concentrations in acidic, center, and basic chambers, under equilibrium of water ionization with $[H^+]$ in each chamber. A_{mem} represents the membrane area, V_A represents acidic chamber volume, and l_{AEM} represents the thickness of AEM. P represents the permeability coefficient of ions though the membrane. M represents the ion-migration coefficient inside the membrane due to the applied electric field. j represents the signed ionic current, with direction pointing from acidic to alkaline chamber as positive.

$$-\frac{d\,[H^+]_A}{d\,t} = \frac{A_{mem}}{V_A}\left(P_{H^+}^{AEM}\frac{[H^+]_A - [H^+]_C}{l_{AEM}} + M_{H^+}^{AEM}j + P_{OH^-}^{AEM}\frac{[OH^-]_C - [OH^-]_A}{l_{AEM}} + M_{OH^-}^{AEM}j\right) \tag{1}$$

$$-\frac{d\,[OH^-]_B}{d\,t} = \frac{A_{mem}}{V_B}\left(P_{OH^-}^{CEM}\frac{[OH^-]_B - [OH^-]_C}{l_{CEM}} + M_{OH^-}^{CEM}j + P_{H^+}^{CEM}\frac{[H^+]_C - [H^+]_B}{l_{CEM}} + M_{H^+}^{CEM}j\right) \tag{2}$$

$$J_{crossover} = \max\left(-\frac{d\,[H^+]_A}{d\,t}\frac{V_A}{A_{mem}}, -\frac{d\,[OH^-]_B}{d\,t}\frac{V_B}{A_{mem}}\right) \tag{3}$$

The ion migration coefficients can be expressed as:

$$M_{H^+}^{AEM} = D_{H^+}^{AEM}[H^+]_{AEM}\frac{ZF}{\sigma^{AEM}RT}; \quad M_{OH^-}^{AEM} = D_{OH^-}^{AEM}[OH^-]_{AEM}\frac{ZF}{\sigma^{AEM}RT};$$

$$M_{OH^-}^{CEM} = D_{OH^-}^{CEM}[OH^-]_{CEM}\frac{ZF}{\sigma^{CEM}RT}; \quad M_{H^+}^{CEM} = D_{H^+}^{CEM}[H^+]_{CEM}\frac{ZF}{\sigma^{CEM}RT}.$$

Here, D represents the diffusivity of an ion in a membrane. Z is the signed charge number of the ion. F is Faraday's constant. R is the universal gas constant and T is the absolute temperature. σ is conductivity of the membrane in the electrolyte. As shown in Fig 1b, we refer to $P_{OH^-}^{CEM}\frac{[OH^-]_B - [OH^-]_C}{l_{CEM}} + M_{OH^-}^{CEM}j$ as the hydroxide crossover terms (through the CEM) and $P_{H^+}^{AEM}\frac{[H^+]_A - [H^+]_C}{l_{AEM}} + M_{H^+}^{AEM}j$ as the proton crossover terms (through the AEM). Similarly, we refer to $P_{OH^-}^{AEM}\frac{[OH^-]_C - [OH^-]_A}{l_{AEM}} + M_{OH^-}^{AEM}j$ as the hydroxide exchange terms (through the AEM) and $P_{H^+}^{CEM}\frac{[H^+]_C - [H^+]_B}{l_{CEM}} + M_{H^+}^{CEM}j$ as the proton exchange terms (through the CEM). The net acid-base crossover flux ($J_{crossover}$) of the system can be described as in **Equation 3**. The equivalent acid-base crossover current density can be calculated by multiplying net acid-base crossover flux with Faradaic constant.

In the initial state, the center-chamber NaCl solution is at near-neutral pH. Taking our specific system as an example, hydroxide crossover flux from the alkaline negolyte (pH 13) is larger than proton crossover flux from the acidic posolyte (about pH 3). Thus, over time, the pH of the center chamber drifts to higher values. Higher center pH will increase the hydroxide exchange rate through the AEM, and any exchanged hydroxide ion entering the acidic chamber will be neutralized by a proton. Thus, the net effect of hydroxide exchanged across the AEM is the loss of protons in acidic chamber. Eventually, the center chamber pH will reach steady state, at which point the net flux of protons and the net flux of hydroxide into the center chamber are equal.

5

A large amount of crossover will destroy the designed pH gradient by driving all chambers toward identical pH values, resulting in diminished operating voltage and possibly instability of the redox-active molecules.

To characterize the hydroxide and proton crossover flux independently for each membrane under alternating electric field during charging and discharging, we constructed a two-chamber supercapacitor cell, with one chamber having an alkaline (or acidic) initial state as crossover source and the other chamber having a near-neutral pH as acceptor chamber (**Fig. 2a**). The two sides were supported by NaCl solutions and separated by a CEM (or AEM) for hydroxide (or proton) crossover testing. Supercapacitors can be charged and discharged through ion adsorption, without introducing redox active molecules that could interfere with the measurements. Ideally, only Na^+ (or Cl^-) ions should cross the membrane when the cell is subjected to an alternating current. However, ion-selective membranes cannot perfectly reject hydroxide ions and protons, leading to a pH change that can be observed in the initially pH-neutral acceptor chamber.
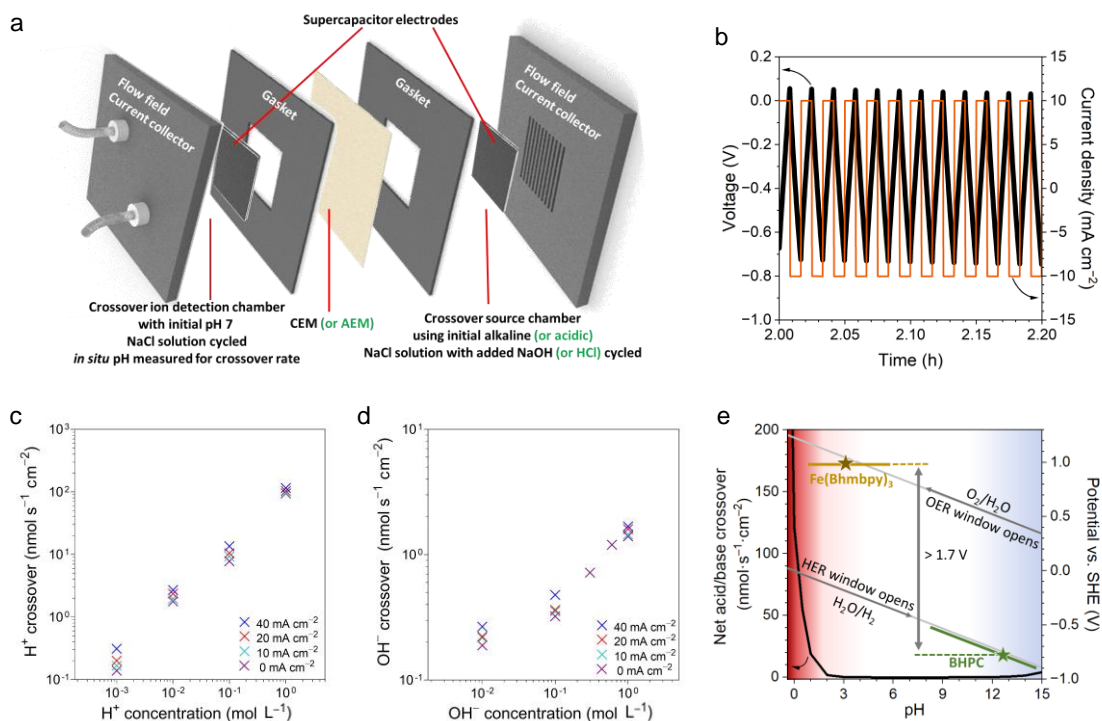
Figure 2 | Proton/hydroxide crossover flux through AEM/CEM under applied electric field. a, Schematic of a supercapacitor cell used to quantify hydroxide and proton crossover. Electrolytes, cell components, and sensors are labeled accordingly. Source and acceptor chamber electrolytes are fed by separate tanks. **b,** Temporal profile of voltage and current density during the crossover supercapacitor test for pH 0 acid source at 10 mA cm^{-2}. **c,** Proton crossover fluxes through DSV-N as a function of proton concentration in source chamber for various current densities. **d,** Hydroxide crossover fluxes through E620 as a function of hydroxide concentration in source chamber for various current densities. **e,** Pourbaix diagram with net acid-base crossover flux. The black curve shows the net acid-base crossover flux calculated from (**c,d**). Background shading is used to indicate the severity of acid-base crossover with DSN-N or E620 (red for acid crossover, blue for base crossover, corresponding to the black crossover flux curve). The thermodynamic

water splitting window is identified by grey lines. Redox potentials of BHPC and Fe(Bhmbpy)$_3$ are labeled in the diagram.

Depending on their selectivity and molecular structure, different ion-selective membranes exhibit varying rates of crossover. We selected well-established and commonly used ion-selective membranes: Fumasep E-620K (E620) as the CEM and Selemion DSV-N (DSV-N) as the AEM, for evaluation of crossover fluxes, which were estimated by tracking the pH change of the initially neutral acceptor solution (**Fig. S1**). To determine the effect of proton/hydroxide concentration and applied current density on the crossover fluxes, we varied the initial pH for the source chamber side and applied different alternating current densities in the constructed supercapacitor cell, mimicking the charge-discharge cycles in during real battery operation. A typical voltage and current density profile is shown in **Fig. 2b**. The operation parameters were chosen to avoid water splitting so that the pH change is affected only by crossover. Then the rate of pH change was normalized by solution volume and membrane area into crossover flux. **Fig. 2c** and **2d** show the measured crossover fluxes for protons and hydroxide, respectively. In both cases, the applied current density has only a minor effect on the magnitude of the crossover fluxes. Conversely, the initial concentration of ions in the source chamber has a significant, almost linear, impact on the crossover flux. Therefore, we can simplify the net crossover flux into $J_{crossover} = \max\left(C_{H^+}^{AEM}[H^+]_A, C_{OH^-}^{CEM}[OH^-]_B\right)$ in which, $C_{H^+}^{AEM}$ is the crossover coefficient of protons through the AEM and $C_{OH^-}^{CEM}$ is the crossover coefficient of hydroxide through the CEM.

By fitting the data of Fig. 2c and Fig. 2d, we found that $C_{H^+}^{DSV-N}$ is about 1.7 µm s^{-1} and $C_{OH^-}^{E620}$ is about 0.015 µm s^{-1} under zero current. As a result, using these two membranes, concentrated strong acid solutions should be used with particular caution in order to avoid energy efficiency loss associated with proton crossover in pH-decoupling ARFBs.

We hypothesized that rapid crossover can be prevented while maintaining high cell voltage through "mild" pH decoupling. Operation at pH 13 and 3 (a difference of 10 pH units) can still allow an OCV higher than 1.7 V if the negolyte and posolyte are chosen appropriately, as seen in **Fig. 2e**. By using milder acid and base than previous pH-decoupling batteries, we can still achieve relatively high voltage while exponentially reducing the unwanted acid-base crossover flux ($C_{H^+}^{DSV-N}[H^+]_A \approx 0.1$ nmol s^{-1} cm^{-2}, $C_{OH^-}^{E620}[OH^-]_A \approx 0.2$ nmol s^{-1} cm^{-2}, under zero current), thus approaching an optimal balance in the tradeoff between operating voltage vs. energy inefficiency and instability due to acid-base crossover associated with the membranes we used.

A mild pH-decoupling battery with pH-recovery

As a proof of concept, Fe(Bhmbpy)$_3$ and BHPC were paired in the mild pH-decoupling ARFB. The redox potential of each molecule was first evaluated in a single three electrode cell (**Fig. S2, S3**). The redox potential of Fe(Bhmbpy)$_3$ is pH-independent, but that of BHPC, which undergoes proton-coupled electron transfer, is pH-dependent. Their redox potentials at different pH values are indicated by solid lines in **Fig. 2e**. Operational conditions for Fe(Bhmbpy)$_3$ and BHPC were carefully optimized through extensive evaluation (**Fig. S4-10**). In our optimized AFRB, Fe(Bhmbpy)$_3$ was employed at pH 2 – 4 and BHPC at pH 13. Furthermore, we chose Fe(Bhmbpy)$_3$ to be the capacity-limiting side because of its higher fade rate (**Fig. S11**).[22]

7

Fig. 3a and **3b** show the temporal evolution of the pH of the reservoirs and the cell capacity and Coulombic efficiency, measured for a test cell in which the negolyte contained 0.1 M Na_2BHPC at pH 13 (20 mL), while the posolyte contained 0.1 M $Fe(Bhmbpy)_3Cl_2$ at pH 3 (10 mL). 1.0 M NaCl was used as a supporting electrolyte on both sides, with added NaOH or HCl to adjust the pH. 20 mL 1.3 M NaCl was cycled in the middle chamber. An E620 CEM separated the negolyte from the middle chamber and a DSV-N AEM separated the posolyte from the middle chamber. This cell was cycled with the standard constant-current followed by constant-voltage (CCCV) protocol at 20 mA cm^{-2} with voltage cut-off values of 2.0 V and 0.7 V during charge and discharge, respectively, held until the current density dropped below a current cutoff value. The cell accessed >95% of its theoretical capacity and exhibited an average Coulombic efficiency of 99%, presumably limited by the self-discharging of the iron-based posolyte.[22]

Starting with the simple approach of restoring the initial pH difference through the simultaneous addition of acid and base, 0.1 mL of 1 M HCl was added to the posolyte side and 0.1 mL of 1 M NaOH was added to the negolyte side when pH had drifted significantly from its initial value. The amount and time of adding exogenous acid-base can be estimated according to the calculated net acid-base crossover fluxes. These addition events are apparent from the discontinuities in the pH data shown in **Fig. 3a**. The cell was cycled over 18 days, and high Coulombic efficiency and a low capacity fade rate were observed (**Fig. 3b**). The voltage-capacity profiles of this battery during three representative cycles are shown in **Fig. 3c**, demonstrating its excellent stability. The plateau near 0.8 V during discharge has been identified as the reversal of a dimerization side-reaction of $Fe(Bhmbpy)_3$.[22]

Because the Coulombic efficiency (CE) of the system is limited by the posolyte side, the cell drifted from perfect charge balance toward reduction of both sides over roughly 13 days (Fig. 3b, day 13). To counteract this imbalance, we briefly exposed the reduced negolyte to air, which brought the cell back into balance. Negolyte exposure to air is a simple and general strategy to restore out-of-balance ARFBs when a parasitic reduction of the posolyte limits the Coulombic-efficiency.[24,25] We also tested a capacity-balanced cell with the same negolyte and posolyte composition. By exposing negolyte to air intermittently to oxidize it back to balanced charge, we were able to run this capacity-balanced cell with similar slow fading and stable voltage output (**Fig. S12**).

A zoomed-in view of the voltage and pH profile for a few cycles is shown in **Fig. 3d**. During cell cycling, the pH of the negolyte oscillated due to proton-coupled electron transfer of BHPC. We attribute the oscillating pH of the posolyte to the reversible dimerization side-reaction of the oxidized $Fe(Bhmbpy)_3$.[22] The posolyte pH oscillates between 2 and 5, representing a small change in proton concentration (10^{-2} mol L^{-1}).

8

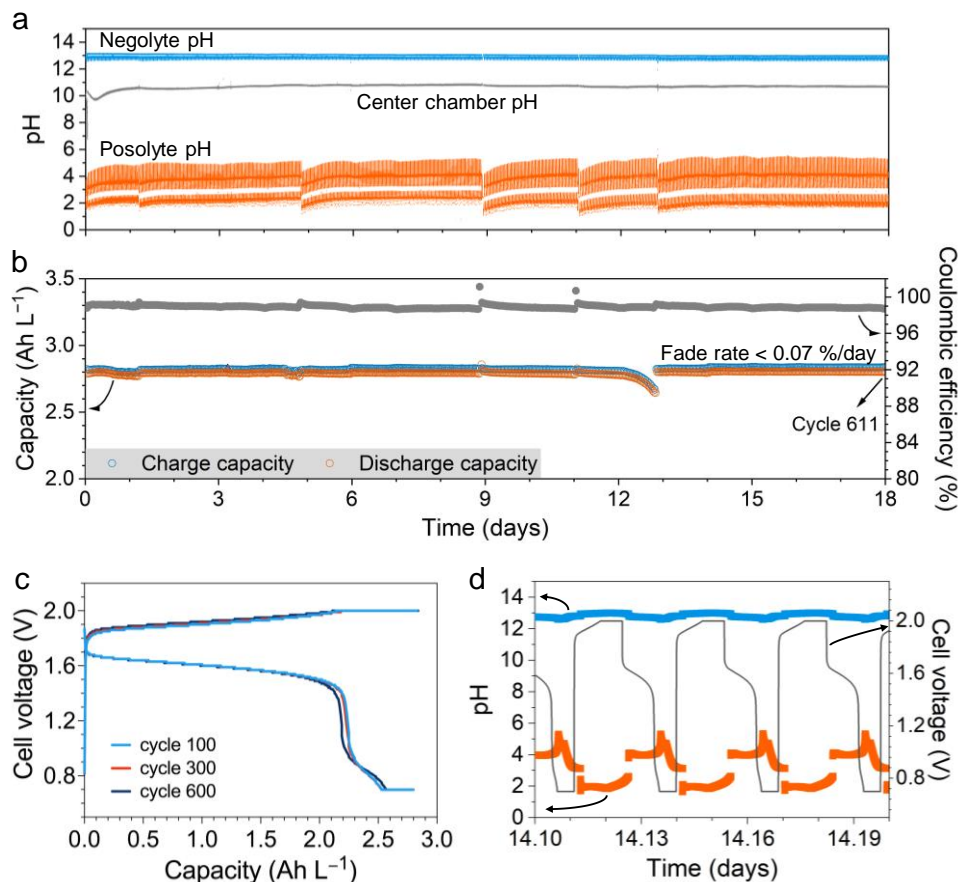**Figure 3 | Long-term performance of high-voltage mild pH-decoupling battery. a,b** Negolyte pH, posolyte pH, capacity, and coulombic efficiency in pH-decoupled ARFB during long-term cycling. The cell was operated with a constant current (20 mA cm^{-2}) followed by constant potentials of 2.0 V (charging) and 0.7 V (discharging) during 18 days of operation at room temperature. The cell was assembled with a negolyte comprising 0.1 M BHPC in 1 M NaCl at pH 13 and a posolyte comprising 0.1 M Fe(Bhmbpy)$_3$ in 1 M NaCl at pH 3. The middle chamber was circulated with 1.3 M NaCl solution and separated from the side chambers by a CEM and an AEM. **c,** Charge-discharge voltage-capacity profiles from selected cycles. **d,** Zoomed-in temporal profile of cell voltage and pH of negolyte and posolyte during a few cell cycles.

Repeated addition of exogenous acid and base into the reservoirs to maintain the pH difference is not viable in the long term. Over months of cell operation, dissolved salts in the cell will accumulate through the net acid-base crossover reaction: HCl + NaOH = NaCl + H$_2$O. Because these salts are difficult to remove, they will eventually reach saturation and precipitate, leading to cell failure. To avoid this trajectory, we used a BPM sub-cell to recover the pH-instability by dissociating water into protons and hydroxide ions during discharging of the electrolytes. In this way, no exogenous materials are introduced into the system.

To demonstrate the effectiveness of this pH recovery strategy, we pumped partially charged electrolytes through a BPM sub-cell and discharged them across the BPM. Linear-sweep

9

voltammetry (LSV) was applied to study the polarization of the BPM cell (**Fig. 4a**). In Fig. 4a, we also show the LSV toward discharge in the three-chamber cell. The voltage difference between the two discharge curves is primarily from the energy cost of water dissociation. Therefore, the difference between them can be interpreted as the acid-base recovery energy cost. More detailed polarization curves of the BPM using different pH pairs were also recorded in a four-electrode setup[26] (**Fig. S13**). During pH recovery, we applied 40 mA cm^{-2} constant current density on the BPM cell through an independent potentiostat. A typical BPM cell voltage profile during pH recovery is shown in **Fig. 4b** (dark blue curve, orange-highlighted region). The cell voltage during a few CCCV cycles before and after recovery is also shown. The recovery discharge voltage is lower than the normal cycling discharge voltage, the difference resulting from the thermodynamic water dissociation potential plus the overpotential and resistance of the BPM. The ideal thermodynamic cost of generating 1 M each of acid and base from water is equivalent to 0.83 V, based on assumptions of unit activities of protons and hydroxide in their respective membrane layers. This additional applied voltage creates an energy efficiency loss associated with pH recovery. If the acid-base crossover is rapid, a large amount of charged electrolyte will have to be discharged in the BPM sub-cell, and the resulting energy efficiency penalty will be severe, as shown in **Fig. S14**. When the amount of acid-base that must be recovered approaches the amount of charged electrolyte (equivalent acid-base crossover current density exceeds about 10% of the current density for battery cycling), the loss in round-trip energy efficiency of the pH-decoupling ARFB will make it impractical. In contrast, in our mild pH-decoupling scheme, low acid-base crossover fluxes can be achieved, and just four pH recovery cycles (each with a capacity of about 6 mAh) were sufficient to keep the system stable for over a week (**Fig. 4c-e**, at vertical arrows). After each recovery cycle, the pH of the negolyte increased (Fig. 4b, light blue trace, and Fig. 4c), while the pH of the posolyte decreased (Fig. 4b, orange trace, and Fig. 4d). The voltage-capacity profile shows stable cycling after pH recovery (**Fig. S15**). The resistance of the BPM increased after two weeks of usage; we attribute this to the degradation of the catalytic layer in the BPM. BPMs with lower resistance, lower water dissociation overpotential and higher stability can further increase the practicability of these designs. pH buffering electrolytes can be applied to help maintain a more stable pH during pH recovery intervals. It is worth noting that the pH-difference recovery through BPM sub-cell does not necessarily have to be periodic. pH recovery can be *operando* and conducted under steady state, by discharging the electrolyte in the BPM sub-cell at a constant current matching the equivalent acid-base crossover current. Consequently, the energy cost from pH recovery presents as a Columbic inefficiency during the cycling of the main ARFB. When the equivalent acid-base crossover current density is small, the round-trip energy inefficiency caused by pH recovery can be negligible, and the geometric area of the BPM sub-cell running under a certain current density can be small enough that it will not apparently increase the capital cost of the battery system.
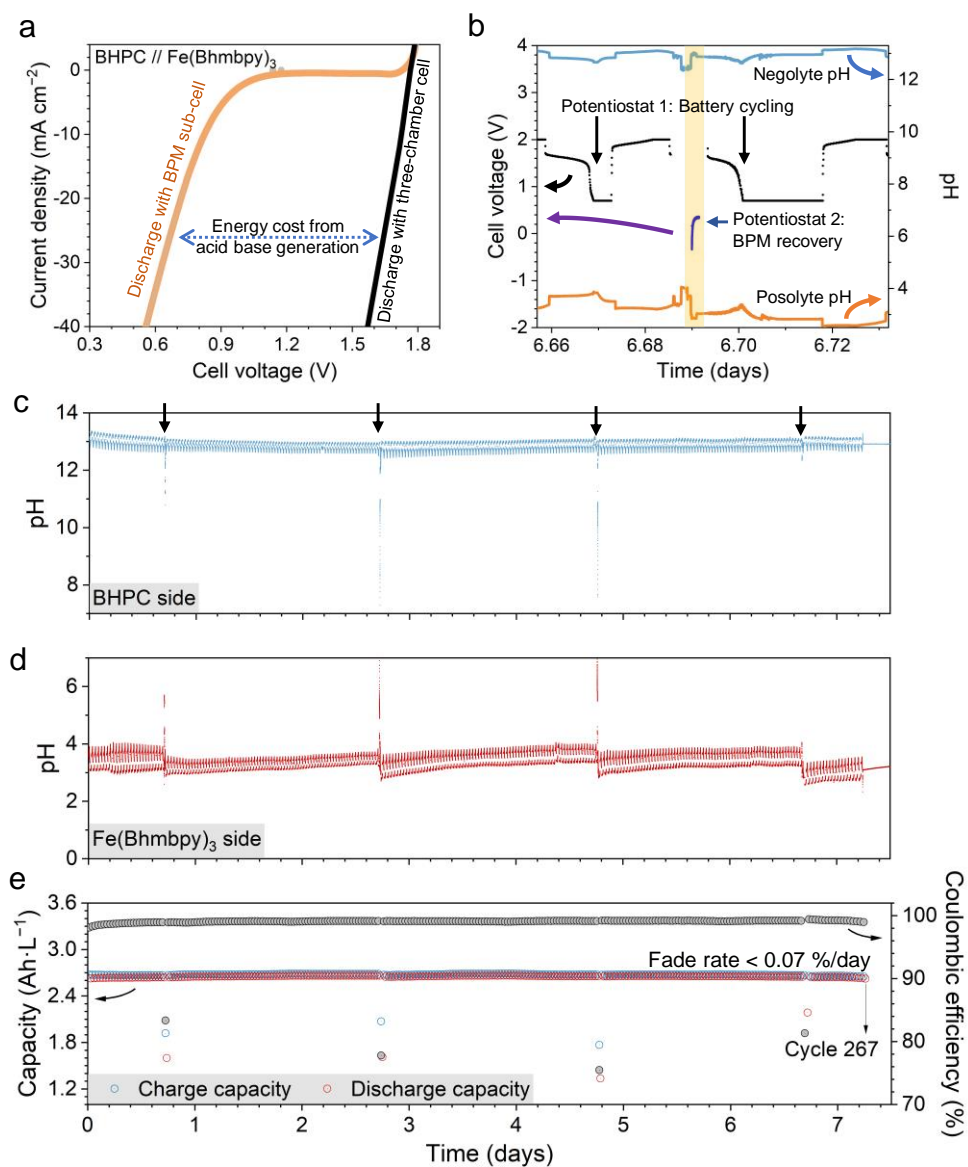
10

Figure 4 | Performance of the BPM sub-cell, and long-term ARFB cycling with pH recovery. a, LSV curve of the BPM sub-cell and three-chamber cell. Electrolytes are pumped into BPM sub-cell at 60–90% SOC. LSV curve was collected with a sweep rate of 3 mV s^{-1} to discharge the electrolytes. The OCV is about 1.75 V, and water dissociation starts around 0.95 V, indicating a voltage cost of around 0.8 V at 5 mA cm^{-2}. **b,** Cell voltage and pH during a few cell cycles and during pH recovery. The CCCV protocol was applied during cell cycling. The BPM sub-cell recovery phase is highlighted in orange. During recovery, potentiostat 1 was disconnected, and the BPM sub-cell was independently connected to potentiostat 2. Charged electrolytes from the three-chamber cell were pumped into the sub-cell. 40 mA cm^{-2} was applied until pumped electrolytes discharged by approximately 6 mAh. *In situ* pH measurements show pH recovery. **c,d,e,** Negolyte pH, posolyte

pH, capacity, and Coulombic efficiency in pH-decoupling ARFB during long-term cycling with pH recovery. Vertical arrows indicate four pH recovery operations. During recovery, electrolytes were pumped through a BPM sub-cell and discharged to dissociate water. The capacity fade rate was smaller than 0.07%/day, and Coulombic efficiency was around 99%. The Coulombic efficiency drop during recovery was due to capacity utilization during BPM sub-cell discharge.

To increase energy efficiency and power density of the system, we further optimized the cell structure. The resistance of the three-chamber cell was first studied by varying the thickness of the center chamber (**Fig. S16-17**). To achieve a sub-millimeter center chamber thickness, we kept the AEM and CEM separated by only 200 μm with a porous spacer in the electrically active region, while preserving good sealing by extending them peripherally along opposite sides of the center-chamber (**Fig. S18**). Ohmic resistance can be linearly decreased by a reduction in the center chamber thickness (**Fig. S19**). Center-chamber NaCl concentration, temperature, and flow rate were also investigated and optimized (**Fig. S20-24**). With these modifications to the center chamber and cycling conditions, the high-frequency ohmic resistance of the system was reduced to nearly the sum of two membrane resistances (**Fig. S25**).

We then conducted a polarization and galvanostatic analysis of the optimized cell structure with a negolyte composition of 0.1 M BHPC at pH 13 (10 mL) and a posolyte composition of 0.1 M Fe(Bhmbpy)$_3$ at pH 3 (4.5 mL). The potential was held at the end of discharge in order to recover Fe(Bhmbpy)$_3$ from dimerization. Polarization curves and galvanic power densities are shown in **Fig. 5a**. The three-chamber pH-decoupling battery reached a peak power density of 140 mW cm^{-2} at 80% SOC. **Fig. 5b** shows the OCV of the cell, increasing from 1.69 V at 20% SOC to 1.8 V at 90% SOC. The high-frequency area-specific resistance (ASR) of the battery averaged 2.85 Ω cm^2 while the average polarization ASR across all SOC was 3.82 Ω cm^2. These values indicate that most of the cell's overall resistance is attributable to the resistance of the membranes. **Fig. S26** depicts the voltage profile of the cell at different current densities, from which we extracted the Coulombic efficiency, capacity utilization, and round-trip energy efficiency for **Fig. 5c**. At 40 mA cm^{-2}, this high-voltage cell exhibits 80% round-trip energy efficiency, which indicates that voltage losses are minimized due to the optimized design of the three-chamber cell.
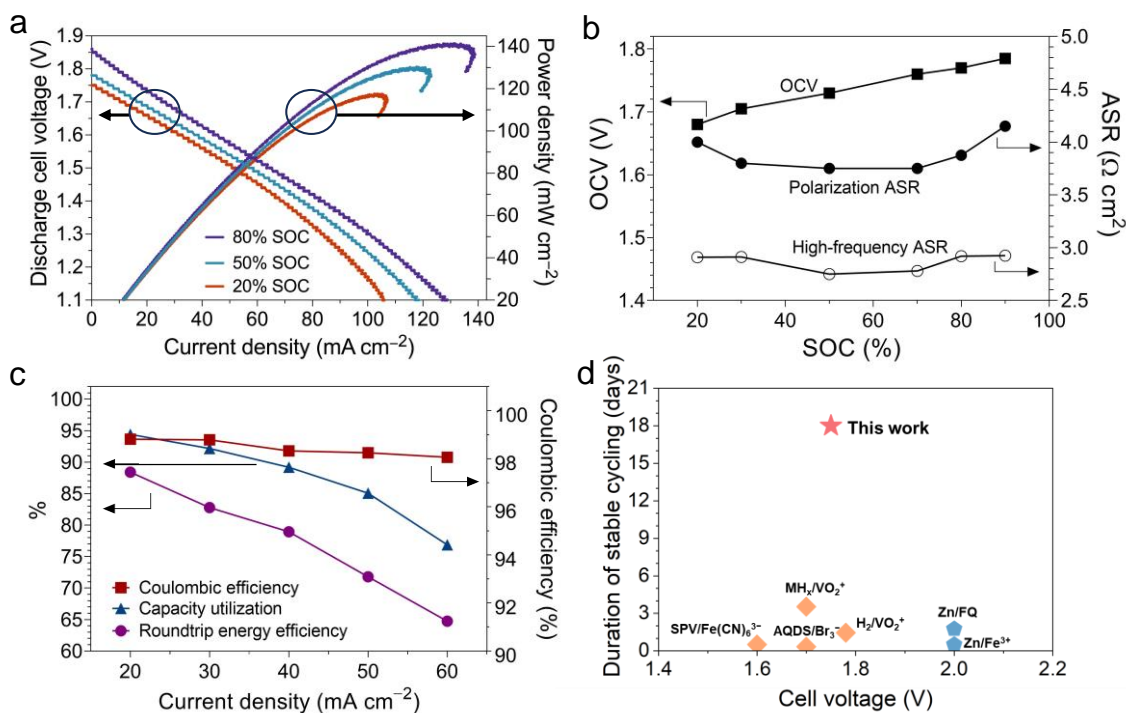
Figure 5 | Polarization performance of the system and comparison of pH-decoupling systems. a, Cell voltage and power density during discharge of three-chamber acid-base ARFB with 0.1 M BHPC in 1 M NaCl at pH 13 (adjusted by NaOH) as negolyte and 0.1 M Fe(Bhmbpy)$_3$ in 1 M NaCl at pH 3 (adjusted by HCl) as posolyte. The 200-μm-thick middle chamber was circulated with 2 M NaCl solution and separated from the side chambers by E620 as CEM and DSV-N as AEM. **b,** Dependence on SOC of OCV and ASR near OCV for the described cell. **c,** Capacity utilization and Coulombic and round-trip energy efficiencies vs. applied current density for the cell. **d,** Reported stable cycling duration of previous acid-base ARFBs compared to the current work. Orange points represent BPM pH-decoupling ARFBs. Blue points represent two-membrane pH-decoupling ARFBs. The star represents this work, featuring the only long-term practical pH-decoupling ARFB that rebalances the lost acid-base during operation.[11,12,14,23,27,28]

With this mild pH-decoupling setup with pH recovery, exhibiting a crossover flux smaller than 0.3 nmol s^{-1} cm^{-2}, we have a negligible energy and capital cost penalty due to the recovery system. Thus, we have realized the first long-term practical pH-decoupling ARFB, theoretically permitting an indefinite duration of operation and demonstrating dramatically longer operation with slower fading compared to previous examples, as illustrated by the duration of stable cycling reported in **Fig. 5d**. We report this comparison to emphasize that future pH-decoupling cell designs should place a greater focus on long-term operation possibility and technoeconomic considerations.[13,17,29] Higher voltage output and lower ASR, can both be beneficial because it lowers the relative cost of pH recovery and therefore, can make higher acid-base crossover rates tolerable.

13

Other applications and technoeconomic calculations

The application of our cell design and recovery concept is not limited by the redox couple we showed. To illustrate the generalization of this system to other redox chemistries, we demonstrated cycling of three other pairs of electrolytes in mild pH-decoupling ARFBs. Fe(Bhmbpy)$_3$ at pH 3 and di-butanoate ether anthraquinone[30] (DBEAQ)[30] at pH 12 were used to demonstrate the cell performance under milder pH difference with non-PCET electrochemistry in both sides (**Fig. S27-28**). This milder pH-decoupling three-chamber cell exhibited better stability and required infrequent addition of acid and base. With pH recovery, the cell also showed similar BPM overpotential to that of the model cell with BHPC, and we measured an overall fade rate of $< 0.07\%$ per day with 99% Coulombic efficiency (**Extended Fig. 1; Fig. S29-30**). The polarization test of this cell revealed similar high energy efficiency but a slightly smaller power density because of its lower OCV (**Fig. S31**).

By exchanging the DBEAQ negolyte for Fe(DIPSO),[31,32] an iron complex negolyte species that operates at pH about 13, we achieved a pH-decoupled all-iron ARFB with OCV around 1.8 V (**Extended Fig. 2; Fig. S32-35**). Maintaining high pH is essential for the stability of Fe(DIPSO), as it precipitates from solution at lower pH. Long-term cycling with either exogenous acid-base addition or pH recovery exhibited a low fade rate and low pH recovery cost.

To further evaluate the performance of the three-chamber and pH recovery cell combination, we utilized a high concentration aqueous redox pair. 2 M FeCl$_3$ (pH 1-3) was paired with 1 M BHPC (pH 13-14, introducing high pH swing) realizing high volumetric capacity. The testing results demonstrated promising cycling performance and successful pH recovery through the BPM cell (**Fig. S36**). However, the results also showed fast capacity fading due to iron ion crossover (Fig. S36c). Towards the practical application of pH-decoupling ARFB, the crossover of redox active molecules has to be controlled. Researchers have developed larger molecules[33], higher charged molecules, or better ion-selective membranes with stronger repulsion against redox active molecules[34-38] to suppress crossover. Another strategy is to develop ARFB systems allowing a mixture of both high-potential and low-potential redox species in both posolyte and negolyte so that crossover is inconsequential.[39]

For higher voltage, pairing Fe(Bhmbpy)$_3$ at pH 3 with Cr chelate 1,3-propylenediaminetertaacetic acid (CrPDTA) at pH 9 can reach an OCV about 2.2 V,[6] with net acid-base crossover flux lower than 0.2 nmol s^{-1} cm^{-2}. Other suitable redox candidates are listed in **Table S1**, from which we can find redox pairs allowing operating our pH-decoupling-recovery design with various values of OCV and crossover flux, maintaining long-term practicability.

To gain insight into the future development of such pH-decoupling systems, we studied the cost penalty from acid-base crossover, by doing a technoeconomic analysis of the penalties that are inherent to any pH decoupled system (**Fig. S37**).[29,40,41] We assumed that the BPM sub-cell operates at a steady-state current density (equal to the equivalent acid-base crossover current) for pH recovery. Consequently, higher acid-base crossover flux leads to higher capital cost associated with a larger BPM sub-cell. This also results in higher energy cost for pH recovery, penalizing the round-trip energy efficiency. Acid-base crossover will be less impactful when using a battery stack with smaller battery area relative to the volume of electrolyte tanks. Because the required geometric battery area for a certain power output decreases roughly as $(ASR) \times (OCV)^{-2}$, an increased OCV cuts the rate of acid-base crossover for a flow battery system with fixed discharge duration, and thereby cuts the BPM cell cost and the energy efficiency penalty of the recovery system. The capital

cost of the three-chamber cell was estimated using a reported technoeconomic model,[10,40] reckoning the additional costs associated with a three-chamber two-membrane setup and a pH recovery system (**Fig. S38**). We estimated the current density of the ARFB as $\frac{0.2\,OCV}{ASR}$. The costs of the recovery system can be acceptable if the increased OCV more than offsets the increased ASR associated with an additional membrane and an additional electrolyte chamber. Although the high capital cost and the high ASR associated with two membranes challenge the commercialization of three-chamber ARFBs (**Fig. S39**), the implementation of mild pH-decoupling can still be useful in other cell designs. [6,24] Because power output and overall ASR appear to be essentially limited by the resistances of the two membranes and because the BPM sub-cell and the energy cost penalty of pH-recovery is determined by the acid-base crossover flux through the two membranes, further development of lower-resistance AEMs and CEMs with low acid-base crossover coefficient is important for pH-decoupling ARFBs.[34,38,42] showing some of the AEMs permit very low proton crossover flux (< 1 nmol s^{-1} cm^{-2}) even working against pH 0 (**Fig. S40**), which is of great promise for future applications in severe pH-decoupling systems.
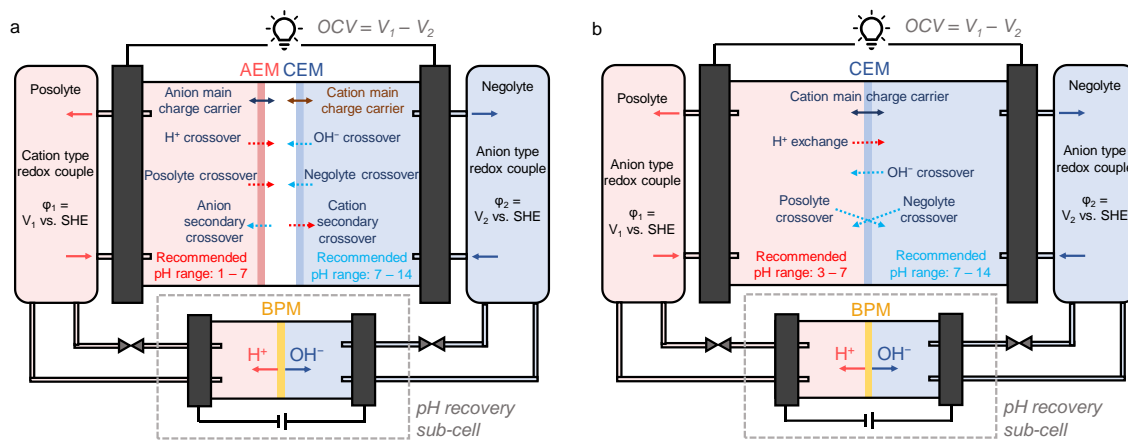
Figure 6 | pH-decoupling ARFBs with pH recovery. a, A three-chamber two-membrane pH-decoupling ARFB with pH recovery. The cell can use concentrated acid and base, while considering the cost of acid-base crossover. **b,** A CEM type single-membrane pH-decoupling ARFB with recovery. The acidic side has to be mild for the main charge carrier to be non-proton cations. Correspondingly, an AEM type single-membrane pH-decoupling ARFB should use mild alkaline electrolyte against acidic electrolyte for the main charge carrier to be non-hydroxide anions.

For other pH-decoupling systems, which always suffer to some extent from acid-base crossover during long-term operation, pH recovery can also be realized.[19,43] Even a small pH difference between the cathode and the anode can enlarge the space for utilization of redox active molecules in high voltage cells. To further demonstrate the capability of utilizing mild pH-decoupling ARFBs with pH recovery, we constructed a single-membrane two-chamber pH-decoupling ARFB that uses KBr/KBr$_3$ (1 M K$^+$, at pH 2 – 5) against CrPDTA (1 M, at pH 9 – 10, buffered by 0.1 M PDTA), separated by only one cation exchange membrane. During cell cycling, because the concentration of K$^+$ is at least two orders of magnitude higher than the concentration of H$^+$, the charge carrier through the membrane is predominantly K$^+$. Meanwhile, hydroxide anions are mostly rejected by the CEM by charge exclusion. Therefore, the net acid-base crossover flux in the system is low, which enables the system pH gradient to be relatively stable. Single-membrane pH-decoupling

ARFBs have higher potential for commercialization and higher tolerance for acid-base crossover flux, due to their increased OCV without extra membranes or chambers compared to conventional ARFBs (**Fig. S41**). The high-frequency ASR of the cell we assembled is about 1.2 Ω cm^2, with an open circuit voltage around 2.1 V. With this cell setup we achieved a peak power density higher than 600 mW cm^{-2} (**Fig. S42**). We cycled the high concentration (26 Ah L^{-1}) cell, achieving a Coulombic efficiency of approximately 98%, limited by Br$_2$ crossover (**Fig. S43**). The crossover of Br$_2$ did not cause decomposition, precipitation, or cell failure (**Fig. S44**). We also confirmed that protons and hydroxide ions can be generated by discharging in the BPM sub-cell to initiate the pH difference. Polarization of charged electrolyte through the BPM sub-cell shows a voltage cost of about 1 V for acid-base generation at a current density of 40 mA cm^{-2} (**Fig. S45**). A comparison between two-membrane pH-decoupling ARFB and single-membrane pH decoupling ARFB is provided in **Fig. 6**, with recommended operating conditions. pH recovery can also be utilized in other systems that involve pH instability, such as when caused by proton-coupled side reactions.[6,24]

Conclusion

We presented a mild pH-decoupling ARFB, operating with a negolyte pH of ~13 and a posolyte pH of ~3, suppressing acid-base crossover rates to less than 0.3 nmol s^{-1} cm^{-2}. This strategy permits an open-circuit voltage exceeding 1.7 V with unprecedentedly long lifetime and only minor energy cost and Coulombic efficiency penalty. Additionally, we developed a sub-cell using a bipolar membrane that can recover protons and hydroxide crossover without requiring exogenous addition of acid and base, thereby preventing the long-term salt accumulation problem. This work resolves the long-standing tradeoff between high voltage output and the energy cost penalty associated with acid-base crossover, by answering the question of "how bad acid-base crossover is in pH-decoupling systems and how to manage it". We also demonstrated that the concept of mild pH-decoupling and acid-base recovery can be utilized in other pH-decoupling, pH-sensitive, or pH-instable electrochemical applications. Future work on pH-decoupling batteries should not only pursue astonishingly high voltage output, but also pay more attention to the long-term practicability of the setup and the cost associated with maintaining the pH difference. Regarding the capital cost of energy storage, higher voltage output and lower resistance of the pH-decoupling setup can increase the acid-base crossover tolerance, which informs directions of developing next-generation aqueous redox-active molecules, low-resistance membranes with high selectivity and long-lifetime pH-decoupling ARFB systems. .

Materials and methods

Materials and Synthesis 4,4 ′ -bis(hydroxymethyl)-2,2 ′ -bipyridine (Bhmbpy), 3-[bis (2-hydroxyethyl) amino]-2-hydroxypropanesulfonic acid (DIPSO), 1,3-propylenediaminetetraacetate (PDTA), FeCl$_2$, FeCl$_3$ were purchased from VWR International. 4,4'-[(9,10-Dioxo-9,10-dihydroanthracene-2,6-diyl)bis(oxy)]dibutyric acid (2,6-DBEAQ) was purchased directly from TCI Chemicals. Cr(II)-(1,3-propylenediaminetetraacetate) potassium salt (CrPDTA) was provided by Marshak group from University of Colorado Boulder. 3,4-diaminobenzoic acid, 2-hydroxy-naphthquinone, potassium ferricyanide and potassium ferrocyanide were purchased from Sigma-Aldrich. Fumasep® E-620K and Nafion® 117 as cation exchange membrane, Selemion® DSV-N anion exchange membrane and Fumasep® bipolar membrane were purchased and only soaked in 1M NaCl or KCl solution before usage.

16

Supercapacitor electrodes were fabricated as follows: High surface area porous carbon powder (purchased from ACS Materials), polyvinylidene fluoride (PVDF) (as a binder, dissolved in N-methyl-2pyrrolidone (NMP) with 1:40 PVDF/NMP weight ratio), and SuperP carbon black were combined in a slurry with the following weight ratios: 85:10:5 to create the capacitive electrodes. The slurry was cast on baked carbon papers (SGL39AA) (400 °C overnight) before it was dried overnight at 70°C. The electrodes were then used directly for the crossover tests in a standard flow cell.

Electrodes for cell cycling tests are carbon papers (SGL 39AA) baked at 400 °C overnight. Center chambers for three-chamber cells were made by PDMS molding or 3-D printing (see Supporting information: Three-chamber two-membrane cell setup characterization and optimization). The center chamber thickness varies from 0.2 mm to centimeters. Several porous plastic spacers were put in the center chamber window to physically avoid AEM CEM touching each other. For this paper, we were using a 3-D printed center chamber with curved in membrane to achieve even flow with 0.2 mm thickness for cell cycling tests, if not further specified.

For BHPC synthesis, 10 mmol of 3,4-diaminobenzoic acid in 100 mL glacial acetic acid, with 10 mmol 2-hydroxy-naphthquinone slowly added was stirred for 12 h at 50 °C. BHPC was obtained with yield > 90% after pouring the mixture into cold water and washed. BHPC electrolyte was prepared by dissolving a certain concentration of BHPC in 1 M NaCl, with NaOH adjusting the pH to 13.

$Fe(Bhmbpy)_3$ electrolyte was prepared by dissolving $FeCl_2$ and Bhmbpy with a ratio of 1:3.5 in 1 M NaCl, using HCl adjusting pH to 3, if not claimed otherwise. $FeCl_2$ electrolyte was prepared by dissolving 2 M $FeCl_2$ in water, with NaCl and HCl adjusting the whole ion concentration and initial pH to 2.

Fe(DIPSO) electrolyte was prepared by dissolving $FeCl_3$ and DIPSO with a ratio of 1:1.5, with NaCl and NaOH adjusting the whole ion concentration (total anion equaling 1.3 M) and initial pH to 13. The electrolyte was filtered before usage. DBEAQ electrolyte was prepared by dissolving 0.1 M DBEAQ in 1 M KCl, with KOH adjusting the pH to 12. When using DBEAQ, 1.3 M KCl was used instead of NaCl in the center chamber when running the three-chamber cell.

CrPDTA electrolyte was prepared by dissolving 1 M CrPDTA (potassium salt) in water, then adding 0.1 M PDTA as buffer reagent, and adjusting pH to 9 using KOH.

Hydroxide (or proton) crossover rate across CEM (or AEM) was evaluated in a standard 5 cm^2 flow cell with two chambers (receiving and source chambers). The receiver chamber contains 1 M NaCl, and its initial pH was set at 7. The source chamber contains 1 M NaCl, and its pH was varied by NaOH (or HCl) for each crossover test (1 M NaOH for pH 14 and 1 M HCl for pH 0, without NaCl). Each cell was built with two layers of high surface area porous carbon coated supercapacitor electrodes in the anode and the cathode that are separated by an ion exchange membrane (DSV-N for proton crossover test and E620 for hydroxide crossover test). The membrane was soaked in 1 M NaCl overnight before use. During each crossover test, alternating constant current was applied with a restricted cell voltage of 1.1 V to avoid water splitting. During alternating current cycling, the pH of both the source and receiving chambers were tracked by pH sensors in real-time.

Cyclic voltammetry was recorded by an electrochemical analyzer from CH instruments CHI 608E with a three-electrode system including one glassy carbon working electrode, one platinum counter

17

electrode and one Ag/AgCl reference electrode. The glassy carbon working electrode was polished with an aluminum slurry before and after each scan.

Rotating disk electrode (RDE) tests were performed using a Pine Instruments Modulated Speed Rotator AFMSRCE equipped with a 5 mm diameter glassy carbon working electrode (Pine Instruments E5PK), an Ag/AgCl reference electrode in 3 M KCl solution (CHI), a graphite counter electrode and a Gamry Reference 3000 potentiostat.

Three-chamber two-membrane cell cycling was conducted in a 5 cm^2 flow battery, using 10 mL 0.1 M Fe(Bhmbpy)$_3$ as capacity limiting side, pairing with 20 mL 0.1 M negolyte, if not clarified. Electrolytes were pumped using a flow rate of 60 mL/min through 3 layers of based carbon papers as electrodes. Center chamber is separated by one E620 and one DSV-N. 20 mL 1.3 M NaCl was cycled as center chamber electrolyte. Center solution was pumped using 10 mL/min. Three pH sensors were inserted in posolyte, negolyte and center solution, respectively. pH reading out was collected by an Arduino during cell operation and manually calibrated after. The cell was operated with a constant current (20 mA cm^{-2}) followed by constant potentials of 2 V (charging) and 0.7 V (discharging). During charging, the potential was held until the current density dropped lower than 1 mA cm^{-2}. During discharge, the current density cutoff was 0.2 mA cm^{-2} to ensure full discharge of the iron complex and its dimers. During operation, we would manually add 0.1 mL 1 M HCl and NaOH to compensate the acid-base crossover when the posolyte pH reaches 5. Or in pH recovery experiments, we would conduct BPM sub-cell pH recovery.

BPM sub-cell pH recovery was conducted in a 2.5 cm^2 flow battery with a BPM sandwiched in 2 layers of baked SGL-AA carbon paper. The sub-cell electrolyte inlets and outlets shared the electrolyte tank of the three-chamber cell. The sub-cell was connected to an independent potentiostat. During recovery, the cell cycling of the three-chamber cell was paused. Then we opened the valve and started the pump connecting sub-cell, with partially charged electrolytes (> 50% SOC) pumped through. Electrolytes are discharged in sub-cell using a constant current of 40 mA cm^{-2} for 3 – 4 minutes to recover the pH gradient loss. Afterwards, electrolytes were pumped out of the sub-cell, with valve closed and three-chamber cell normal cycling restarted. BPM polarization of certain pairs of electrolytes were evaluated by LSV with a sweeping rate of 3 mV s^{-1}, scanning from a voltage close to OCV to lower voltage.

Single-membrane pH-decoupling cell cycling was conducted in a 5 cm^2 flow battery, using 5 mL 1 M CrPDTA as capacity limiting side, pairing with 10 mL 1 M KBr. 3 layers of baked carbon papers were separated by one Nafion 212. Electrolytes were pumped using a flow rate of 60 mL/min. Two pH sensors were inserted in posolyte and negolyte, respectively. pH reading out was collected by an Arduino during cell operation and manually calibrated after. The cell was operated with a constant current (50 mA cm^{-2}) followed by constant potentials of 2.4 V (charging) and 1.4 V (discharging). The potential was held until the current density dropped lower than 20 mA cm^{-2}. We conducted BPM sub-cell acid-base generation before the starting of cell cycling. The pH in CrPDTA should be between 9 and 10, while KBr should be lower than 7 to ensure the normal cycling.

Cell polarization was conducted for Fe(Bhmbpy)$_3$ – BHPC and Fe(Bhmbpy)$_3$ – DBEAQ cells.

For the Fe(Bhmbpy)$_3$ – BHPC test, a cell composed of ~ 4.0 mL 0.1 M Fe(Bhmbpy)$_3$ (10.7 mAh theoretical capacity) in 1 M NaCl at pH 3 (HCl was added to adjust pH) paired with 5 mL of 0.1 M BHPC (26.8 mAh theoretical capacity) in 1 M NaCl at pH 13 (NaOH was added to adjust pH). The middle chamber was circulated with 2 M NaCl solution sandwiched by E620 as CEM and

18

DSV-N as AEM. 3 layers of carbon papers (SGL 39AA) baked at 400 °C overnight were used in each half-cell. For the Fe(Bhmbpy)$_3$ – DBEAQ cell, conditions were similar but supporting electrolytes were changed into KCl.

The full accessed capacity of the cell was first determined by performing a full charge/discharge cycling, which was accomplished by applying a 20 mA cm^{-2} constant current followed by potential holds at 2 V (charge) and 0.7 V (discharge) until the current decreased to the cutoff value. The cell was then charged with intervals to various states of charge (calculated from the percentage of the total accessed capacity). To determine the high-frequency area-specific resistance (ASR), electrochemical impedance spectroscopy (EIS) measurements were conducted at each SOC with a perturbation of 10 mV and frequencies ranging from 1 to 100,000 Hz. The battery's open-circuit voltage (OCV) was also measured. Additionally, the potential was swept at each SOC at a scan rate of 150 mV s^{-1}, and the current response as a result was measured to create polarization curves. The polarization ASR was computed using the linear region of the polarization curves near OCV.

For galvanostatic tests, constant current densities between 10 to 60 mA cm^{-2} with intervals of 10 mA cm^{-2} were applied during both charge and discharge cycles with potential holds during discharge. Cut-off values of 2.2 V and 0.7 V were used. Consequently, the Coulombic, capacity utilization and energy efficiencies are calculated for each current density.

Supporting Information

Supporting Information is available from the online library or from the author.

Author Contributions

D.X. and A.M.A. designed and conducted cell tests and electrochemical experiments. D.X. developed the concept of mild pH-decoupling ARFB and acid-base recovery. A.M.A. worked on molecule synthesis and characterization. D.X. and J.G. worked on the posolyte. D.X. and T.C. worked on the design of center chambers. A.M.A., L.C.I.F., T.Y.G and T.W. worked on crossover characterization. D.X. and Y.Z. worked on the single-membrane pH-decoupling cell. R.Y.L. and R.G.G. supervised the molecular synthesis and characterization. M.J.A. supervised the cell assembly, electrolyte composition selection, and performance evaluation. D.X. did the technoeconomic calculation. D.X., A.M.A. and M.J.A. drafted the manuscript. All authors edited the manuscript.

19

Conflict of Interest

The authors declare no conflict of interest.

Keywords

energy storage, long lifetime, pH-decoupling, high voltage, redox flow batteries, recovery

Extended data figures

Fe(Bhmbpy)$_3$ – DBEAQ cell
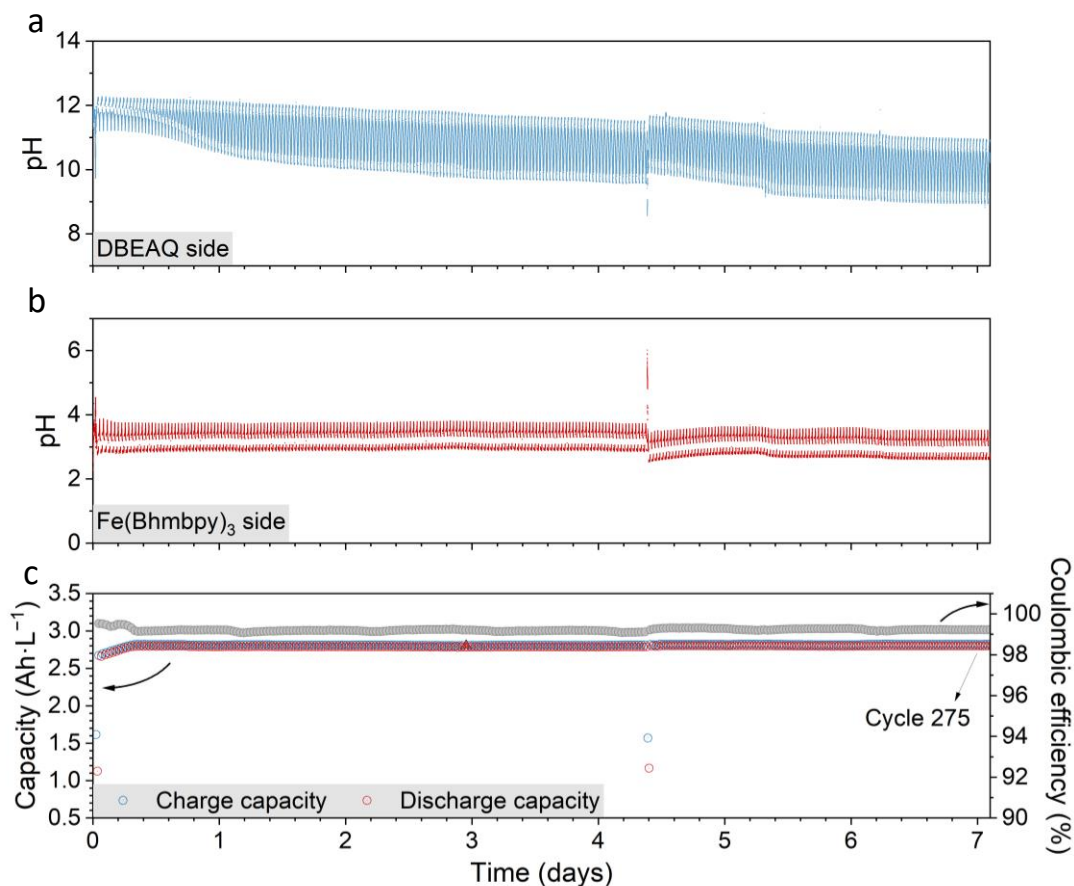
Extended Figure 1 | Fe(Bhmbpy)$_3$ – DBEAQ cell long-term cycling with pH recovery. a, In-situ monitoring of negolyte pH. **b,** In-situ monitoring of posolyte pH. **c,** Capacity and Coulombic efficiency during long-term cycling with pH recovery. Recovery was conducted on day 0 and day 4.4.

Fe(Bhmbpy)$_3$ – Fe(DIPSO) cell
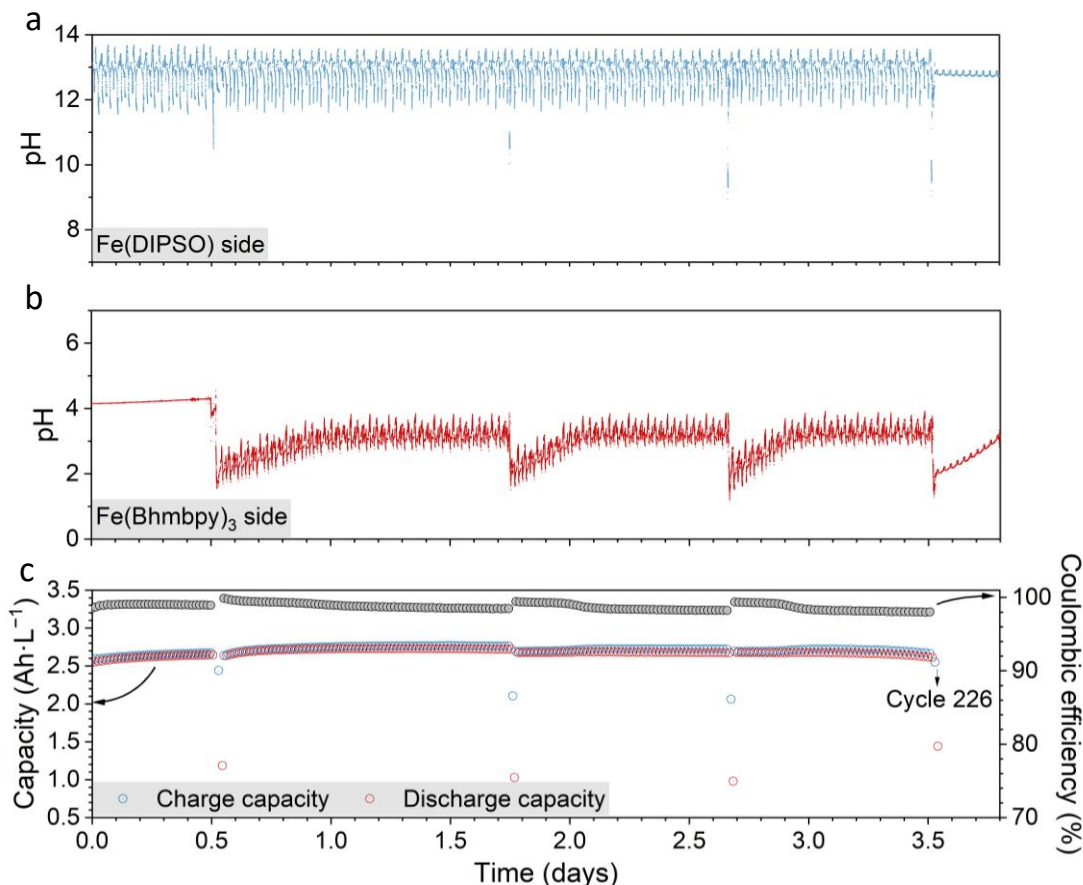
Extended Figure 2 | Fe(Bhmbpy)$_3$ – Fe(DIPSO) cell long-term cycling with pH recovery. a, In-situ monitoring of negolyte pH. **b,** In-situ monitoring of posolyte pH. **c,** Capacity and Coulombic efficiency during long-term cycling with pH recovery. Recovery for this all-iron ARFB was conducted on day 0.5, day 1.75, day 2.7 and day 3.5.

1   Dunn, B., Kamath, H. & Tarascon, J.-M. Electrical energy storage for the grid: a battery of choices. *Science* **334**, 928-935 (2011).
2   Liang, Y. & Yao, Y. Designing modern aqueous batteries. *Nat. Rev. Mater.* **8**, 109-122, doi:10.1038/s41578-022-00511-3 (2022).
3   Park, M., Ryu, J., Wang, W. & Cho, J. Material design and engineering of next-generation flow-battery technologies. *Nat. Rev. Mater.* **2**, doi:10.1038/natrevmats.2016.80 (2016).
4   Zhang, L., Feng, R., Wang, W. & Yu, G. Emerging chemistries and molecular designs for flow batteries. *Nat. Rev. Chem.* **6**, 524-543, doi:10.1038/s41570-022-00394-6 (2022).
5   Chao, D. & Qiao, S.-Z. Toward High-Voltage Aqueous Batteries: Super- or Low-Concentrated Electrolyte? *Joule* **4**, 1846-1851, doi:10.1016/j.joule.2020.07.023 (2020).

6   Robb, B. H., Farrell, J. M. & Marshak, M. P. Chelated Chromium Electrolyte Enabling High-Voltage Aqueous Flow Batteries. *Joule* **3**, 2503-2512, doi:10.1016/j.joule.2019.07.002 (2019).

7   Yao, Y., Lei, J., Shi, Y., Ai, F. & Lu, Y.-C. Assessment methods and performance metrics for redox flow batteries. *Nat. Energy* **6**, 582-588, doi:10.1038/s41560-020-00772-8 (2021).

8   Leung, P. K., Ponce-de-León, C., Low, C. T. J., Shah, A. A. & Walsh, F. C. Characterization of a zinc–cerium flow battery. *J. Power Sources* **196**, 5174-5185, doi:10.1016/j.jpowsour.2011.01.095 (2011).

9   Walsh, F. C. *et al.* The Development of Zn-Ce Hybrid Redox Flow Batteries for Energy Storage and Their Continuing Challenges. *ChemPlusChem* **80**, 288-311, doi:10.1002/cplu.201402103 (2015).

10   Perry, M. L., Rodby, K. E. & Brushett, F. R. Untapped Potential: The Need and Opportunity for High-Voltage Aqueous Redox Flow Batteries. *ACS Energy Lett.* **7**, 659-667, doi:10.1021/acsenergylett.1c02225 (2022).

11   Yan, Z. *et al.* High-Voltage Aqueous Redox Flow Batteries Enabled by Catalyzed Water Dissociation and Acid-Base Neutralization in Bipolar Membranes. *ACS Cent Sci* **7**, 1028-1035, doi:10.1021/acscentsci.1c00217 (2021).

12   Weng, G.-M., Li, C.-Y. V. & Chan, K.-Y. High-voltage pH differential vanadium-hydrogen flow battery. *Materials Today Energy* **10**, 126-131, doi:10.1016/j.mtener.2018.08.014 (2018).

13   Gu, S., Gong, K., Yan, E. Z. & Yan, Y. A multiple ion-exchange membrane design for redox flow batteries. *Energy Environ. Sci.* **7**, 2986-2998, doi:10.1039/c4ee00165f (2014).

14   Gong, K. *et al.* A zinc–iron redox-flow battery under $100 per kW h of system capital cost. *Energy Environ. Sci.* **8**, 2941-2945, doi:10.1039/c5ee02315g (2015).

15   Xie, X., Mushtaq, F., Wang, Q. & Daoud, W. A. The Renaissance of the Zn-Ce Flow Battery: Dual-Membrane Configuration Enables Unprecedentedly High Efficiency. *ACS Energy Lett.* **7**, 3484-3491, doi:10.1021/acsenergylett.2c01646 (2022).

16   Beh, E. S. *et al.* A Neutral pH Aqueous Organic–Organometallic Redox Flow Battery with Extremely High Capacity Retention. *ACS Energy Lett.* **2**, 639-644, doi:10.1021/acsenergylett.7b00019 (2017).

17   Zhong, C. *et al.* Decoupling electrolytes towards stable and high-energy rechargeable aqueous zinc–manganese dioxide batteries. *Nat. Energy* **5**, 440-449, doi:10.1038/s41560-020-0584-y (2020).

18   Xia, Y. *et al.* A cost-effective alkaline polysulfide-air redox flow battery enabled by a dual-membrane cell architecture. *Nat. Commun.* **13**, 2388 (2022).

19   Zhu, Y.-h. *et al.* Decoupled aqueous batteries using pH-decoupling electrolytes. *Nat. Rev. Chem.* **6**, 505-517, doi:10.1038/s41570-022-00397-3 (2022).

20   Kwabi, D. G., Ji, Y. & Aziz, M. J. Electrolyte Lifetime in Aqueous Organic Redox Flow Batteries: A Critical Review. *Chem. Rev.* **120**, 6467-6489, doi:10.1021/acs.chemrev.9b00599 (2020).

21   Wang, C. *et al.* Molecular Design of Fused-Ring Phenazine Derivatives for Long-Cycling Alkaline Redox Flow Batteries. *ACS Energy Lett.* **5**, 411-417, doi:10.1021/acsenergylett.9b02676 (2020).

22   Gao, J. *et al.* A High Potential, Low Capacity Fade Rate Iron Complex Posolyte for Aqueous Organic Flow Batteries. *Adv. Energy Mater.* **12**, doi:10.1002/aenm.202202444 (2022).

23   Park, M. *et al.* A High Voltage Aqueous Zinc–Organic Hybrid Flow Battery. *Adv. Energy Mater.* **9**, doi:10.1002/aenm.201900694 (2019).

23

24   Kong, T. *et al.* Stable Operation of Aqueous Organic Redox Flow Batteries in Air Atmosphere. *Angew. Chem. Int. Ed.* **62**, e202214819, doi:10.1002/anie.202214819 (2023).

25   Zhang, F. *et al.* Decoupled Redox Catalytic Hydrogen Production with a Robust Electrolyte-Borne Electron and Proton Carrier. *J. Am. Chem. Soc.* **143**, 223-231, doi:10.1021/jacs.0c09510 (2021).

26   Hohenadel, A. *et al.* Electrochemical characterization of hydrocarbon bipolar membranes with varying junction morphology. *ACS Applied Energy Materials* **2**, 6817-6824 (2019).

27   Metlay, A. S. *et al.* Three-Chamber Design for Aqueous Acid–Base Redox Flow Batteries. *ACS Energy Lett.* **7**, 908-913, doi:10.1021/acsenergylett.2c00040 (2022).

28   Weng, G.-M., Li, C.-Y. V. & Chan, K.-Y. High voltage vanadium-metal hydride rechargeable semi-flow battery. *J. Electrochem. Soc.* **160**, A1384 (2013).

29   Darling, R. M. Techno-economic analyses of several redox flow batteries using levelized cost of energy storage. *Current Opinion in Chemical Engineering* **37**, 100855 (2022).

30   Kwabi, D. G. *et al.* Alkaline Quinone Flow Battery with Long Lifetime at pH 12. *Joule* **2**, 1894-1906, doi:10.1016/j.joule.2018.07.005 (2018).

31   Shin, M., Noh, C., Chung, Y. & Kwon, Y. All iron aqueous redox flow batteries using organometallic complexes consisting of iron and 3-[bis (2-hydroxyethyl)amino]-2-hydroxypropanesulfonic acid ligand and ferrocyanide as redox couple. *Chem. Eng. J.* **398**, doi:10.1016/j.cej.2020.125631 (2020).

32   Shin, M., Noh, C. & Kwon, Y. Stability enhancement for all‐iron aqueous redox flow battery using iron‐3‐[bis(2‐hydroxyethyl)amino]‐2‐hydroxypropanesulfonic acid complex and ferrocyanide as redox couple. *International Journal of Energy Research* **46**, 6866-6875, doi:10.1002/er.7535 (2021).

33   Jin, S. *et al.* A Water-Miscible Quinone Flow Battery with High Volumetric Capacity and Energy Density. *ACS Energy Lett.* **4**, 1342-1348, doi:10.1021/acsenergylett.9b00739 (2019).

34   Xi, J., Wu, Z., Qiu, X. & Chen, L. Nafion/SiO2 hybrid membrane for vanadium redox flow battery. *J. Power Sources* **166**, 531-536 (2007).

35   Tan, R. *et al.* Hydrophilic microporous membranes for selective ion separation and flow-battery energy storage. *Nat. Mater.* **19**, 195-202 (2020).

36   Xia, Y. *et al.* Polymeric membranes with aligned zeolite nanosheets for sustainable energy storage. *Nature Sustainability* **5**, 1080-1091 (2022).

37   Ye, C. *et al.* Development of efficient aqueous organic redox flow batteries using ion-sieving sulfonated polymer membranes. *Nat. Commun.* **13**, 3184 (2022).

38   Li, Z. & Lu, Y.-C. Polysulfide-based redox flow batteries with long life and low levelized cost enabled by charge-reinforced ion-selective membranes. *Nat. Energy* **6**, 517-528 (2021).

39   Lopez-Atalaya, M., Codina, G., Perez, J., Vazquez, J. & Aldaz, A. Optimization studies on a Fe/Cr redox flow battery. *J. Power Sources* **39**, 147-154 (1992).

40   Darling, R. M., Gallagher, K. G., Kowalski, J. A., Ha, S. & Brushett, F. R. Pathways to low-cost electrochemical energy storage: a comparison of aqueous and nonaqueous flow batteries. *Energy Environ. Sci.* **7**, 3459-3477 (2014).

41   Dmello, R., Milshtein, J. D., Brushett, F. R. & Smith, K. C. Cost-driven materials selection criteria for redox flow battery electrolytes. *J. Power Sources* **330**, 261-272 (2016).

42   Zuo, P. *et al.* Near-frictionless ion transport within triazine framework membranes. *Nature*, 1-7 (2023).

43   Lin, C. *et al.* High-voltage asymmetric metal–air batteries based on polymeric single-Zn2+-ion conductor. *Matter* **4**, 1287-1304, doi:10.1016/j.matt.2021.01.004 (2021).

Supporting Information

Mild pH-decoupling Aqueous Flow Battery with Practical pH Recovery

Dawei Xi[1,3], Abdulrahman M. Alfaraidi[1,3], Jinxu Gao[2], Thomas Cochard[1], Luana C. I. Faria[1], Zheng Yang[1], Thomas Y. George[1], Taobo Wang[1], Roy G. Gordon[1,2] *, Richard Y. Liu[2] *, Michael J. Aziz[1] *

1 John A. Paulson School of Engineering and Applied Sciences, Harvard University, Cambridge, MA, USA.

2 Department of Chemistry and Chemical Biology, Harvard University, Cambridge, MA, USA

3 These authors contributed equally: Dawei Xi and Abdulrahman M. Alfaraidi

* E-mail: gordon@chemistry.harvard.edu; richardliu@chemistry.harvard.edu; maziz@harvard.edu

Table of Contents

Supercapacitor driven ion crossover tests (Fig. S1)

We assembled a supercapacitor cell with one donor side solution with high concentration of acid or base and another side of initially neutral pH as acceptor. We monitored the pH of both sides. The source side pH did not have significant change after two days of applied current (state range of applied currents). Therefore, the crossover flux was calculated with the acceptor side pH change. pH value was converted into concentration, and then the concentration rate of change was normalized by the acceptor side solution volume (V) and the membrane area (A_{mem}).

$$[H^+] = 10^{-pH}$$

$$[OH^-] = 10^{pH-14}$$

$$Flux_{proton\ crossover} \approx \frac{d[H^+]}{dt} \frac{V}{A_{mem}}$$

$$Flux_{hydroxide\ crossover} \approx \frac{d[OH^-]}{dt} \frac{V}{A_{mem}}$$

The raw pH monitoring data of the acceptor side under a certain current density is shown in Fig. S1. Raw data was then fitted and converted to crossover flux.
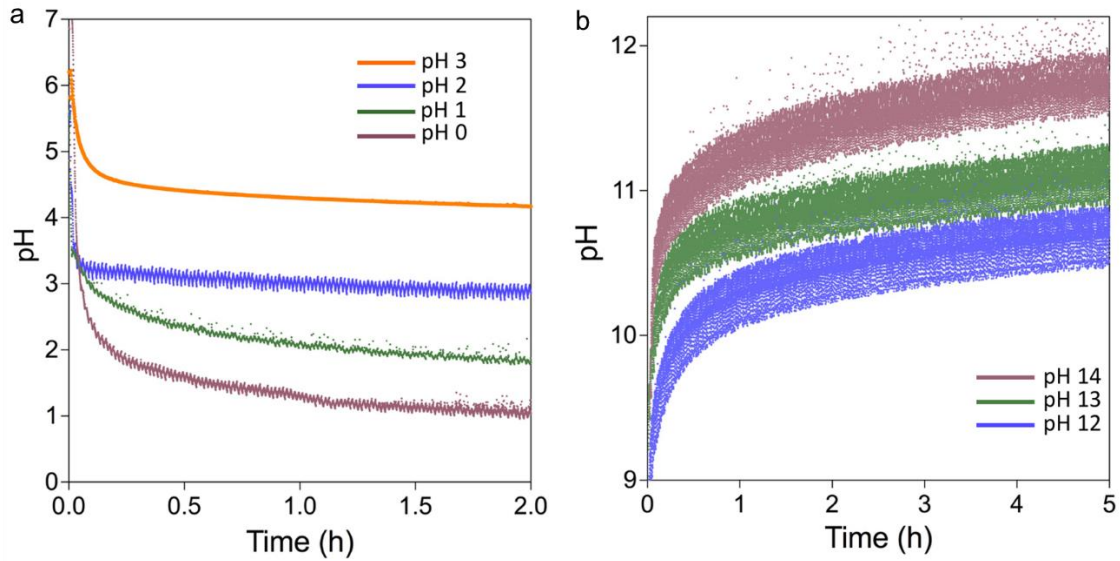
Figure S1 | In situ monitoring of pH change over time in the neutral (accepting) side of the cell with different initial pH of source side at 20 mA cm^{-2} for **a,** proton crossover test and **b,** hydroxide crossover test.

Tests and characterization of Fe(Bhmbpy)₃ and BHPC (Fig. S2-3)

Cyclic voltammetry of Fe(Bhmbpy)₃ shows no apparent difference under pH 2, 3 and 4, which is our operation pH range.
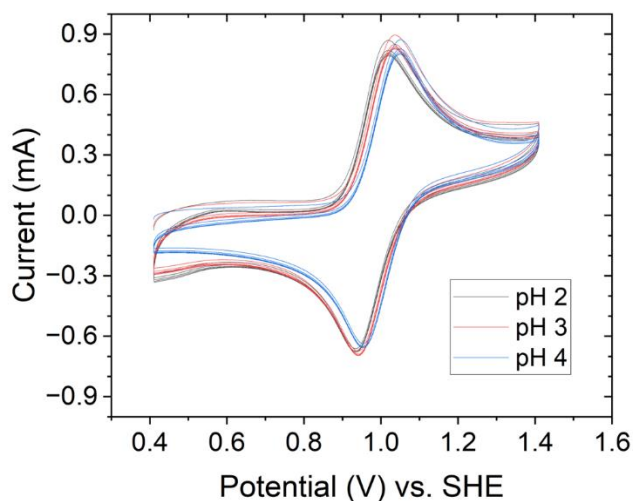
Figure S2 | Fe(Bhmbpy)₃ cyclic voltammetry in mild acidic conditions. Cyclic voltammogram of 10 mM Fe(Bhmbpy) in 1 m NaCl aqueous solution. pH was adjusted using HCl (scan rate 100 mV s^{-1}).
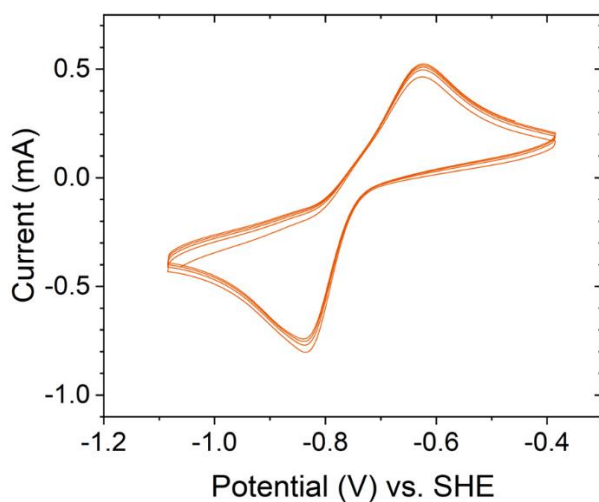
Figure S3 | BHPC cyclic voltammetry in mild basic conditions at pH 13. Cyclic voltammogram of 10 mM BHPC in 1 m NaCl aqueous solution. pH was adjusted to 13 by NaOH (scan rate 100 mV s^{-1}).

Fe(Bhmbpy)₃ cycling performance in three-chamber cells, and optimization of its operational condition (Fig. S4-10)

Lower bound of operation pH (Fig. S4-6)

Since the properties of Fe(Bhmbpy)$_3$ in two-chamber standard ARFB at near neutral starting conditions have been tested in a previous study,[1] here we evaluate the properties of Fe(Bhmbpy)$_3$ in a three-chamber two-membrane cell (5 cm^2 working area) with pH gradient with various initial conditions. The negolyte was composed of 0.1 M (50 mL) potassium ferricyanide/ferrocyanide (4:1 ferricyanide: ferrocyanide) at pH 13 (adjusted by NaOH) as non-capacity limiting side, with 1 M NaCl as supporting salt. A cation exchange membrane (CEM, Fumasep E620 K) was used to separate the negolyte from the center chamber. The center chamber contained 1.3 M NaCl that was circulated through the cell from a 50 mL tank. The posolyte was prepared by adding 0.35 M Bhmbpy into 0.1 M FeCl$_2$ while adjusting initial pH to 2 using HCl. An anion exchange membrane (AEM, Selemion DSV-N) was used to separate the posolyte side from the center chamber. The electrolyte flow rate for posolyte and negolyte was 30 mL min^{-1}. The center chamber electrolyte flow rate was about 10 mL min^{-1}. The cell was cycled with CCCV protocol at 20 mA cm^{-2} with voltage cut-off values of 0.9 V and -0.4 V during charge and discharge, respectively. The cutoff voltage was held until current density dropped lower than 1 mA cm^{-2} (charging) and 0.2 mA cm^{-2} (discharging). Discharging current cutoff is smaller to fully recover the dimerized iron complex. The discharging voltage has to be at least 0.7 V lower than cell OCV to realize 'deep discharge' of Fe(Bhmbpy)$_3$ to avoid accumulation of dimers.[1]

The capacity fading of this cell is shown in **Fig. S4**. With low pH operation (< 1), the cycling showed lower Coulombic efficiency and rapid capacity fading (Fig. S4a) and Fe(Bhmbpy)$_3$ crossover became severe (Fig. S4b). After cycling, the pH of Fe(Bhmbpy)$_3$ is still about 1, and center chamber salt solution became pink, indicating fast crossover.
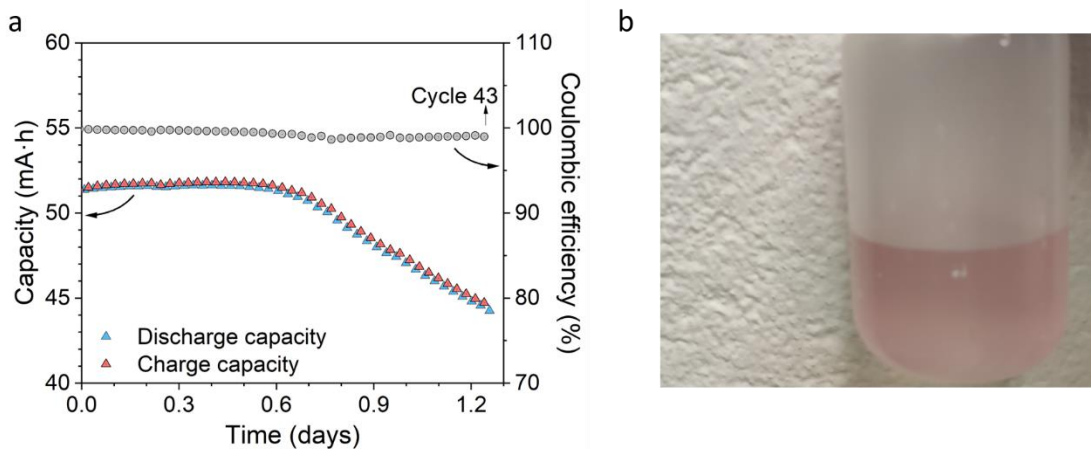
Figure S4 | Fe(Bhmbpy)₃ – Fe(CN)₆ three-chamber cell cycling with 1:3.5 of Fe:Bhmbpy and initial pH < 1. a, Capacity and Coulombic efficiency during cycling. **b,** Digital photo of center chamber salt solution (neutral pH) after cycling.

Crossover of Fe(Bhmbpy)$_3$ at different pH was further investigated by standard UV-Vis crossover tests (**Fig. S5**). A stirred H-cell was assembled with Selemion DSV-N (pre-soaked overnight in 1 M NaCl) clamped between 72 mM Fe(Bhmbpy)$_3$Cl$_2$ in 1 M NaCl (donating side, dark color) and

1.1 M NaCl (receiving side), both sides initially at pH 2.5, and the diffusion of the iron complex across the membrane was monitored with UV-vis spectrophotometry using a 1 cm length cuvette .[1] Over two days, the permeability of $Fe(Bhmbpy)_3^{2+}$ was determined to be $2 \times 10^{-11}\,cm^2/s$, similar to our previous report, and the receiving chamber became light pink in color (see digital photographs in a, days 1 and 2). Then, HCl was added dropwise to both sides of the H-cell to bring the pH to 1.0, and the pink color of the receiving chamber disappeared (digital photographs, days 3 and 4). From UV-vis of samples from the receiving chamber diluted 100x, a sharp absorbance peak was clear at 300 nm and grew over time between days 3 and 4 of the experiment, while the peak indicating the $Fe(Bhmbpy)_3^{2+}$ was no longer present. **Fig. S6** shows that the peak at 300 nm matches the shape of the peak for the Bhmbpy ligand (see spectra normalized to maximum absorbance), indicating that at low pH, Bhmbpy ligands are removed from the iron and can cross the membrane.
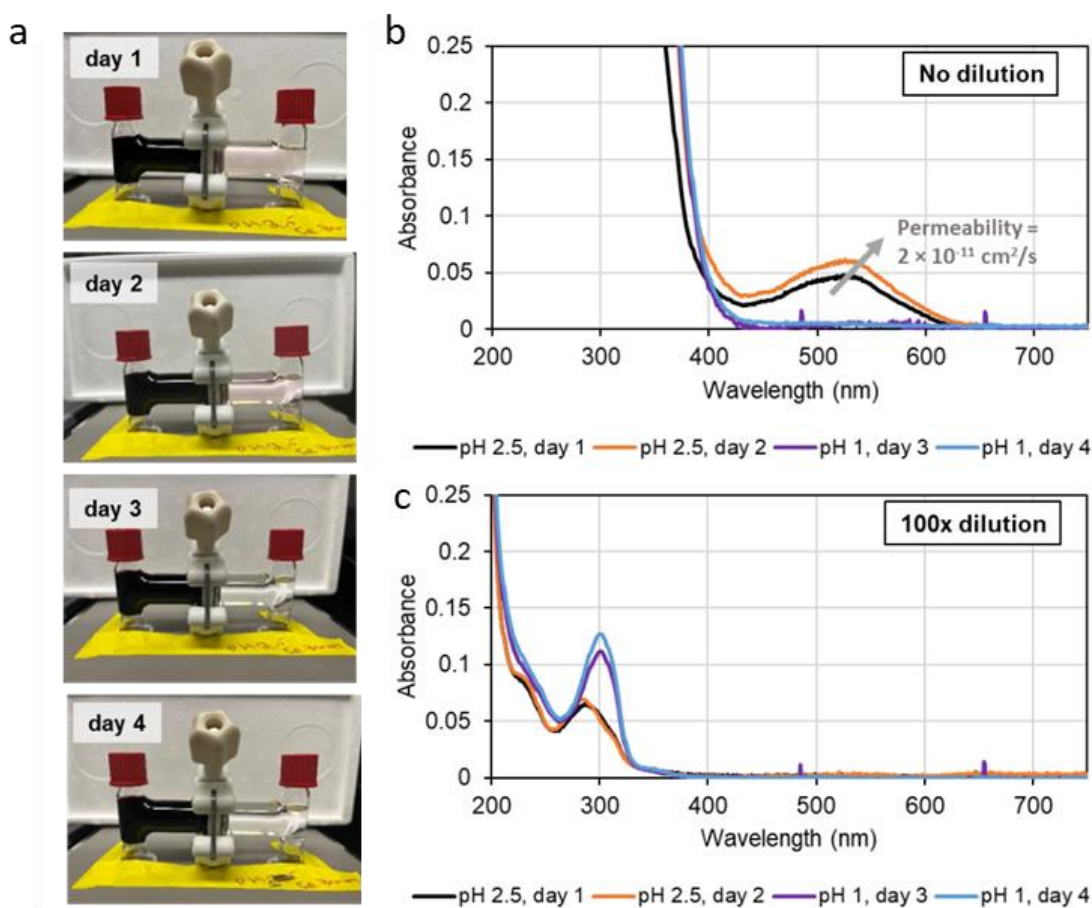
Figure S5 | Membrane (Selemion DSV-N) permeation of Fe(Bhmbpy)₃. a, A stirred H-cell setup for crossover test, with both sides initially at pH 2.5 for days 1 and 2. Then, HCl was added, bringing the pH to 1.0 for days 3 and 4. **b**, UV-vis of samples from the receiving chamber. **c**, UV-vis of one hundred times diluted samples from the receiving chamber.
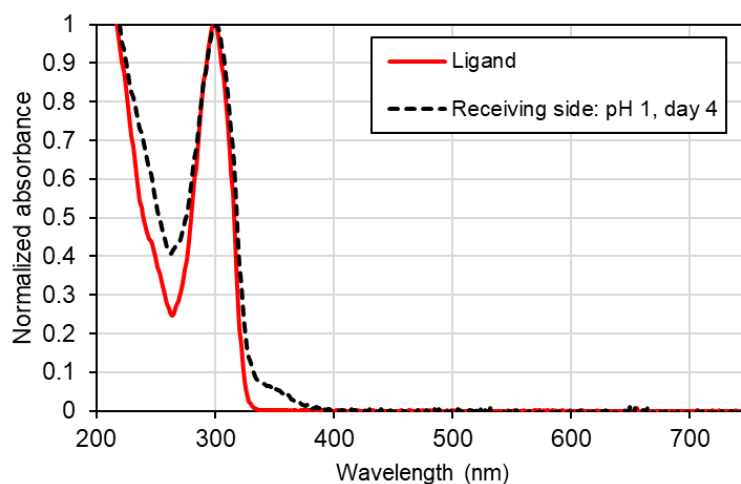
Figure S6 | UV-vis spectrum of receiving chamber at pH 1. The spectrum from crossed-over species matches the shape of the peak for the bare Bhmbpy ligand standard sample.

Results show that $Fe(Bhmbpy)_3$ will disassociate into iron ions and protonated ligands when pH reaches or lower than 1. This may explain the capacity fade shown in Fig. S4. Thus, for optimized operation, **the lower bound of the pH for $Fe(Bhmbpy)_3$ is 2.**

Upper bound of operation pH (Fig. S7-9)

Then we assessed the Fe(Bhmbpy)$_3$ cycling in three-chamber cells at higher initial pH to find the upper bound of operation pH. The cell setup and cycling conditions are the same as the lower bound test of operation pH. We prepared Fe(Bhmbpy)$_3$ by adding 0.3 M Bhmbpy into 0.1 M FeCl$_2$ without adjusting initial pH. The capacity fade of this cell is shown in **Fig. S7a**. The fast fading was caused by constant hydroxide crossover from ferricyanide side into Fe(Bhmbpy)$_3$ side. Hydroxide introduced unrecoverable dimerization of Fe(Bhmbpy)$_3$. Dimerized complex precipitation was found in the electrolyte after cycling. The dimerization reaction can be described as following:[1]

$$2Fe(Bhmbpy)_3{}^{3+} + H_2O + 2Cl^- \rightarrow Fe_2OCl_2(Bhmbpy)_4{}^{2+} + 2HBhmbpy^+$$
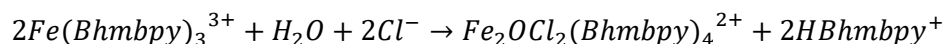
Or with hydroxide involved:

$$2Fe(Bhmbpy)_3{}^{3+} + 2OH^- + 2Cl^- \rightarrow Fe_2OCl_2(Bhmbpy)_4{}^{2+} + 2Bhmbpy + H_2O$$
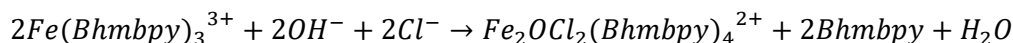
Therefore, with hydroxide crossover into posolyte, dimerized complex would accumulate and cannot be discharged. We added HCl solution to reverse the dimerization, as shown in **Fig. S7b**. Each time after adding acid, we achieve a few cycles of higher Coulombic efficiency, contributed by dimer discharging. The capacity will go back to initial value with just enough acid provided.
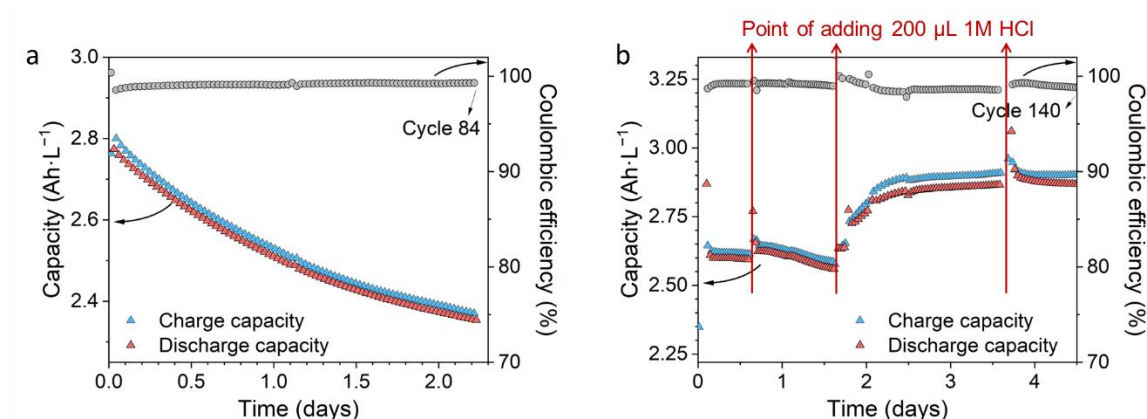
Figure S7 | Fe(Bhmbpy)$_3$ – Fe(CN)$_6$ three-chamber cell cycling with 1:3 of Fe:Bhmbpy and initial neutral pH. a, Capacity and Coulombic efficiency during cycling. **b,** After the test in (**a**), capacity and Coulombic efficiency during cycling with HCl added in Fe(Bhmbpy)$_3$, indicated by red arrows.

According to the pH measurement, any time when pH reached 4, any hydroxide crossing in the Fe complex chamber will cause dimerization. Precipitation formed is shown in **Fig. S8**. And this fading can always be recovered by adding acid. When pH for Fe(Bhmbpy)$_3$ side is higher than 2, the center chamber salt solution (neutral pH) can remain colorless, indicating slow crossover (**Fig. S9**). Thus, for optimized operation, **the upper bound of the pH for Fe(Bhmbpy)$_3$ is 4.**
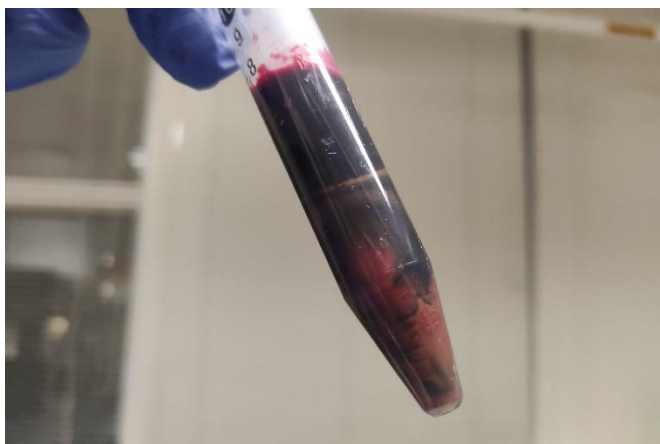
Figure S8 | Digital photo of dimerized Fe(Bhmbpy)₃ that precipitated and cannot be deep-discharged when pH > 4.

Figure S9 | Digital photo of center chamber salt solution after cycling with Fe(Bhmbpy)₃ pH maintained higher than 2.

Extra ligands as pH buffer (Fig. S10)

A pH buffer may be used to achieve a more stable operation. Luckily, the ligand Bhmbpy itself is a weak base. Bhmbpy and its protonated form HBhmbpy are a buffer pair with pK_a around $2 - 4$. Therefore, we use a ligand ratio of 1:3.5 (Fe:Bhmbpy) for later tests. **Extra ligands function as buffer solution that can keep the solution pH stable in optimized region for longer time. The optimized operation pH for this iron complex is $2 - 4$.**

We prepared $Fe(Bhmbpy)_3$ by adding 0.35 M Bhmbpy into 0.1 M $FeCl_2$ without adjusting initial pH. The capacity fading is shown in **Fig. S10**. With extra ligands as pH buffer, we can obtain stable capacity for several days during cycling.
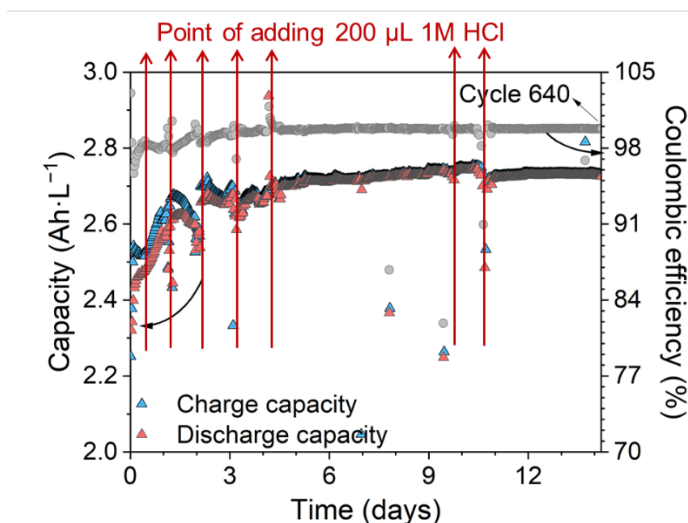
Figure S10 | $Fe(Bhmbpy)_3 - Fe(CN)_6$ three-chamber cell cycling with 1:3.5 of Fe:Bhmbpy starting neutral pH for all three chambers with acid added intermittently later.

Characterization and tests and of BHPC at pH 13 (Fig. S11)

a

b
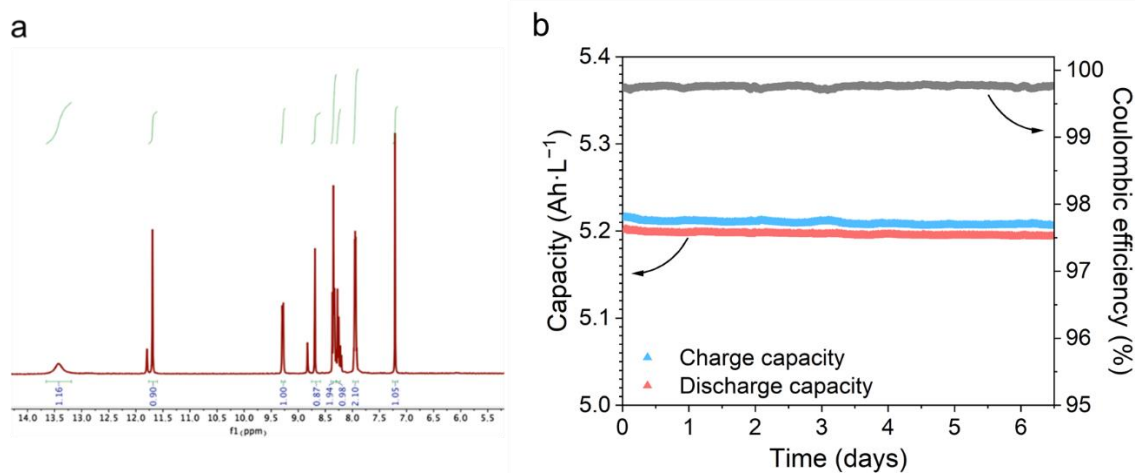
Figure S11 | a, ^{1}H NMR spectrum (400 MHz, DMSO-d6) of BHPC. b, Cycling stability of BHPC at pH 13. Long term cell cycling of standard flow batteries pH of 13 operated with a constant current (20 mA cm^{-2}) followed by constant potentials of 1.4 V (charging) and 0.6 V (discharging) at room temperature. The cell was assembled with 4.5 mL 0.1 M BHPC in 1 M NaCl paired with 50 mL of 0.1 M ferrocyanide/0.02 M ferricyanide in 1 M separated by an E620 K cation exchange membrane. The pH of both sides was adjusted to 13 by addition of NaOH. Fade rate is smaller than 0.02% per day.

Fade rate of BHPC under pH 14 is about 0.04%/day, as demonstrated by previous works[2]. Therefore, BHPC fade rate is smaller than iron complex (0.07% per day) through pH 13 to 14.

Fe(Bhmbpy)₃ – BHPC operation condition optimization (Fig. S12)

Mechanism of Coulombic efficiency imbalance in the cell and cell rebalancing

According to previous tests, BHPC has a Coulombic efficiency higher than 99.9%, while the Coulombic efficiency of Fe(Bhmbpy)$_3$ is around 99%. The Coulombic inefficiency of Fe(Bhmbpy)$_3$ in those case is attributed to the self-discharging of oxidized form. Specifically, ligands can be oxidized by charged Fe(Bhmbpy)$_3$:[1]

$$2Fe(Bhmbpy)_3^{3+} + HBhmbpy^+ + H_2O \rightarrow 2Fe(Bhmbpy)_3^{2+} + HOBhmbpy^+ + 2H^+$$
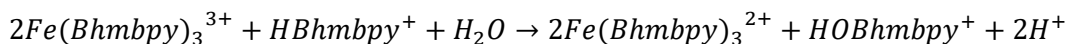
This self-discharging will over time make the cell out of balance with the posolyte accumulating reduced Fe(Bhmbpy)$_3$. To overcome this, we can expose the negolyte to air so that excess reduced BHPC is oxidized by oxygen. The oxidized BHPC may then be reduced at the negative electrode to oxidize the reduced posolyte species, rebalancing the cell. Similar strategies of rebalancing the cell were used in various reported research.[3, 4]

Fe(Bhmbpy)₃ – BHPC capacity balanced cell (Fig. S12)

To check the feasibility of this rebalancing strategy in our system, a capacity balanced cell was built by using 10 mL 0.1 M Fe(Bhmbpy)$_3$ (Fe:Bhmbpy = 1:3.5, initial pH 2) pairing with 5 mL 0.1 M BHPC in a three-chamber cell. The cell capacity fading was recovered by exposing BHPC side to air (**Fig. S12**). The oxygen-mediated oxidation of BHPC in the negolyte will result in net accumulation of hydroxide ions, which will not hurt the cell performance. The voltage-capacity curve shows the stable cycling voltage.
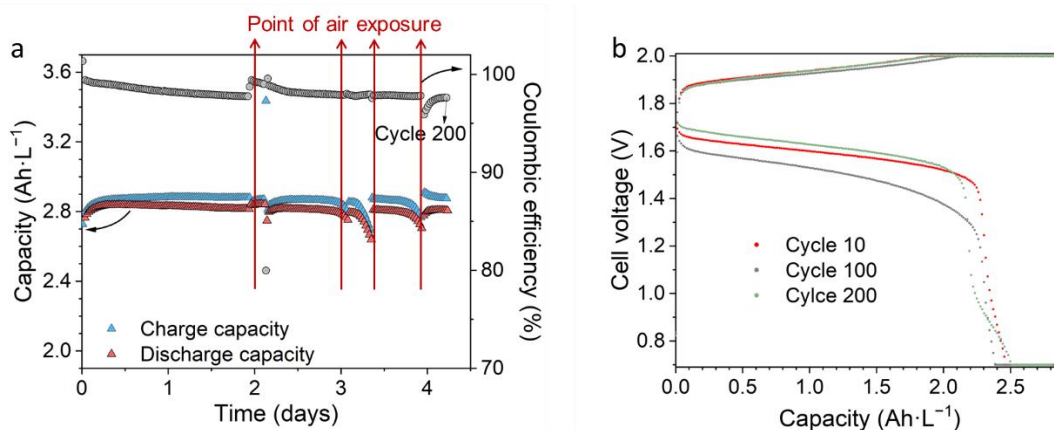
Figure S12 | Fe(Bhmbpy)₃ – BHPC three-chamber capacity balanced cell cycling with intermittent air exposure. a, Capacity and Coulombic efficiency during cycling. **b,** Cell voltage versus capacity for selected cycles.

Therefore, during the cell cycling in our case, air exposure was applied if the cell went out of balance.

Bipolar membrane (BPM) acid-base regeneration study (Fig. S13-15)

Polarization of BPM in a standard 4-electrode setup (Fig. S13)

We evaluated Fumasep FBM bipolar membrane polarization in a 4-electrode setup (**Fig. S13a**). 1 M NaCl solution, with added HCl or NaOH was used as electrolyte. Fresh electrolytes were pumped continually into the setup. Current was applied on WE and CE (Pt electrodes) for water splitting. Voltage was recorded between two RE (Ag/AgCl reference electrodes). Thus, the current and voltage drop across the membrane was collected. Linear sweeping voltammetry (LSV) was applied with a scan rate of 3 mV s^{-1} to collect the polarization curve. The BPM showed similar potential of the onset of water dissociation (~ 0.83 V) and current density at various pH couples (**Fig. S13b**). The small current before 0.8 V is mainly contributed by salt ions, rather than the generation of acid and base. Therefore, the BPM sub-cell can generate acid and base efficiently through near neutral to severe pH only when the current density is higher than approximately 20 mA cm^{-2}.
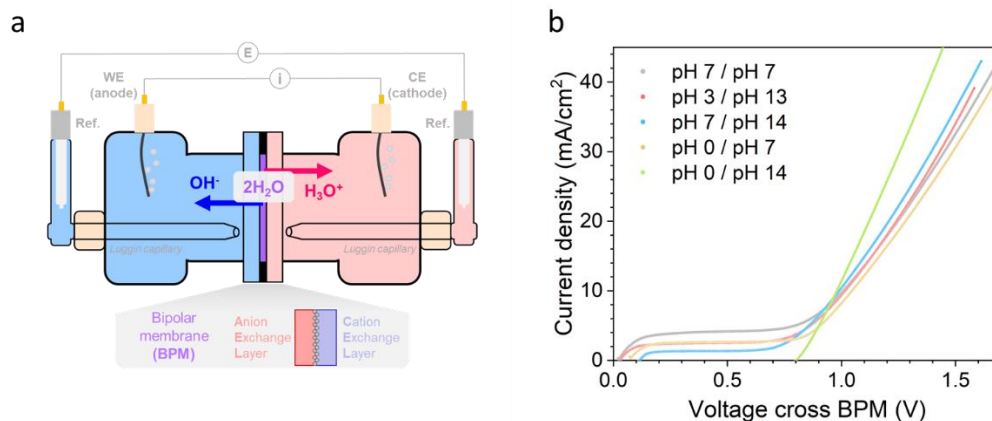
Figure S13 | BPM polarization test. a, 4-electrode setup for membrane polarization test.[5] **b,** Polarization curve of BPM using LSV.

BPM pH recovery mechanism

To explain the acid and base generation using BPM sub-cell, herein, we use subscript *(A)* indicating the posolyte acid chamber, *(B)* indicating the negolyte base chamber, and *(C)* indicating the center chamber. M stands for a posolyte molecule and Q stands for a negolyte molecule. When non proton coupled electron transfer (non-PCET) molecules are used as posolyte or negolyte:
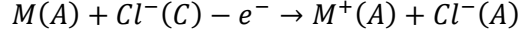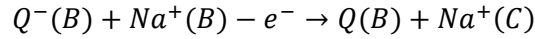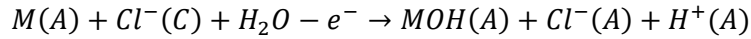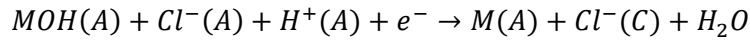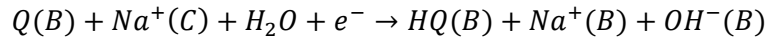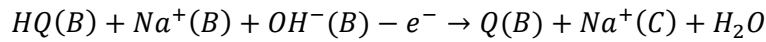
Charge of posolyte through AEM:

$$M(A) + Cl^-(C) - e^- \rightarrow M^+(A) + Cl^-(A)$$

Discharge of posolyte through AEM:

$$M^+(A) + Cl^-(A) + e^- \rightarrow M(A) + Cl^-(C)$$

Discharge of posolyte through BPM:

$$M^+(A) + Cl^-(A) + e^- + H^+(BPM) \rightarrow M(A) + Cl^-(A) + H^+(A)$$

Charge of negolyte through CEM:

$$Q(B) + Na^+(C) + e^- \rightarrow Q^-(B) + Na^+(B)$$

Discharge of negolyte through CEM:

$$Q^-(B) + Na^+(B) - e^- \rightarrow Q(B) + Na^+(C)$$

Discharge of negolyte through BPM:

$$Q^-(B) + Na^+(B) - e^- + OH^-(BPM) \rightarrow Q(B) + Na^+(B) + OH^-(B)$$
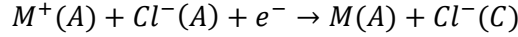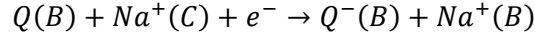
When proton coupled electron transfer (PCET) molecules are used as posolyte or negolyte:

Charge of posolyte through AEM:

$$M(A) + Cl^-(C) + H_2O - e^- \rightarrow MOH(A) + Cl^-(A) + H^+(A)$$

Discharge of posolyte through AEM:

$$MOH(A) + Cl^-(A) + H^+(A) + e^- \rightarrow M(A) + Cl^-(C) + H_2O$$

Discharge of posolyte through BPM:

$$MOH(A) + Cl^-(A) + e^- + H^+(BPM) \rightarrow M(A) + Cl^-(A) + H_2O$$

Charge of negolyte through CEM:

$$Q(B) + Na^+(C) + H_2O + e^- \rightarrow HQ(B) + Na^+(B) + OH^-(B)$$

Discharge of negolyte through CEM:

$$HQ(B) + Na^+(B) + OH^-(B) - e^- \rightarrow Q(B) + Na^+(C) + H_2O$$

Discharge of negolyte through BPM:

$$HQ(B) + Na^+(B) - e^- + OH^-(BPM) \rightarrow Q(B) + Na^+(B) + H_2O$$
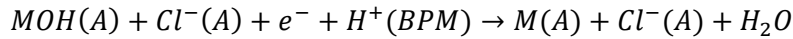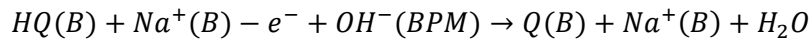
Energy efficiency penalty when using different pH pairs (Fig. S14)

Knowing the crossover rate of acid and base through membrane and the energy required for pH recovery, the energy efficiency was calculated when using different pH pairs. We used 3 Ω cm^2 as cell resistance, experimentally determined net crossover flux, and the theoretical energy cost (0.83 V) for BPM 1M acid-base recovery to calculate the round-trip energy efficiency. Mass transport, kinetic and other efficiency losses are not included in this calculation. Efficiency loss from resistance penalty is linear with current density. The non-linear portion of the curves in Figure S14 (at relatively low current density) are explained by acid-base crossover energy penalty. For example, pH 0 introduces severe proton crossover, with a large penalty to the energy efficiency (only 50 % efficiency at 10 mA cm^{-2}, Fig. S14a). At lower current density, more time will be spent on each cycle, increasing the amount of crossover (or, equivalent acid-base crossover current is a larger fraction of charge/discharge current) over the course of a given cycle. As an example of "equivalent acid-base crossover current ($I_{crossover}$)", 200 nmol cm^{-2} s^{-1} is equivalent to about 19.3 mA cm^{-2} ($200*10^{-9}*96485*1000$) crossover current density.

$$\text{Energy efficiency} = \frac{OCV - IR}{OCV + IR + \frac{I_{crossover}}{I} * 0.83}$$
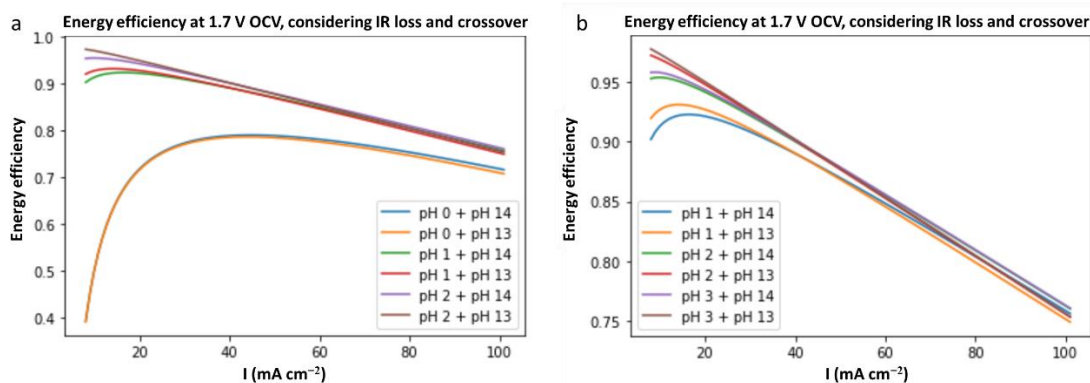
Figure S14 | Round-trip energy efficiency calculation considering pH crossover loss and IR loss with different operating pH pairs.

Voltage-capacity curve with recovery (Fig. S15)

Even after multiple uses of the BPM recovery cell, the three-chamber cell voltage – capacity curve remains stable (**Fig. S15**), indicating successful pH recovery through the BPM sub-cell.
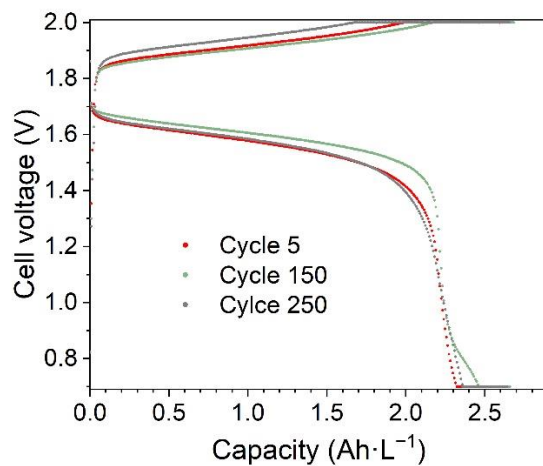

Figure S15 | Selected cell voltage – capacity curve of Fe(Bhmbpy)$_3$ – BHPC three-chamber cell with BPM sub-cell pH recovery.

Three-chamber two-membrane cell setup characterization and optimization (Fig. S16-25)

Cell resistance is an important factor affecting cell power output. For this section, the three-chamber two-membrane cell used Fe^{2+}/Fe^{3+} (negolyte) and $Fe(CN)_6^{4-}/ Fe(CN)_6^{3-}$ (posolyte) each at 0.1 M concentration, 50% SOC, with 1 M NaCl supporting salt. Tests were conducted in a 2.5 cm^2 cell. If not specified, the center chamber electrolyte was 1 M NaCl, tested at room temperature.

Effect of center chamber thickness (Fig. S16-19)

Center chambers for three-chamber cells in this work were prepared using polydimethylsiloxane (PDMS) molding (**Fig. S16**). An exploded view of the three-chamber cell including a PDMS center chamber is shown in **Fig. S17**. The center chamber thickness was adjusted to study the effect on cell resistance, as illustrated in **Fig. S18**.
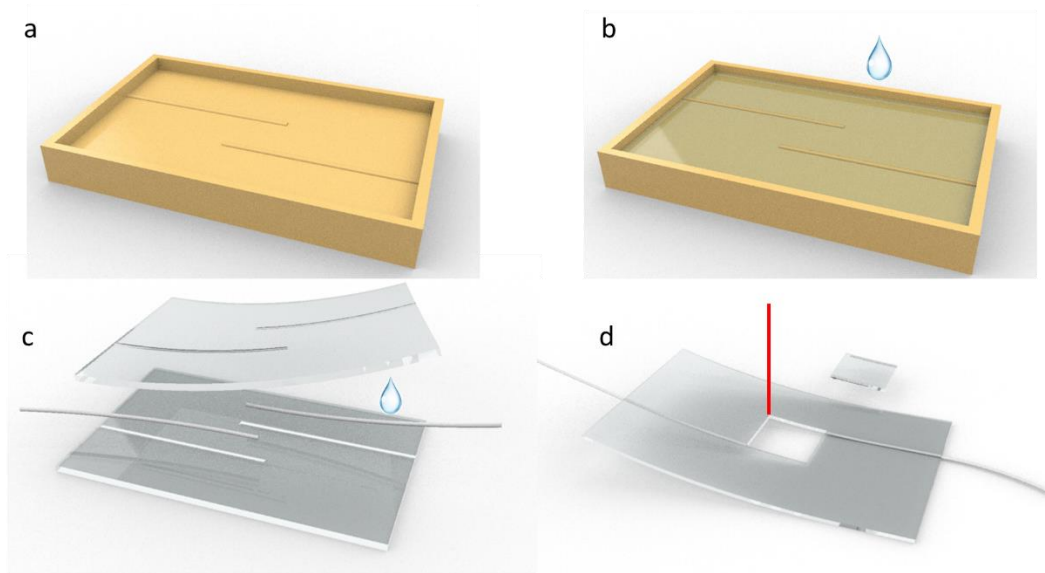
Figure S16 | Manufacturing of PDMS center chamber. a, 3-D printed plastic mold with shape for tubing insertion. **b,** Pouring PDMS into mold. The droplet represents liquid PMDS before curing. **c,** Using fresh PDMS (shown as the droplet in between) sealing two pieces together with tubing inserted. **d,** Laser cutting the window.
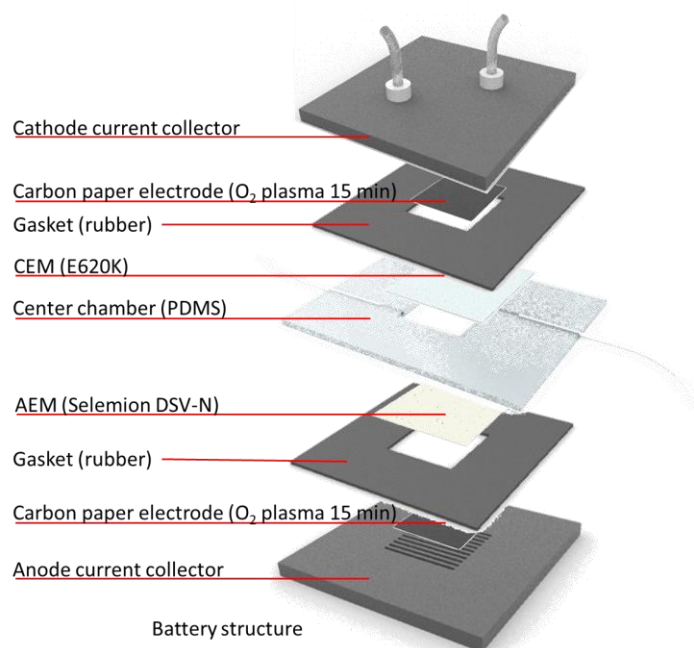
Figure S17 | Battery structure of 3-chamber cell with PDMS center chamber.
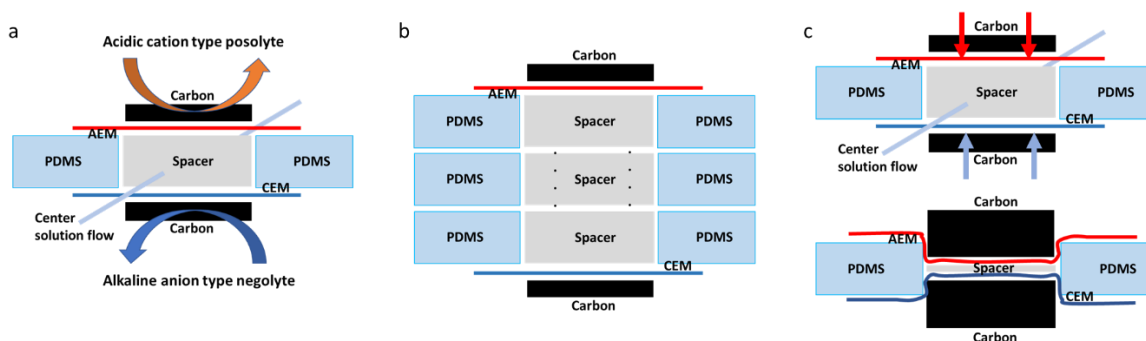

Figure S18 | Thickness adjustment of PDMS center chamber. a, cross-section of three-chamber cell with one center chamber. **b,** Multiple PMDS for thicker center chamber. **c,** From one center chamber to thinner center by curving in the membranes.

We measured the high frequency resistance of the cell using potentiostatic electrochemical impedance spectroscopy (PEIS) (**Fig. S19a**). PEIS measurements were conducted near OCV with a perturbation of 10 mV and frequencies ranging from 1 to 100,000 Hz. The x-intercept of the plot gives the high frequency resistance. LSV with a scan rate of 10 mV s^{-1} was applied near OCV to test the area specific resistance (ASR) from DC polarization of the cell (**Fig. S19b**). The slope of the polarization curve around OCV was calculated to approximate the resistance. The measured resistance values are shown in **Fig. S19c**. The cell resistance drops linearly as the center chamber is made to be thinner. The cell with the thinnest center chamber we were able to achieve (0.2 mm) gives the resistance close to the sum of AEM and CEM, meaning the resistance of the center chamber itself becomes negligible.
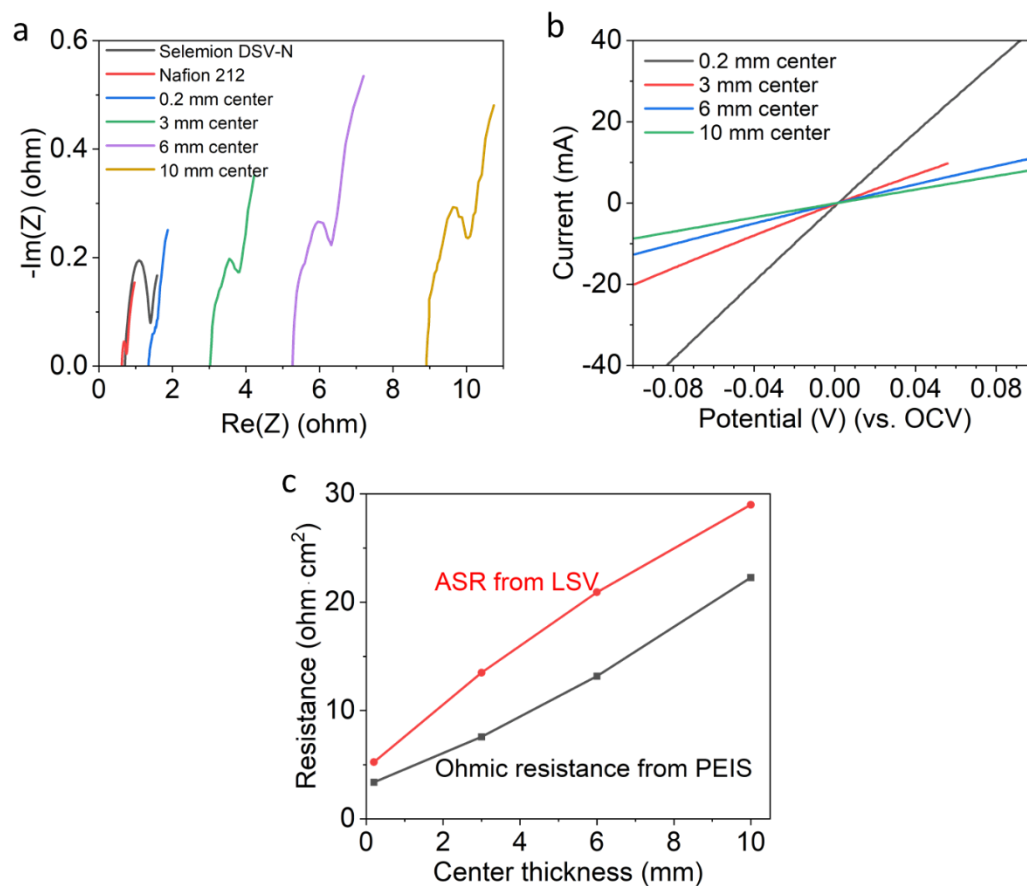
Figure S19 | Center chamber thickness effect. a, PEIS for different center thickness cells. **b,** Polarization curves for cells with different center chamber thicknesses. **c,** Resistance calculated from EIS and LSV.

Effect of center chamber solution concentration (Fig. S20)

We studied the effect of the concentration of NaCl in the center chamber electrolyte on cell resistance. We used a 3 mm center chamber, testing the system at room temperature.

The conductivity of NaCl was measured by a conductivity meter (Thermo Scientific STAR A212 Star A212 Conductivity Benchtop Meter) (**Fig. S20a**). The high frequency resistance of the three-chamber cell was measured with PEIS (**Fig. S20b**). Ohmic resistance of the cell (from PEIS) shows a nearly linear relationship versus center chamber ionic resistance. Because the membrane resistance can go up when using high concentration salt solution,[6] we chose 1 – 2 M NaCl as the center chamber electrolyte concentration for further tests.
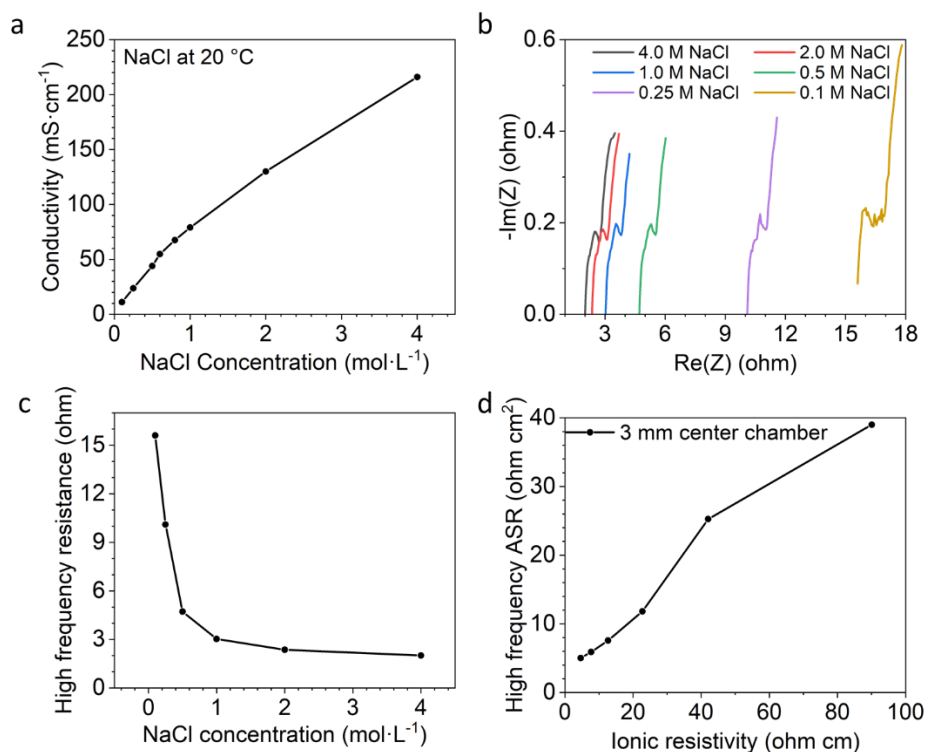
Figure S20 | Center chamber solution concentration effect. a, Conductivity of NaCl at various concentrations. **b,** PEIS spectra of the cell with various center chamber solution concentrations. **c,** Relationship of cell resistance and center chamber NaCl concentration. **d,** Relationship of cell area-specific resistance and center chamber electrolyte ionic resistance.

Effect of operation temperature (Fig. S21)

We used 1 M NaCl center chamber solution and evaluated the effect of operation temperature on cell resistance. Temperature can influence ion conductivity, but it is not a dominant factor when using thin center and high concentration solution (**Fig. S21**). At 50 °C, the conductivity of NaCl solution increases by 100% over the value at 25 °C. With a sufficiently thin center chamber and high concentration of center chamber solution, decreasing cell resistance by increasing temperature is not crucial.
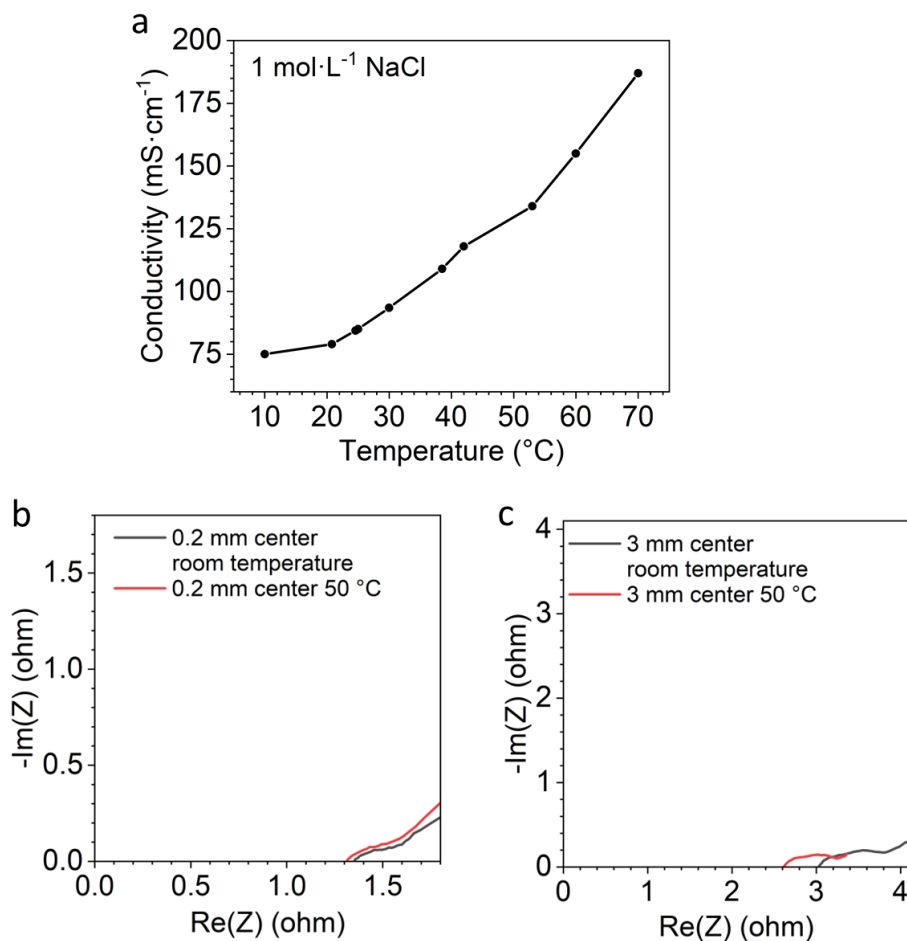
Figure S21 | Cell temperature effect. a, Temperature-dependent conductivity of 1 M NaCl. **b,** PEIS of the 2.5 cm^2 cell with 3 mm center chamber at different operation temperature. **c,** PEIS of the 2.5 cm^2 cell with 0.2 mm center chamber at different operation temperature.

Optimization of center flow (Fig. S22-24)

Resistance from concentration polarization may become important under high current density. This may be mitigated by introducing fast and uniform center chamber flow. However, flow through PDMS is slow and uneven (**Fig. S22**). We used 3-D printing to improve the center chamber, further reducing the resistance of the system during operation (**Fig. S23-24**).
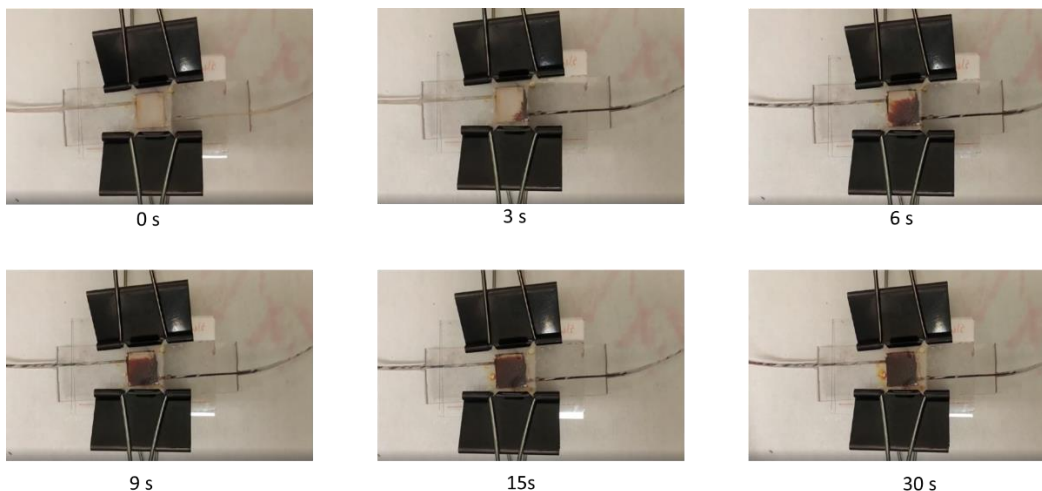

Figure S22 | Flow through PDMS center chamber. Dye was used to show the flow. Flow was slow through the center with uneven distribution, even using the maximum flow rate (10 mL/min) that the center chamber can hold.
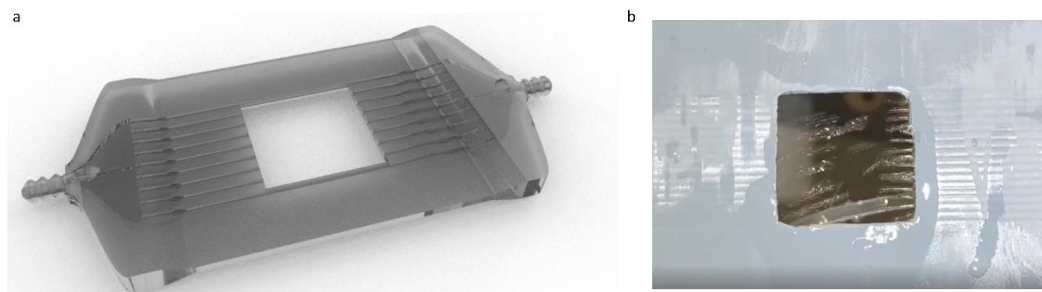
Figure S23 | 3-D printed center chamber. a, Structure of printed center chamber. We introduced multiple inlet and outlet channels. The thickness of this center chamber is 0.8 − 1.2 mm. **b,** A digital photo of the center chamber flow. The center chamber was vertically held. Water was pumped through the chamber from the right side, forming streams that flow out of the holes.
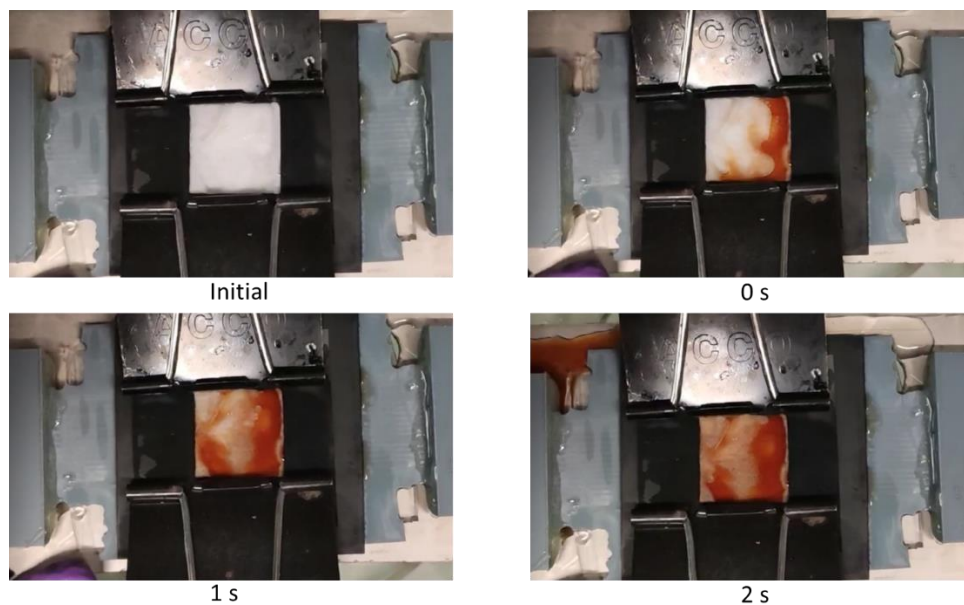
Figure S24 | Flow through 3-D printed center chamber. Dye was used to show the flow. Flow was fast (60 mL/min, without apparent pressure built up) through the center with even distribution.

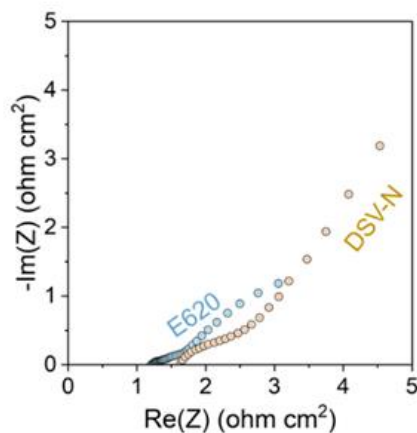## Resistance of the three-chamber cell after optimization (Fig. S25)

Figure S25 | Nyquist plot of E620 and DSV-N. High frequency ASR of E620 is about 1.2 ohm cm^2, and high frequency ASR of DSV-N is about 1.5 ohm cm^2. The high frequency ASR of the optimized three-chamber cell is about 2.7 – 3 ohm cm^2 as shown in Figure 5b, close to the total resistance of two individual membranes.

Voltage profile of the three-chamber cell at different current densities (Fig. S26)
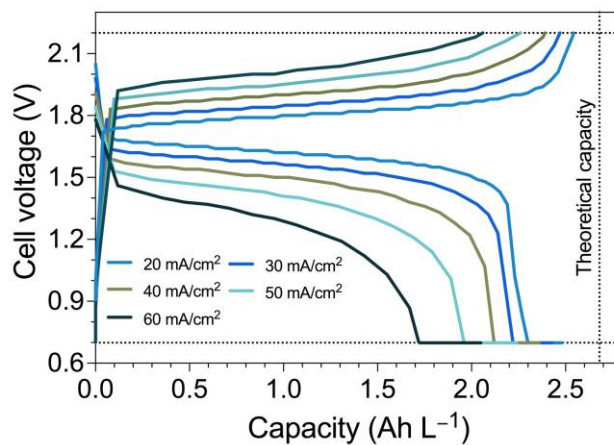

Figure S26 | Voltage profile of the three-chamber cell at different current densities.
Galvanostatic charge-discharge curves at various current densities with 2.2 V and 0.7 V cutoffs.
The theoretical capacity is indicated by the vertical dashed line.

Other redox pairs demonstrated in the system (Fig. S27-36)

Fe(Bhmbpy)₃ – DBEAQ cell (Fig. 27-31)

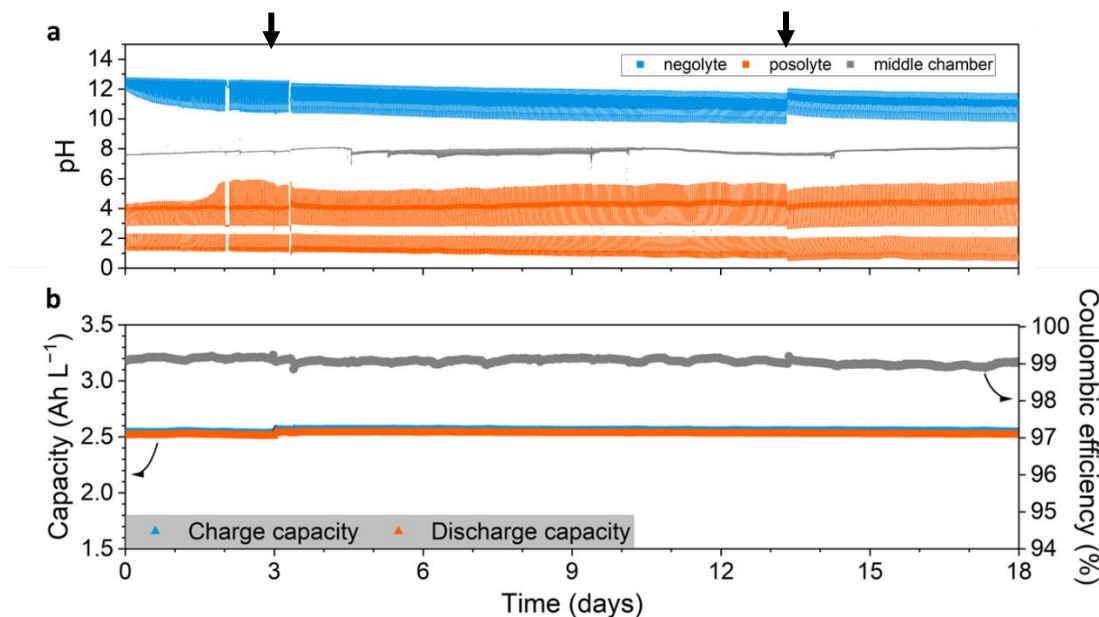Standard cycling of three-chamber ARFB with adding exogenous acid and base (Fig. 27-28)

Figure S27 | Fe(Bhmbpy)₃ – DBEAQ cell long-term cycling with adding exogenous acid and base. a, In-situ monitoring of negolyte, posolyte, and middle chamber pH. **b,** Capacity and Coulombic efficiency during long-term cycling. Acid (1 M HCl) and base (1 M NaOH) was added on day 3 and day 13.5 (indicated by the arrows).
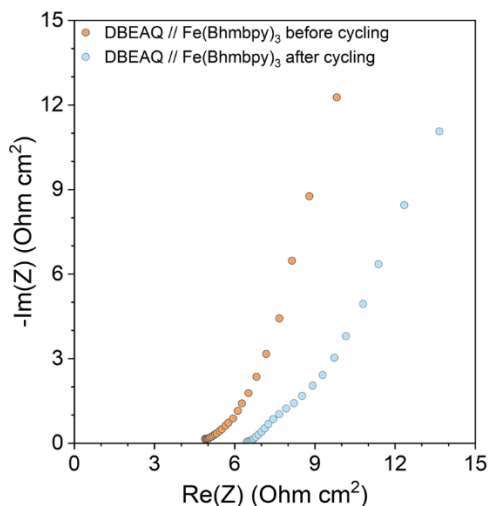

Figure S28 | PEIS of Fe(Bhmbpy)₃ – DBEAQ three-chamber cell with exogenous acid and base.

Cycling of three-chamber ARFB with BPM sub-cell in-situ pH recovery (Fig. S29-30)

The cell was also cycled with in-situ pH recovery. The BPM resistance and polarization was tested by PEIS and LSV, as shown in **Fig. S29**.
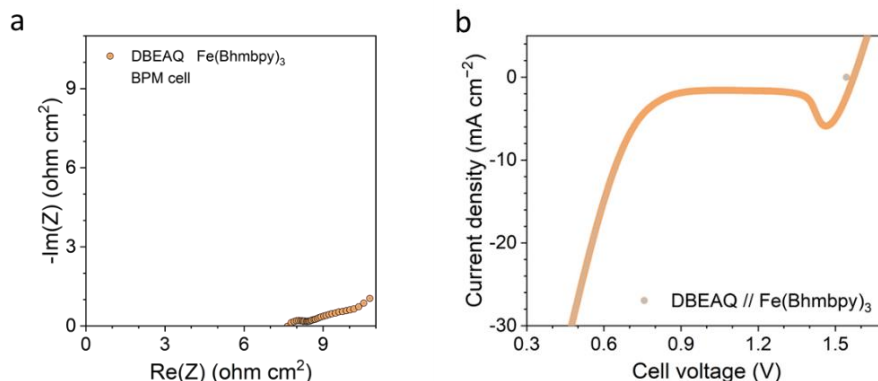

Figure S29 | Characterization of Fe(Bhmbpy)₃ – DBEAQ BPM sub-cell. a, PEIS of BPM sub-cell. **b,** Polarization LSV curve of BPM sub-cell.

The three-chamber cell resistance and selected cycles of cell voltage versus capacity showed well performance and stability of this three-chamber cell with in-situ recovery (**Fig. S30**).
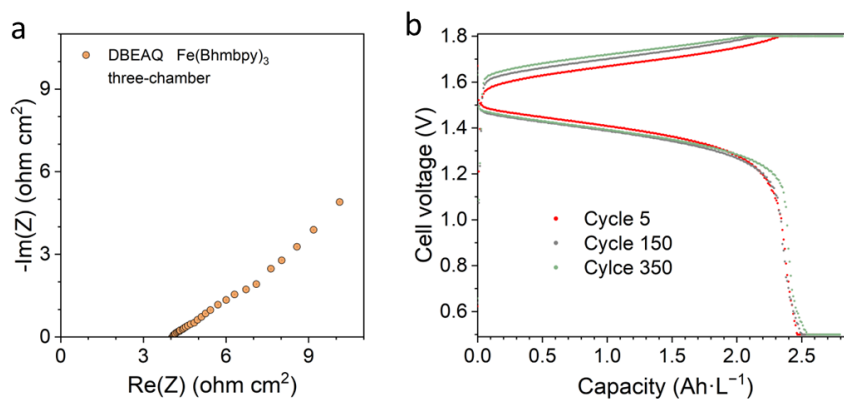

Figure S30 | Characterization of Fe(Bhmbpy)₃ – DBEAQ three-chamber cell with BPM sub-cell pH recovery. a, PEIS of the three-chamber cell. **b,** Selected voltage – capacity curve of the three-chamber cell with recovery.
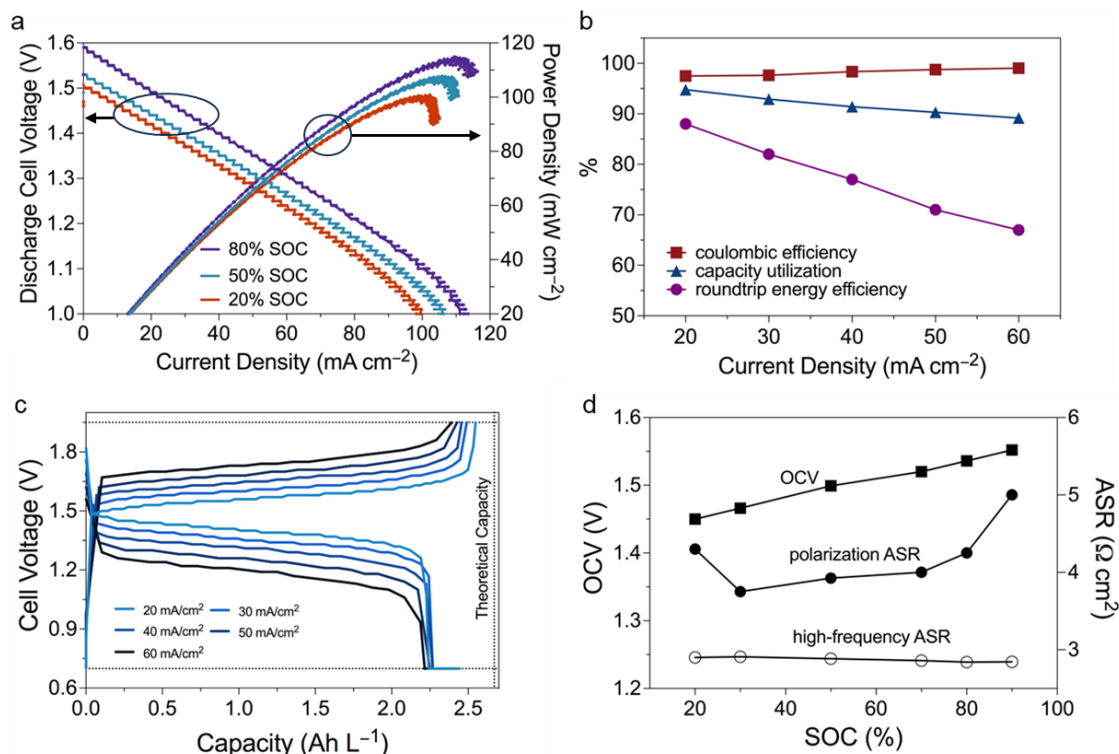
Polarization performance (Fig. S31)

Figure S31 | Polarization performance of the system, technoeconomic calculation, and comparison of pH-decoupling systems. a, Cell voltage and power density during discharge of three-chamber acid-base ARFB with 0.1 M DBEAQ and 0.1 M Fe(Bhmbpy)$_3$. The middle chamber was circulated with 2 M KCl solution and separated from the side chambers by E620 K as CEM and DSV-N as AEM. **b,** Plots of OCV and high frequency and polarization ASR vs. SOC for the same cell as in (**a**). **c,** Galvanostatic charge-discharge curves at various current densities with 1.95 V and 0.7 V cutoffs. The theoretical capacity is indicated by the vertical dashed line. **d,** Coulombic, capacity utilization, and energy round-trip efficiencies at different applied current densities for the same cell as in (**a**).

Fe(Bhmbpy)₃ – Fe(DIPSO) cell (Fig. S32-35)

Characterization of Fe(DIPSO) (Fig. S32)

Stability of Fe(DIPSO) at pH 14 has been demonstrated by previous works, showing a fade rate approximately 0.02%/day.[7, 8] Stability of Fe(DIPSO) at pH 13 in a standard two-chamber flow cell is shown **Fig. S32**.
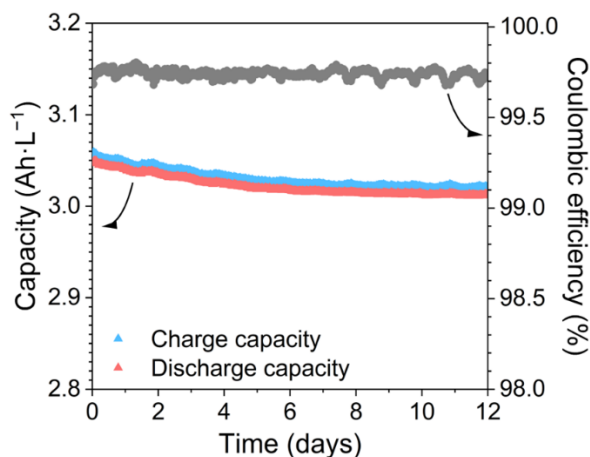

Figure S32 | Cycling stability of Fe(DIPSO) at pH 13. Long term cell cycling of standard two-chamber flow batteries at pH of 13 operated with a constant current (20 mA cm^{-2}) followed by constant potentials of 1.4 V (charging) and 0.6 V (discharging) at room temperature. The cell was assembled with 10 mL 0.11-0.12 M Fe(DIPSO) in 1 M NaCl paired with 50 mL of 0.1 M ferrocyanide/0.02 M ferricyanide in 1 M separated by a E620 K cation exchange membrane. The pH of both sides was adjusted to 13 by addition of NaOH. The capacity fade rate of the first few days is fast due to precipitation of some unstable complexes. The capacity fade rate then stabilized to about 0.05%/day.

29

Standard cycling of three-chamber ARFB with adding exogenous acid and base (Fig. S33)
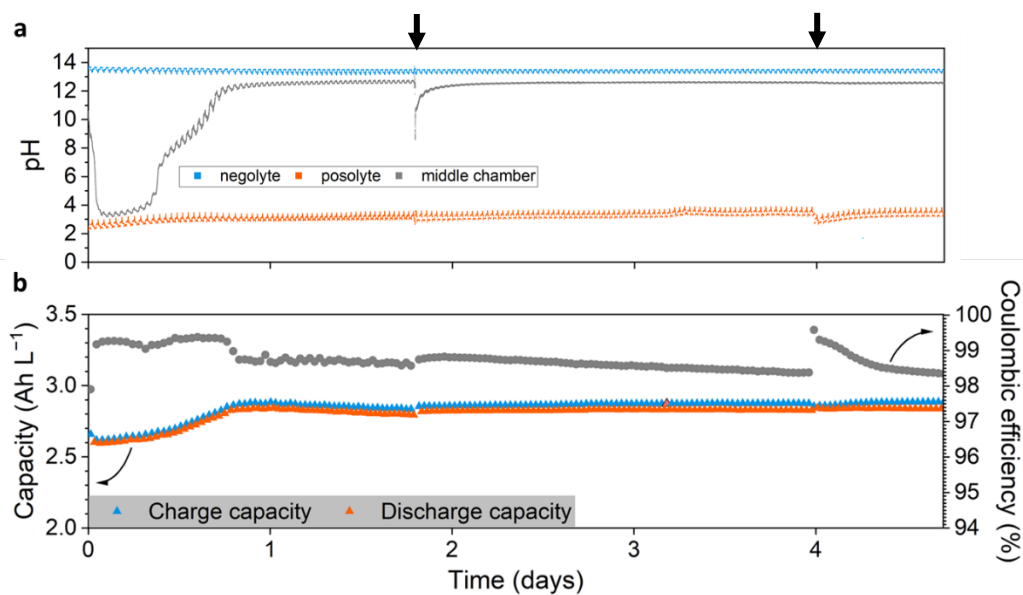

Figure S33 | Fe(Bhmbpy)₃ – Fe(DIPSO) cell long-term cycling with adding exogenous acid and base. a, In-situ monitoring of negolyte, posolyte, and middle chamber pH. **b,** Capacity and Coulombic efficiency during long-term cycling. Acid (1 M HCl) and base (1 M NaOH) was added on day 1.8 and day 4 (indicated by the arrows).

Cycling of three-chamber ARFB with BPM sub-cell in-situ pH recovery (Fig. S34-35)
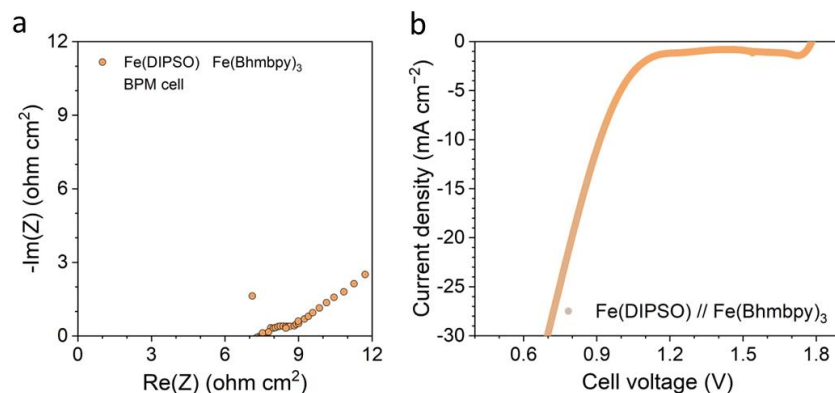

Figure S34 | BPM sub-cell characterization of Fe(Bhmbpy)₃ – Fe(DIPSO) cell. a, PEIS of BPM subcell. **b,** Polarization LSV curve of BPM sub-cell.
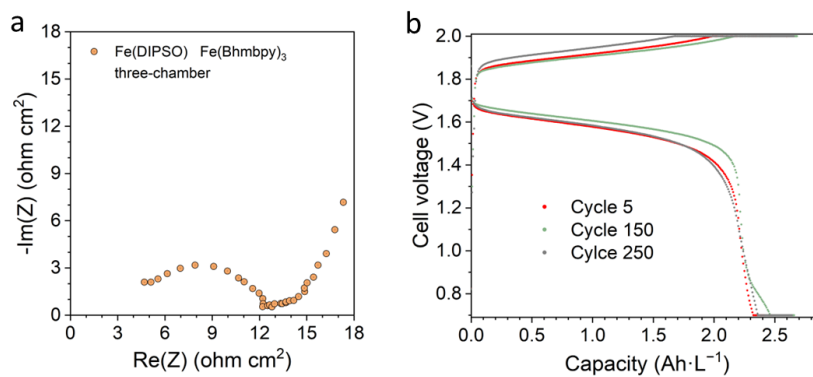

Figure S35 | Characterization of Fe(Bhmbpy)₃ – Fe(DIPSO) three-chamber cell with BPM sub-cell pH recovery. a, PEIS of the three-chamber cell. **b,** Selected voltage – capacity curve of the threechamber cell with recovery.

FeCl$_2$ – BHPC high concentration cell (Fig. S36)

FeCl$_2$ – BHPC high concentration cell was operated using 10 mL 2 M FeCl$_2$, with HCl adjusting initial pH to 2, and 10 mL 1 M BHPC, with NaOH adjusting initial pH to 13. PEIS was used to measure three-chamber cell resistance. PEIS also shows slower kinetic of iron ions as posolyte (**Fig. S36a**). The cell was cycled with CCCV: 1.8 V charge cutoff, with voltage hold until 1 mA/cm^2 cutoff, and 1 V discharge cutoff, with voltage hold until 0.2 mA/cm^2 cutoff (**Fig. S36b**). pH recovery (indicated by black arrows) was operated by discharging the electrolyte in the BPM sub-cell for about 6 mAh after the second cycle. pH afterwards showed clear higher gradient, indicating successful pH recovery (**Fig. S36c,d**). The capacity fading was caused by iron ion crossover, forming precipitation in center chamber. The iron crossover flux for a 2 M source is about 0.1 – 0.2 nmol s^{-1} cm^{-2}, although iron ions have much smaller crossover coefficient than protons through AEMs. This calls for further development of mild acidic posolyte that has low crossover, high voltage, low cost, low fade rate and high solubility.
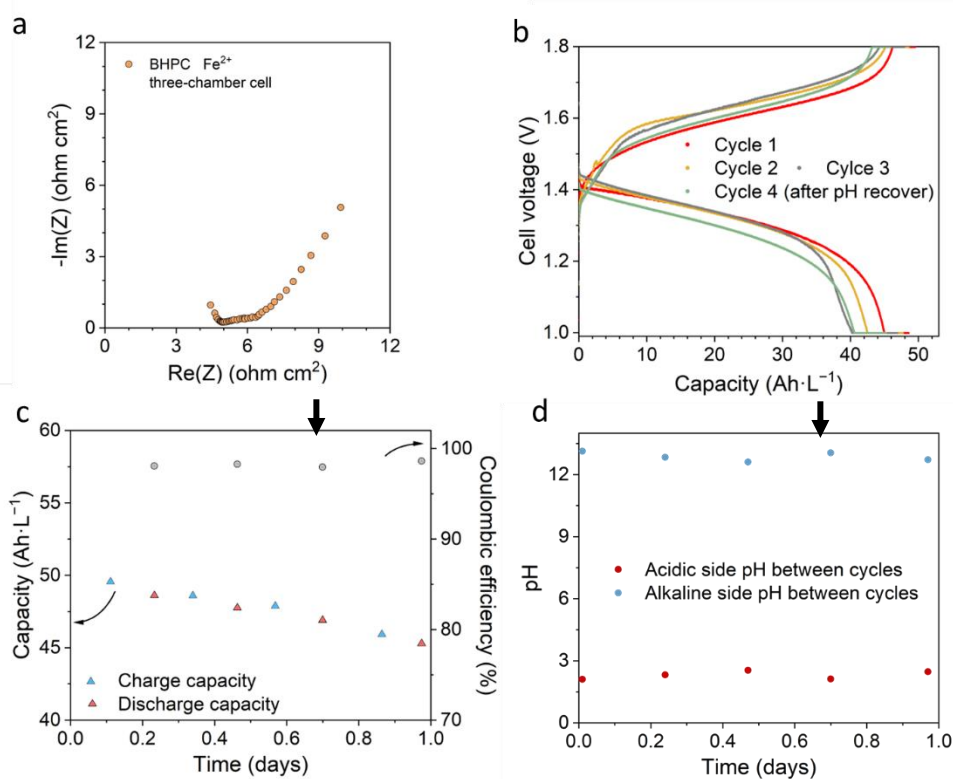

Figure S36 | Characterization of FeCl$_2$ – BHPC three-chamber cell with BPM sub-cell pH recovery. a, PEIS of the three-chamber cell. **b,** Voltage – capacity curve of the three-chamber cell with recovery. **c,** Capacity fading of the cell. **d,** pH testing during cell cycling. pH recovery was run around day 0.6.

Techno-economic calculation (Fig. S37-40)

Techno-economic calculation was done using the methodology and input parameters, except as specified below, from reported work.[9] Values for resistance, reactor cost, balance-of-plant cost, system cost and operation cost were adjusted to account for the structure of our three-chamber setup with BPM sub-cell.[10]

Inherent cost penalty from general pH-decoupling systems (Fig. S37)

We studied the capital cost associated with the acid-base crossover. The cost estimate in this section is independent of the three-chamber battery system cost. The capital cost of a BPM recovery sub-cell can be assigned into two parts. The first part is the BPM recovery sub-cell cost. If the acid-base crossover is more severe, assuming a minimally sized BPM recovery sub-cell that operates constantly, we will have to use a larger BPM recovery sub-cell. The second part is the energy consumed by acid-base recovery. Capacity utilized in the recovery process cannot be counted into the energy storage capacity.

Input values for economic analyses of an acid-base BPM recovery sub-cell:

n is the energy storage project cycle duration at rated power in *hr*.

F is Faraday constant in *C/mol*, whose value equals to 96485.

$CostA_{BPM}$ is the BPM system area cost in *$/cm²*, whose value is estimated as 0.05 (equaling to $500/m²).

$V_{recover}$ is the BPM acid-base recovery voltage cost in *V*, whose value is estimated as 1.4 (thermodynamic 0.83 V; adding overpotential from our experimental results).

$I_{recover}$ is the BPM acid-base recovery current density in *A/cm²*, whose value is assumed as 0.1.

J is the net acid-base crossover flux in *nmol/cm²/s*.

$I_{crossover}$ is the acid-base crossover equivalent current density in *A/cm²*. The value of $I_{crossover}$ can be calculated using $F * J * 10^{-9}$.

This crossover current density will be always multiplied by 2, because crossover happens during both charge and discharge.

Three-chamber cell discharge voltaic efficiency: 0.8.

ASR is the three-chamber cell area-specific resistance in *ohm cm²*, whose value is estimated as 2.

OCV is the three-chamber cell open circuit voltage in *V*.

$Area_{capacity}$ is the three-chamber battery area per capacity in *cm²/kWh*. The value of $Area_{capacity}$ can be calculated using $\frac{ASR}{0.2\ OCV * 0.8\ OCV * n} * 1000$.

I_{three} is the current density of the three-chamber battery cycling system in *A/cm²*. The value of I_{three} can be estimated using $\frac{0.2\ OCV}{ASR}$.

We first estimate the BPM sub-cell setup capital cost. This term is related to the crossover rate. Because with faster crossover rate, we need larger BPM cell to realize fast enough pH recovery of the system.

According to our estimation,

Cost$_{recovery}$ is the BPM recovery sub-cell capital cost in $/kWh, whose value can be calculated using

$$Cost_{recovery} = \frac{I_{crossover}*2*Area_{capacity}}{I_{recover}} * CostA_{BPM}$$

$$= \frac{F*J*2*\frac{ASR}{0.2\ OCV*0.8\ OCV*n}}{I_{recover}} * 10^{-6} * 0.05$$

By assuming a 4-hour project, BPM recovery sub-cell capital cost is shown in **Fig. S37a.** The equation above shows that the BPM recovery sub-cell capital cost is proportional to the acid-base crossover rate and is inversely proportional to the discharge duration at rated power and to the square of the OCV.

Next, we estimate the capital cost penalty factor caused by acid-base crossover. The penalty factor a0 is from the energy cost of acid-base crossover recovery, because the energy consumed during recovery cannot be considered as stored capacity. Basically, faster crossover costs more energy, which penalizes energy storage efficiency. Therefore, by multiplying a0 with capital cost of the whole system that has a certain crossover flux J, we achieve the capital cost of the system with considering acid-base crossover energy consumption.

Capital cost penalty factor from the energy cost of acid-base crossover recovery:

$$a0 = \frac{1}{1-\frac{I_{crossover}*2}{I_{three}}*\frac{V_{recover}}{OCV}} = \frac{1}{1-\frac{F*J*2*10^{-9}}{\frac{0.2\ OCV}{ASR}}*\frac{1.4}{OCV}}$$

The capital cost penalty factor of the combined battery and BPM recovery sub-cell is shown in **Fig. S37b**. The system energy storage cost is less penalized with higher OCV of the three-chamber cell and with lower acid-base crossover flux. The capital cost of the whole system can be calculated by adding BPM recovery sub-cell capital cost, then multiplying by the penalty factor a0. The capital cost penalty factor a0 and BPM recovery sub-cell capital cost is plotted against pH crossover rate in **Fig. S37c**, assuming a 4 h project and 1.7 V OCV of the three-chamber cell for battery cycling.
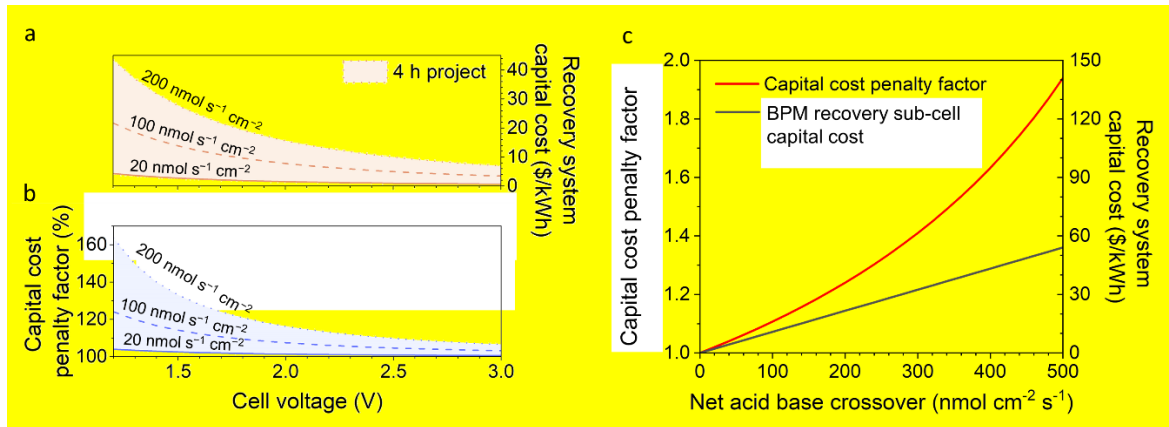
Figure S37 | Capital cost from acid-base recovery system. a, The BPM recovery sub-cell capital cost of a 4 h project vs. OCV of the three-chamber cell, with various acid-base crossover flux values. **b,** The energy storage system capital cost penalty factor caused by energy consumption for pH recovery vs. OCV of the three-chamber cell, with various acid-base crossover flux values. **c,** The BPM recovery sub-cell capital cost and the energy storage system capital cost penalty factor caused by energy consumption of pH recovery vs. acid-base crossover flux for a 4-hour, 1.7 V OCV battery.

Capital cost of a three-chamber two-membrane ARFB with recovery system (Fig. S38-39)

In this section, we further study the capital cost of a hypothetical battery system with acid-base recovery. These costs depend on the cost of several components of the three-chamber battery system. Basically, costs from the extra chamber, extra membrane, center flow, BPM sub-cell hardware, the BPM itself, and recovery energy input were added to the published model.[9-13] By adding the cost of the acid-base recovery system, we are able to study the acid-base recovery cost tradeoff against the advantage of increased battery voltage. The possible cost of the active species and their molecular weights are taken from reported work.[9-12] These hypothetical numbers can be reasonable. Specifically, Ce, Fe and Zn are frequently used and studied in pH-decoupling ARFBs.[6, 14-16] A three-chamber pH decoupled ARFB using $Ce^{3+/4+}$ ($5.37 per kg, 0.140 kg per mole electrons) or $Fe^{2+/3+}$ ($0.04 per kg, 0.056 kg per mole electrons) as posolyte and $Zn/Zn(OH)_4^{2-}$ ($2.36 per kg, 0.033 kg per mole electrons) as negolyte can be lower than the assumptions of molecular weight and cost we used here (adding posolyte and negolyte together, $5 per kg, 0.3 kg per mole electrons)[6]. Prices of metals were taken from www.dailymetalprice.com in July 2023.

Input values for economic analyses of a three-chamber two-membrane system are as follows for a n-hour project:

n is the energy storage project cycle duration at rated power in *hr*.

Discharge voltaic efficiency (including resistance, mass transport limitation and overpotential during discharging): 0.7.

Roundtrip Coulombic efficiency: 0.97.

Depth of discharge: 0.85.

ASR is the three-chamber cell area-specific resistance in *ohm cm²*, whose value is estimated as 2.

$CostA_{three}$ is the three-chamber two-membrane system area cost in *$/cm²*, whose value is estimated as 0.025 (equaling to $250/m², presumed average cost of one membrane $100/m²).

Balance-of-plant cost is in $/kW, whose value is estimated as 260.

Additional cost is in $/kW, whose value is estimated as 125.

MW is the active species molecular weight in kg/mol.

n_e is the number of transferrable electrons per molecule.

M_e is the molecular weight per mole of transferrable electrons in kg/mol. $M_e = MW/n_e$. The value is estimated as 0.15, meaning 0.15 kg per mole of transferrable electrons for each side.

Therefore, for negolyte + posolyte, the total M_e is 0.3, meaning 0.3 kg per mole electrons.

Solubility of active species in electrolyte is in kg/kg, whose value is estimated as 0.2.

Cost of active species is in $/kg, whose value is estimated as 5.

Cost of electrolyte is in $/kg, whose value is estimated 1.

$3600000 \, C = 1 \, kAh$

$Cost_{electrolyte}$ is the active species (including electrolyte cost) cost per unit energy in $/kWh, whose value can be calculated using

$$\frac{gravimetric \; cost(including \; electrolyte \; cost)*MW*3600000}{F*n_e*OCV*efficiency}$$

$$= \frac{gravimetric \; cost*M_e*3600000}{F*OCV*efficiency}$$

$$= \left(5 + \frac{1}{0.2}\right) * 0.3 * \frac{1}{F} * \frac{1}{OCV*efficiency}$$

$\approx 112/OCV/0.85/0.7/0.97$

$\approx 200/OCV$

I_{three} is the current density of the three-chamber battery cycling system in *A/cm^2*, whose value can be estimated using $\frac{0.2 \; OCV}{ASR}$.

$Area_{capacity}$ is the three-chamber battery area per capacity in *cm^2/kWh*, whose value can be calculated using $\frac{ASR}{0.2 \; OCV*0.8 \; OCV*n*0.7*0.85*0.97} * 1000$.

$Cost_{cell}$ is the cell stack cost in $/kWh, whose value can be calculated using

$$Cost_{cell} = Area_{capacity} * CostA_{three} = \frac{ASR*1000}{0.2 \; OCV*0.8 \; OCV*n*0.7*0.85*0.97} * 0.025$$

System additional cost (Balance-of-plant costs + Additional costs) is in $/kW, and its value is estimated as 400 .

$Cost_{addition}$ is the additional cost for an n-hour project in $/kW, whose value can be estimated as $\frac{1}{n} * 400$

$Cost_{recovery}$ and recovery energy efficiency (capital cost) penalty factor a0 is defined as previously discussed.

$Capital \; cost = (Cost_{electrolyte} + Cost_{cell} + Cost_{addition} + Cost_{recovery}) * a0$

The capital costs of 4 h, 6 h and 10 h projects with different cell voltage were approximated at different acid-base crossover fluxes (**Fig. S38**). The solid line shows the cost of the whole system with zero pH crossover. Higher cell voltage will increase the energy stored in a certain number of active molecules. Higher OCV will also increase the cell power density and thereby decrease the required area for a cell stack. Therefore, the capital cost of the battery system drops when the cell voltage goes higher. Meanwhile, in a pH-decoupling cell, higher acid-base crossover will lead to higher energy cost for pH recovery and higher capital cost associated with a larger BPM sub-cell. For example, when the cell voltage is around 1.7 V, a crossover flux of 20 nmol s^{-1} cm^{-2} would increase the capital cost by around 3% (dashed line). When the net crossover reaches 100 (alternating dashed–dotted line) or 200 (dotted line) nmol s^{-1} cm^{-2}, capital cost increases by 15%

and 35%, respectively. Acid-base crossover will be less impactful when using a cell stack with smaller area and higher current density. Because the required battery area for a certain power output decreases fast due to roughly an $(ASR)*(OCV^{-2})$ dependence, an increased OCV will decrease the BPM cell costs and the energy cost of the BPM recovery sub-cell, making the costs of the BPM recovery sub-cell acceptable if the increased OCV more than offsets the increased ASR associated with an additional membrane and an additional electrolyte chamber.
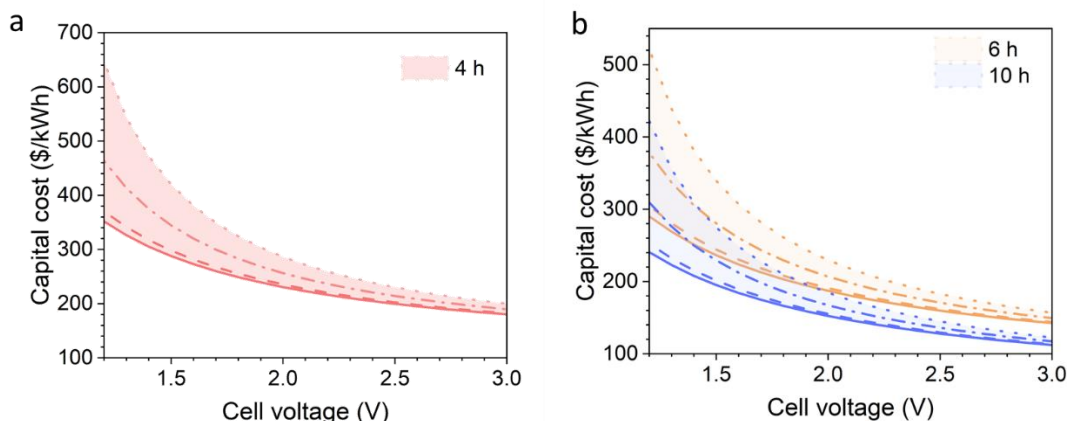

Figure S38 | Techno-economic estimation for three-chamber cell with different OCV. Technoeconomic calculation of the capital cost of a three-chamber pH-decoupling cell with *operando* pH recovery. Capital cost was calculated including three-chamber two-membrane cell stack cost, electrolyte cost, management/maintenance system cost, additional cost, and BPM recovery sub-cell cost, and then multiplied by the capital cost penalty factor a0 caused by acid-base crossover. Solid lines correspond to 0 acid-base crossover. From dashed line to dash-dotted line to dotted line (going up), costs are calculated with 20 to 100 to 200 nmol s^{-1} cm^{-2} net acid-base crossover flux, respectively. Costs are shown in **a,** a 4 h project and **b,** 6 h and 10 h battery projects.

High membrane cost and large ASR are the major concerns for three-chamber two-membrane ARFBs. When fixing the OCV of the cell at 1.7 V and the ASR at 2.0 ohm cm^2, without considering acid-base crossover, the influence of membrane cost on capital cost of the ARFB system is shown in **Fig. S39a**. By fixing the three-chamber battery areal cost at 250 \$/m^2, the ASR of the ARFB is shown to also influence the capital cost (**Fig. S39b**). Lower resistance decreases capital cost of the system and increases the tolerance of higher acid-base crossover.
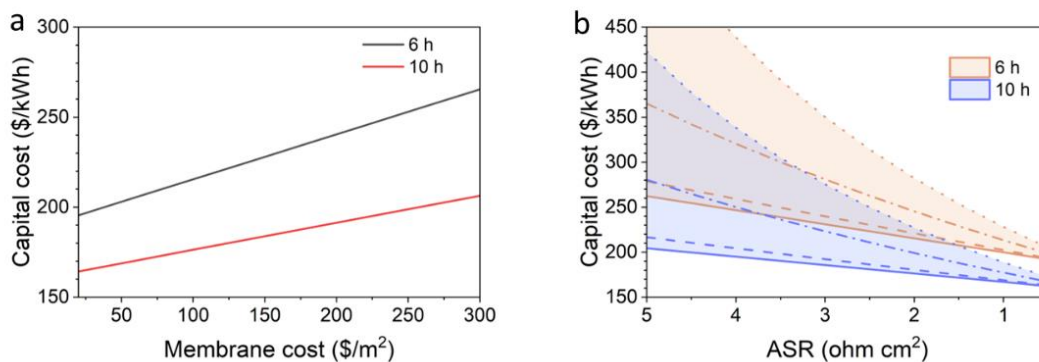
Figure S39 | Techno-economic estimation for three-chamber cell with different membrane cost and ASR. Technoeconomic calculation of the capital cost of a three-chamber pH-decoupling cell with *operando* pH recovery. **a,** Capital cost of the three-chamber system influenced by average areal membrane cost. b, Capital cost of 6 h and 10 h battery projects with different ASR. Capital cost was calculated including three-chamber two-membrane cell stack cost, electrolyte cost, management/maintenance system cost, additional cost, and BPM recovery sub-cell cost, and then multiplied by the capital cost penalty factor a0 caused by acid-base crossover. Solid lines correspond to 0 acid-base crossover. From dashed line to dash-dotted line to dotted line (going up), costs are calculated with 20 to 100 to 200 nmol s^{-1} cm^{-2} net acid-base crossover flux, respectively. Other parameters are set as default (OCV = 1.7 V, ASR = 2.0 ohm cm^2, battery areal cost = 250 \$/m^2) during the investigation of membrane cost in (a) and ASR in (b).

Characterization and influence of membranes – AEMs as examples

The capital cost of the pH-recovery BPM cell and the energy cost during pH-recovery are functions dominated by net acid-base crossover flux, also influenced by the resistance and OCV of the three-chamber cell. The crossover flux of hydroxides through Fumasep E620 is low (< 2 nmol s^{-1} cm^{-2}, equivalent net acid-base crossover current $= 0.19$ mA cm^{-2}) even working against a pH 14 solution. The crossover flux of protons through Selemion DSV-N is high (~ 200 nmol s^{-1} cm^{-2}, equivalent net acid-base crossover current $= 19$ mA cm^{-2}), limiting the utilization of our three-chamber cell under severe pH-decoupling systems (e.g., pH 0 decoupled from pH 14). Therefore we tested various AEMs that are available on the market to study the influence of membrane choice on the cost of the pH-recovery system, demonstrating the important metrics of membranes that researchers should pay attention to when working with pH-decoupling systems.

AEMs we selected for the test are: Selemion DSV-N, Selemion AMV-N, PiperION-A20, IONOMR AF-1-CNN5-50-X. For the characterization of membranes, we assembled a 5 cm^2 flow cell and performed PEIS on the cell under the flow of 1 M NaCl solution on both sides. PEIS measurements were conducted near OCV with a perturbation of 10 mV and frequencies ranging from 1 to 100,000 Hz. The intercept of the plot with the real axis gives the high frequency resistance of the cell. The high frequency ASR of the membrane under 1 M NaCl is plotted in **Fig. S40a**. Then, to evaluate the proton crossover rate through a certain membrane from pH 0, we changed the electrolyte on one side of the membrane to 1 M HCl, and measured the time-dependent pH change in the initially neutral NaCl side. The results are shown in the semi-log plot in **Fig. S40a**. Points near the left-hand edge of the plot represent highly selective AEMs; points near the horizontal axis represent membranes with low resistance to anionic current.

We calculated the capital cost of the BPM cell and energy penalty during pH-recovery assuming a 6-hour (n = 6) energy/power ratio.

$Cost_{recovery}$ is the BPM recovery sub-cell capital cost in $/kWh, whose value can be calculated using

$$Cost_{recovery} = \frac{I_{crossover}*2*Area_{capacity}}{I_{recover}} * CostA_{BPM}$$

$$= \frac{F*J*2*\frac{ASR}{0.2\,OCV*0.8\,OCV*n}}{I_{recover}} * 10^{-6} * 0.05$$

Energy cost penalty factor from acid-base crossover recovery:

$$Energy_{recovery} = \frac{I_{crossover}*2}{I_{three}} * \frac{V_{recover}}{OCV} * 100\% = \frac{F*J*2*10^{-9}}{\frac{0.2\,OCV}{ASR}} * \frac{1.4}{OCV} * 100\%$$

As shown in **Fig. S40b**, for a three-chamber cell with an OCV of 1.7 V (black "+") or 2.0 V (red "×"), the cost related to pH-recovery for the crossover of protons from pH 0 is very low for AMV-N, making the severe pH-decoupling ARFB still possibly practical. For example, by using AMV-N with an E620 CEM in a pH 0 decoupling pH 14 battery, we expect a net acid-base crossover flux lower than 2 nmol cm^{-2} s^{-1}, causing negligible energy efficiency loss ($< 0.1\%$) and BPM sub-cell cost ($< \$0.1$/kWh).

Although the area-specific resistance (ASR) of AMV-N, which is 110 μm thick, is twice that of DSV-N, in principle the possibility exists of casting AMV-N at half of this thickness. This would result in halving the ASR and doubling the proton crossover flux, which would still be negligible

(< 2 nmol s^{-1} cm^{-2}). It might even be possible to produce the equivalent of AMV-N at 20 μm thickness – that of E620 – further cutting the ASR while keeping the proton crossover flux very low. Consequently, AEM ASR is not a fundamental limitation of the approach taken here.
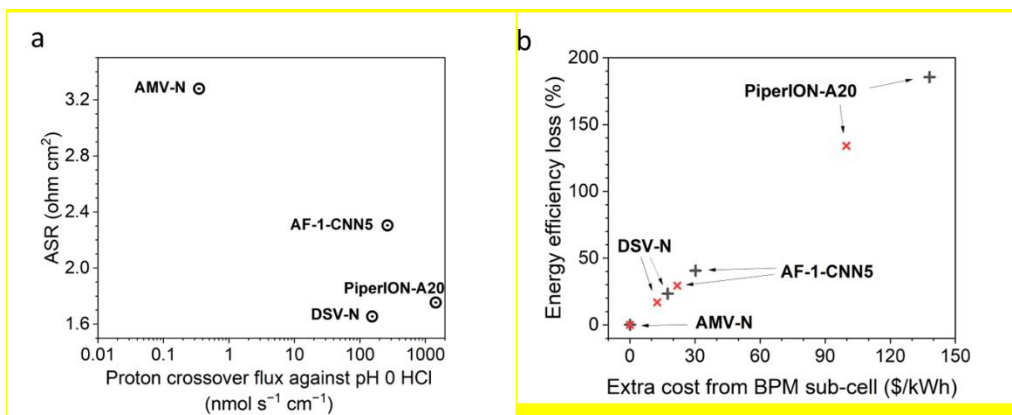

Figure S40 | Properties of AEMs and their influence on recovery costs. a, Membranes with different area-specific resistance to anionic current in 1 M NaCl, and their proton crossover flux into 1 M NaCl from 1 M HCl. **b,** Calculated extra cost of BPM sub-cell for pH recovery and energy efficiency loss due to acid-base crossover. The calculation is based on a 6-hour energy/power ratio for a 1.7 V (black "+") and a 2.0 V (red "×") pH-decoupling ARFB.

41

Capital cost of a single-membrane pH-decoupling ARFB with recovery system (Fig. S41)

The concept of mild pH-decoupling and pH recovery can be used in single-membrane pH-decoupling ARFBs, which are more commercially attractive due to lower membrane cost and ASR.

Input values for economic analyses of a single membrane system are as follows for a n-hour project:

n is the energy storage project cycle duration at rated power in *hr*.

Discharge voltaic efficiency (including resistance, mass transport limitation and overpotential during discharging): 0.7.

Roundtrip Coulombic efficiency: 0.97.

Depth of discharge: 0.85.

ASR is the single-membrane cell area-specific resistance in *ohm cm²*, whose value is estimated as 0.8.

CostA$_{single}$ is the system area cost in *$/cm²*, whose value is estimated as 0.0175 (equaling to $175/m²).

Balance-of-plant cost is in $/kW, whose value is estimated as 260.

Additional cost is in $/kW, whose value is estimated as 125.

Cost of electrolytes and molecules are the same as used in the "capital cost of a three-chamber two-membrane ARFB with recovery system".

Cost$_{electrolyte}$ is the active species (including electrolyte cost) cost per unit energy in $/kWh, whose value can be calculated using

$$\frac{gravimetric\ cost(including\ electrolyte\ cost)*MW*3600000}{F*n_e*OCV*efficiency}$$

$$= \frac{gravimetric\ cost*M_e*3600000}{F*OCV*efficiency}$$

$$= \left(5 + \frac{1}{0.2}\right)*0.3*\frac{1}{F}*\frac{1}{OCV*efficiency}$$

≈ 112/OCV/0.85/0.7/0.97

≈ 200/OCV

I$_{single}$ is the current density of the single-membrane battery cycling system in *A/cm²*, whose value can be estimated using $\frac{0.2\ OCV}{ASR}$.

Area$_{capacity}$ is the single-membrane battery area per capacity in *cm²/kWh*, whose value can be calculated using $\frac{ASR}{0.2\ OCV*0.8\ OCV*n*0.7*0.85*0.97}*1000$.

Cost$_{cell}$ is the cell stack cost in $/kWh, whose value can be calculated using

$$Cost_{cell} = Area_{capacity} * CostA_{single} = \frac{ASR*1000}{0.2\ OCV*0.8\ OCV*n*0.7*0.85*0.97}*0.0175$$

System additional cost (Balance-of-plant costs + Additional costs) is in \$/kW, and its value is estimated as 400 .

Cost_{addition} is the additional cost for an n-hour project in \$/kW, whose value can be estimated as $\frac{1}{n} * 400$

Cost_{recovery} and recovery energy efficiency (capital cost) penalty factor a0 is defined as previously discussed.

*Capital cost = (Cost_{electrolyte} + Cost_{cell} + Cost_{addition} + Cost_{recovery}) * a0*

The capital costs of 6 h and 10 h projects with different cell voltage for a single-membrane mild pH-decoupling ARFB with pH recovery were approximated at different acid-base crossover fluxes (**Fig. S41**). The decreased ASR of the single-membrane system compared to that of the two-membrane system increased its tolerance for acid-base crossover. The solid line shows the cost of the whole system with zero pH crossover. When the cell voltage is around 1.7 V, a crossover flux of 20 nmol s^{-1} cm^{-2} would increase the capital cost by around 1% (dashed line). When the net crossover reaches 100 (alternating dashed–dotted line) or 200 (dotted line) nmol s^{-1} cm^{-2}, capital cost increases by 6% and 12%, respectively.
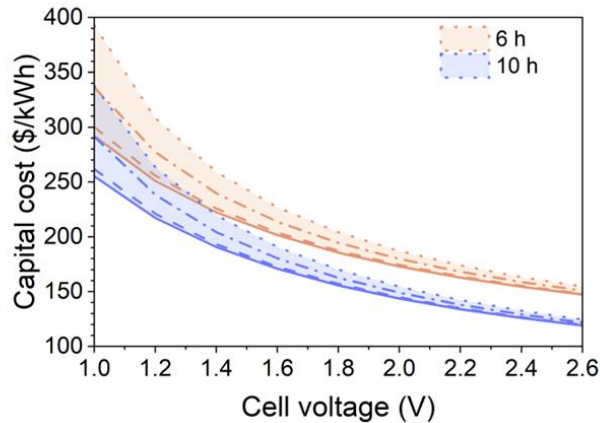

Figure S41 | Techno-economic estimation of single-membrane cell capital cost vs. OCV for 6 h and 10 h projects. Capital cost was calculated including single-membrane cell stack cost, electrolyte cost, management/maintenance system cost, additional cost, and BPM recovery sub-cell cost, and then was multiplied by the capital cost penalty factor a0 caused by acid-base crossover. Solid lines correspond to 0 acid-base crossover. From dashed line to dash-dotted line to dotted line (going up), costs are calculated with 20 to 100 to 200 nmol s^{-1} cm^{-2} net acid-base crossover flux, respectively.

Single-membrane mild pH-decoupling ARFB with pH recovery (Fig. S42-44)

KBr – CrPDTA high concentration single-membrane pH-decoupling cell was operated using 5 mL 1 M CrPDTA, with 0.1 M PDTA as buffer, using KOH to adjust initial pH to 9, and 10 mL 1 M KBr in water, without adjusting pH. CrPDTA only works in pH 9 – 10, while KBr/KBr$_3$ only works below pH 7 (Br$_2$ will disproportionate when pH is 7 or higher). The cell was assembled using 3 layers of carbon papers (SGL 39AA) baked at 400 °C overnight in each half-cell, separated by an untreated Fumasep E610K or Nafion 212. Polarization performance of the cell was tested using LSV with a scan rate of 0.1 V s^{-1} (**Fig. 42a**). PEIS was used to measure high frequency ASR. Polarization ASR was measured using the slope near OCV LSV with a scan rate of 0.01 V s^{-1} (**Fig. 42b**). The high value of polarization ASR is mainly caused by the low kinetic of CrPDTA, which can be solved by using Bi as catalysts.[17] The cell was cycled with CCCV: constant current of 50 mA cm^{-2}, with a 2.4 V charge cutoff, with voltage hold until 20 mA cm^{-2} cutoff, and 1.4 V discharge cutoff, with voltage hold until 20 mA cm^{-2} cutoff (**Fig. 43**). The pH change during operation could be caused by the side reaction for posolyte (Br$_2$ oxidizing the carbon electrode) and negolyte (hydrogen evolution reaction), or small amount of proton coupled electrochemical reactions that oxidized carbon electrode could have. A Coulombic efficiency of 98% is caused by the crossover of Br$_2$. Acid-base generation (at the beginning of the cell cycling) was operated by discharging the electrolyte in the BPM sub-cell for about 3 mAh. The difference of the LSV in the main cell and BPM sub-cell shows the energy cost for acid-base generation (**Fig. 44**). It is worth noticing that CrPDTA has a very low crossover rate, and this system is not vulnerate towards the crossover of redox active species. Br crossover will not cause decomposition or fading in CrPDTA side (**Fig. 45**).
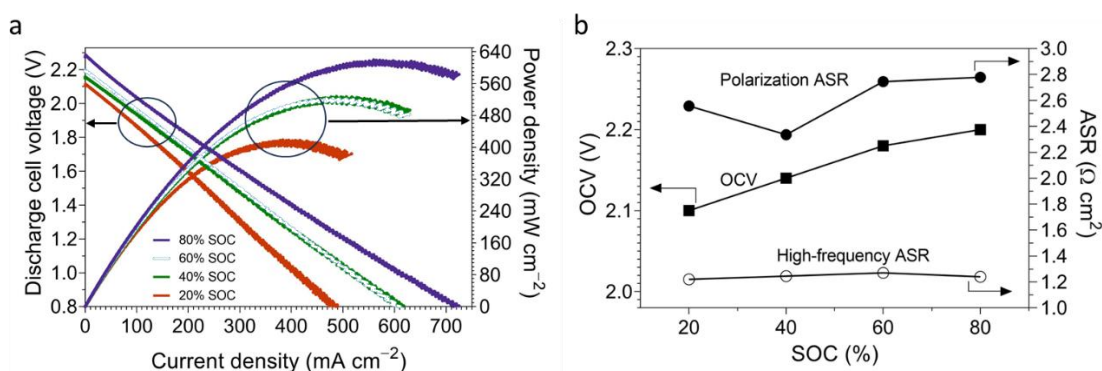
Polarization performance (Fig. S42)

Figure S42 | Polarization performance of the single-membrane KBr (pH < 7) – CrPDTA (pH 9 – 10) cell. a, Cell voltage and power density during discharge of the KBr-CrPDTA ARFB with 1 M KBr and 1 M CrPDTA, separated by Fumasep E610K as CEM. **b,** Plots of OCV and high frequency and polarization ASR vs. SOC for the same cell as in (**a**).

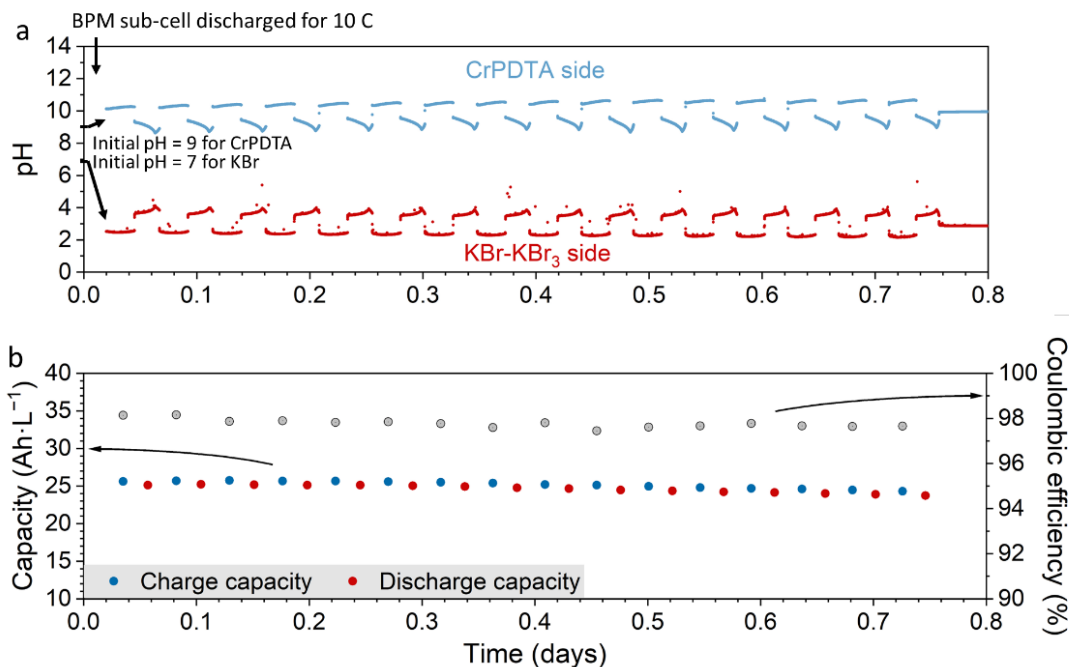## Cycling of single-membrane pH-decoupling ARFB with BPM sub-cell pH recovery (Fig. S43-45)

Figure S43 | KBr – CrPDTA cell cycling with BPM sub-cell discharging before starting. a, In-situ monitoring of negolyte and posolyte pH. The initial pH change is introduced by the discharging of electrolytes in the BPM sub-cell. The pH swing and drifting are mainly caused by proton coupled side reactions. **b,** Capacity and Coulombic efficiency during cycling. Coulombic efficiency is about 98%, penalized by Br_2 crossover.
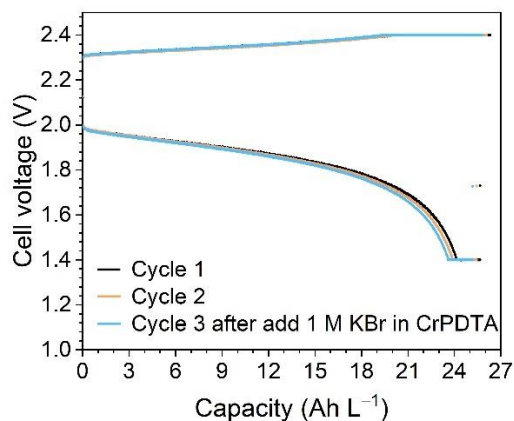
Figure S44 | KBr – CrPDTA cell cycling with KBr added. KBr was manually added in the CrPDTA electrolyte after cycle 2 to show that the crossover of Br_2 and its subsequent reduction to bromide will not cause decomposition, precipitation or cell failure.
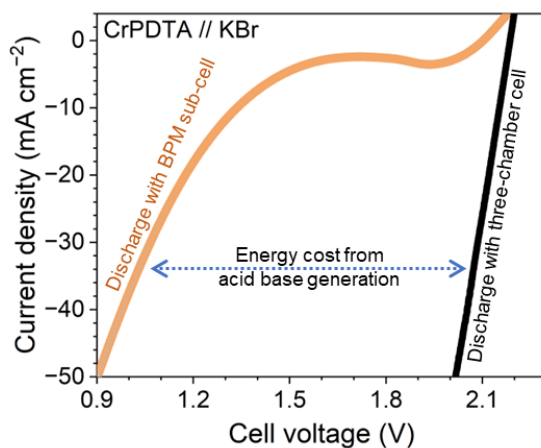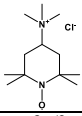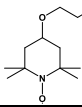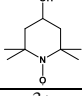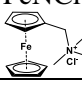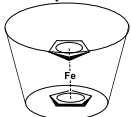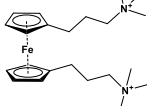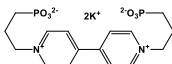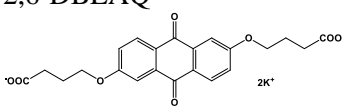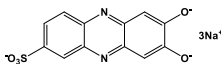
Figure S45 | Performance of the BPM sub-cell. LSV curve of the BPM sub-cell and three-chamber cell. Electrolytes are pumped into BPM sub-cell at 20% – 60% SOC. LSV curve was collected with a sweep rate of 3 mV s^{-1} to discharge the electrolytes. The OCV is about 2.15 V, and water dissociation starts around 1.4 V. The voltage cost for acid-base generation is around 1 V at 40 mA cm^{-2}.

Table S1. Redox molecule candidates[*].

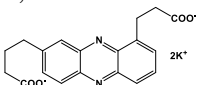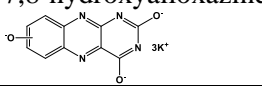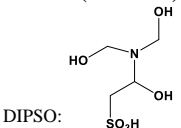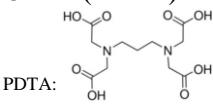| Name & Structure	Voltage (V vs. SHE)	Working pH	Note	Reference
Ce^{4+}/Ce^{3+}	1.44	< 0	Posolyte. Cation. Strong acid, need to consider acid crossover. Voltage changes with anions. Need to check water splitting.	[18]
Cl_2/Cl^-	1.36	< 7	Posolyte. Anion. High vapor pressure.	
MnO_2/Mn^{2+}	1.22 (pH = 0)	< 2	Posolyte. Cation. Strong acid, need to consider acid crossover. Proton coupled.	[19]
Br_3^-/Br^-	1.09	< 7	Posolyte. Anion. High vapor pressure.	[20]
VO_2^+/VO^{2+}	1.04 (pH = 0)	< 1	Posolyte. Cation. Strong acid, need to consider acid crossover. Proton coupled.	[21]
TEMPTMA	1.01	~ 7	Posolyte. Cation.	[22]
$Fe^{3+/2+}(Bhmbpy)_3$ (as shown)	0.98	2 – 4	Posolyte. Cation.	[1]
$MnO_2/Mn(OAc)_2$	0.85	4	Posolyte. Cation.	[23]
TMAP-TEMPO	0.80	~ 7	Posolyte. Cation.	[24]
4-OH-TEMPO	0.81	~ 7	Posolyte. Cation.	[25]
Fe^{3+}/Fe^{2+}	0.77	< 3	Posolyte. Cation.	[6]
FcNCl ($Fe^{3+/2+}$)	0.61	~ 7	Posolyte. Cation.	[26]
I_3^-/I^-	0.54	< 7	Posolyte. Anion.	[27]
Fc⊂β-CD ($Fe^{3+/2+}$)	0.5	~ 7	Posolyte. Cation.	[28]

BTMAP-Fc (Fe$^{3+/2+}$)	0.39	~ 7	Posolyte. Cation.	[29]
S$_4^{2-}$/S$_2^{2-}$	−0.42	> 11	Negolyte. Anion.	[14]
BPP-Vi	−0.46	~ 7	Negolyte. Anion.	[30]
2,6-DBEAQ	−0.52 (pH 12)	> 12	Negolyte. Anion.	[31]
DHAQ	−0.68 (pH 14)	14	Negolyte. Anion.	[32]
BHPC (as shown)	−0.78 (pH 14)	> 12	Negolyte. Anion. Proton coupled.	[2]
DHPS	−1.05 (pH 14)	> 13	Negolyte. Anion. Proton coupled.	[33]
1,8-PFP	−0.57 (pH 14)	> 7	Negolyte. Anion. Proton coupled.	[34]
7,8-hydroxyalloxazine	−0.72 (pH 14)	14	Negolyte. Anion. Proton coupled.	[35]
Fe$^{3+/2+}$(DIPSO)	−0.82	> 13	Negolyte. Anion.	[7]
Cr$^{3+/2+}$ (PDTA)	−1.18	~ 9	Negolyte. Anion. Need to check water splitting.	[36]
Zn/Zn(OH)$_4^{2-}$	−1.22 (pH 14)	> 14	Negolyte. Anion. Strong base. Need to consider base crossover. Need to check water splitting.	[15]

* We only included the examples of some organic molecules. We mainly included cation as posolyte and anion as negolyte.

1.   Gao, J.; Amini, K.; George, T. Y.; Jing, Y.; Tsukamoto, T.; Xi, D.; Gordon, R. G.; Aziz, M. J., A High Potential, Low Capacity Fade Rate Iron Complex Posolyte for Aqueous Organic Flow Batteries. *Adv. Energy Mater.* **2022,** *12* (44).

2.   Wang, C.; Li, X.; Yu, B.; Wang, Y.; Yang, Z.; Wang, H.; Lin, H.; Ma, J.; Li, G.; Jin, Z., Molecular Design of Fused-Ring Phenazine Derivatives for Long-Cycling Alkaline Redox Flow Batteries. *ACS Energy Lett.* **2020,** *5* (2), 411-417.

3.   Kong, T.; Liu, J.; Zhou, X.; Xu, J.; Xie, Y.; Chen, J.; Li, X.; Wang, Y., Stable Operation of Aqueous Organic Redox Flow Batteries in Air Atmosphere. *Angew. Chem. Int. Ed.* **2023,** *62* (6), e202214819.

4.   Jin, S.; Wu, M.; Jing, Y.; Gordon, R. G.; Aziz, M. J., Low energy carbon capture via electrochemically induced pH swing with electrochemical rebalancing. *Nat. Commun.* **2022,** *13* (1), 2140.

5.   Hohenadel, A.; Powers, D.; Wycisk, R.; Adamski, M.; Pintauro, P.; Holdcroft, S., Electrochemical characterization of hydrocarbon bipolar membranes with varying junction morphology. *ACS Applied Energy Materials* **2019,** *2* (9), 6817-6824.

6.   Gong, K.; Ma, X.; Conforti, K. M.; Kuttler, K. J.; Grunewald, J. B.; Yeager, K. L.; Bazant, M. Z.; Gu, S.; Yan, Y., A zinc–iron redox-flow battery under $100 per kW h of system capital cost. *Energy Environ. Sci.* **2015,** *8* (10), 2941-2945.

7.   Shin, M.; Noh, C.; Chung, Y.; Kwon, Y., All iron aqueous redox flow batteries using organometallic complexes consisting of iron and 3-[bis (2-hydroxyethyl)amino]-2-hydroxypropanesulfonic acid ligand and ferrocyanide as redox couple. *Chem. Eng. J.* **2020,** *398*.

8.   Shin, M.; Noh, C.; Kwon, Y., Stability enhancement for all‐iron aqueous redox flow battery using iron‐3‐[bis(2‐hydroxyethyl)amino]‐2‐hydroxypropanesulfonic acid complex and ferrocyanide as redox couple. *International Journal of Energy Research* **2021,** *46* (5), 6866-6875.

9.   Darling, R. M.; Gallagher, K. G.; Kowalski, J. A.; Ha, S.; Brushett, F. R., Pathways to low-cost electrochemical energy storage: a comparison of aqueous and nonaqueous flow batteries. *Energy Environ. Sci.* **2014,** *7* (11), 3459-3477.

10.   Perry, M. L.; Rodby, K. E.; Brushett, F. R., Untapped Potential: The Need and Opportunity for High-Voltage Aqueous Redox Flow Batteries. *ACS Energy Lett.* **2022,** *7* (2), 659-667.

11.   Iwakiri, I.; Antunes, T.; Almeida, H.; Sousa, J. P.; Figueira, R. B.; Mendes, A., Redox flow batteries: Materials, design and prospects. *Energies* **2021,** *14* (18), 5643.

12.   Darling, R. M., Techno-economic analyses of several redox flow batteries using levelized cost of energy storage. *Current Opinion in Chemical Engineering* **2022,** *37*, 100855.

13.   Dmello, R.; Milshtein, J. D.; Brushett, F. R.; Smith, K. C., Cost-driven materials selection criteria for redox flow battery electrolytes. *J. Power Sources* **2016,** *330*, 261-272.

14.   Gu, S.; Gong, K.; Yan, E. Z.; Yan, Y., A multiple ion-exchange membrane design for redox flow batteries. *Energy Environ. Sci.* **2014,** *7* (9), 2986-2998.

15.   Park, M.; Beh, E. S.; Fell, E. M.; Jing, Y.; Kerr, E. F.; Porcellinis, D.; Goulet, M. A.; Ryu, J.; Wong, A. A.; Gordon, R. G.; Cho, J.; Aziz, M. J., A High Voltage Aqueous Zinc–Organic Hybrid Flow Battery. *Adv. Energy Mater.* **2019,** *9* (25).

16.   Zhu, Y.-h.; Cui, Y.-f.; Xie, Z.-l.; Zhuang, Z.-b.; Huang, G.; Zhang, X.-b., Decoupled aqueous batteries using pH-decoupling electrolytes. *Nat. Rev. Chem.* **2022,** *6* (7), 505-517.

17.   Waters, S. E.; Robb, B. H.; Scappaticci, S. J.; Saraidaridis, J. D.; Marshak, M. P., Isolation and characterization of a highly reducing aqueous chromium (II) complex. *Inorg. Chem.* **2022,** *61* (23), 8752-8759.

18.   Leung, P. K.; Ponce-de-León, C.; Low, C. T. J.; Shah, A. A.; Walsh, F. C., Characterization of a zinc–cerium flow battery. *J. Power Sources* **2011,** *196* (11), 5174-5185.

19.   Zhong, C.; Liu, B.; Ding, J.; Liu, X.; Zhong, Y.; Li, Y.; Sun, C.; Han, X.; Deng, Y.; Zhao, N.; Hu, W., Decoupling electrolytes towards stable and high-energy rechargeable aqueous zinc–manganese dioxide batteries. *Nat. Energy* **2020,** *5* (6), 440-449.

20.   Huskinson, B.; Marshak, M. P.; Suh, C.; Er, S.; Gerhardt, M. R.; Galvin, C. J.; Chen, X.; Aspuru-Guzik, A.; Gordon, R. G.; Aziz, M. J., A metal-free organic-inorganic aqueous flow battery. *Nature* **2014,** *505* (7482), 195-8.

21.   Parasuraman, A.; Lim, T. M.; Menictas, C.; Skyllas-Kazacos, M., Review of material research and development for vanadium redox flow battery applications. *Electrochim. Acta* **2013,** *101*, 27-40.

22.   Janoschka, T.; Martin, N.; Hager, M. D.; Schubert, U. S., An aqueous redox‐flow battery with high capacity and power: the TEMPTMA/MV system. *Angewandte Chemie International Edition* **2016,** *55* (46), 14427-14430.

23.   Lei, J.; Yao, Y.; Huang, Y.; Lu, Y.-C., A highly reversible low-cost aqueous sulfur–manganese redox flow battery. *ACS Energy Lett.* **2022,** *8* (1), 429-435.

24.   Liu, Y.; Goulet, M.-A.; Tong, L.; Liu, Y.; Ji, Y.; Wu, L.; Gordon, R. G.; Aziz, M. J.; Yang, Z.; Xu, T., A long-lifetime all-organic aqueous flow battery utilizing TMAP-TEMPO radical. *Chem* **2019,** *5* (7), 1861-1870.

25.   Liu, T.; Wei, X.; Nie, Z.; Sprenkle, V.; Wang, W., A total organic aqueous redox flow battery employing a low cost and sustainable methyl viologen anolyte and 4‐HO‐TEMPO catholyte. *Adv. Energy Mater.* **2016,** *6* (3), 1501449.

26.   Hu, B.; DeBruler, C.; Rhodes, Z.; Liu, T. L., Long-cycling aqueous organic redox flow battery (AORFB) toward sustainable and safe energy storage. *J. Am. Chem. Soc.* **2017,** *139* (3), 1207-1214.

27.   Lei, J.; Zhang, Y.; Yao, Y.; Shi, Y.; Leung, K. L.; Fan, J.; Lu, Y.-C., An active and durable molecular catalyst for aqueous polysulfide-based redox flow batteries. *Nat. Energy* **2023**, 1-10.

28.   Li, Y.; Xu, Z.; Liu, Y.; Jin, S.; Fell, E. M.; Wang, B.; Gordon, R. G.; Aziz, M. J.; Yang, Z.; Xu, T., Functioning Water‐Insoluble Ferrocenes for Aqueous Organic Flow Battery via Host–Guest Inclusion. *ChemSusChem* **2021,** *14* (2), 745-752.

29.   Beh, E. S.; De Porcellinis, D.; Gracia, R. L.; Xia, K. T.; Gordon, R. G.; Aziz, M. J., A neutral pH aqueous organic–organometallic redox flow battery with extremely high capacity retention. *ACS Energy Lett.* **2017,** *2* (3), 639-644.

30.   Jin, S.; Fell, E. M.; Vina‐Lopez, L.; Jing, Y.; Michalak, P. W.; Gordon, R. G.; Aziz, M. J., Near Neutral pH Redox Flow Battery with Low Permeability and Long‐Lifetime Phosphonated Viologen Active Species. *Adv. Energy Mater.* **2020,** *10* (20).

31.   Kwabi, D. G.; Lin, K.; Ji, Y.; Kerr, E. F.; Goulet, M.-A.; De Porcellinis, D.; Tabor, D. P.; Pollack, D. A.; Aspuru-Guzik, A.; Gordon, R. G.; Aziz, M. J., Alkaline Quinone Flow Battery with Long Lifetime at pH 12. *Joule* **2018,** *2* (9), 1894-1906.

32.   Lin, K.; Chen, Q.; Gerhardt, M. R.; Tong, L.; Kim, S. B.; Eisenach, L.; Valle, A. W.; Hardee, D.; Gordon, R. G.; Aziz, M. J., Alkaline quinone flow battery. *Science* **2015,** *349* (6255), 1529-1532.

33.   Hollas, A.; Wei, X.; Murugesan, V.; Nie, Z.; Li, B.; Reed, D.; Liu, J.; Sprenkle, V.; Wang, W., A biomimetic high-capacity phenazine-based anolyte for aqueous organic redox flow batteries. *Nat. Energy* **2018,** *3* (6), 508-514.

34.   Xu, J.; Pang, S.; Wang, X.; Wang, P.; Ji, Y., Ultrastable aqueous phenazine flow batteries with high capacity operated at elevated temperatures. *Joule* **2021,** *5* (9), 2437-2449.

35.   Lin, K.; Gómez-Bombarelli, R.; Beh, E. S.; Tong, L.; Chen, Q.; Valle, A.; Aspuru-Guzik, A.; Aziz, M. J.; Gordon, R. G., A redox-flow battery with an alloxazine-based organic electrolyte. *Nat. Energy* **2016,** *1* (9).

36.   Robb, B. H.; Farrell, J. M.; Marshak, M. P., Chelated Chromium Electrolyte Enabling High-Voltage Aqueous Flow Batteries. *Joule* **2019,** *3* (10), 2503-2512.